# Photoproduction of $\Lambda(1405)$ and $\Sigma^0(1385)$ hyperons on the proton at $E_\gamma = 1.5 - 2.4$ GeV

## Masayuki Niiyama

A dissertation submitted in partial fulfillment of the requirements for the degreee of

Doctor of Science

Department of Physics
Kyoto University

# Contents

# Chapter 1

# Introduction

## 1.1  Structure of the $\Lambda(1405)$

In the quark model, the $\Lambda(1405)$ and $\Sigma^0(1385)$ are assigned as three quark baryon resonances of $u$, $d$, and $s$-quarks with the spin-parity of $J^P = \frac{1}{2}^-$ and $J^P = \frac{3}{2}^+$, respectively. The observed mass peak positions are 1.407 GeV/c$^2$ for the $\Lambda(1405)$ and 1.384 GeV/c$^2$ for the $\Sigma^0(1385)$ [1]. Although the mass and quark flavor are similar for these two hyperons, the understanding of the internal structure of these two are quite different. The $\Sigma^0(1385)$ is a member of the baryon decuplet and firmly established as the three quark ($q^3$) baryon resonance. In contrast, the structure of the $\Lambda(1405)$ is unclear. In the quark model, the $\Lambda(1405)$ is the spin-multiplet partner of the $\Lambda(1520)$ ($J^P = \frac{3}{2}^-$) hyperon. However, the observed mass of $\Lambda(1405)$ is much smaller than the theoretical prediction, and the mass difference is too large to be explained by the $LS$ splitting between quarks. For example, a nonrelativistic quark model by Isgur and Karl calculated the mass of the $\Lambda(1405)$ as 1.49 GeV/c$^2$ [2], which is degenerate with the mass of the $\Lambda(1520)$. A bag model by DeGrand predicted even higher mass for the $\Lambda(1405)$ than the $\Lambda(1520)$ due to the $LS$ force between quarks [3]. Instead of the picture of $q^3$ baryon resonance, the $\Lambda(1405)$ has been discussed as a possible candidate of a meson-baryon molecular state because the observed mass of the $\Lambda(1405)$ is close to the $\bar{K}N$ threshold, 1.43 GeV/c$^2$ [4, 5]. If the $\Lambda(1405)$ is such a meson-baryon molecule, the $q^3$ baryon which is the spin-multiplet partner of the $\Lambda(1520)$ is missing. There has been a long discussion whether the $\Lambda(1405)$ is a $q^3$ baryon or a meson-baryon molecule. The discussion is well summarized in the reference [6].

Theoretically, the $\Lambda(1405)$ has been studied intensively using various models, but clear answer has not been obtained so far. Recently, the lattice QCD calculation was performed to study the structure of the $\Lambda(1405)$ model-independently. Melnitchouk *et al.* calculated the mass of the $\Lambda(1405)$ as a $q^3$ baryon using the quenched lattice QCD simulation, and they found the mass of the $\Lambda(1405)$ to be about 1.7 GeV/c$^2$, which is much heavier than the true mass of the $\Lambda(1405)$ [7]. The other lattice

calculations by Nemoto *et al.* and Ishii *et al.* also obtained the mass of the $\Lambda(1405)$ to be about 1.7 GeV/c$^2$ for the $q^3$ bound state and 1.89 GeV/c$^2$ for the $q^4\bar{q}$ bound state. They suggested that the $\Lambda(1405)$ might be a mixed state of these two quark configurations [8,9]. Based on the meson-baryon molecular picture for the $\Lambda(1405)$, Nacher *et al.* dynamically generated the lineshape of the $\Lambda(1405)$ as a $\pi\Sigma$ and $\bar{K}N$ molecular state using a chiral Lagrangian and coupled unitary model [10]. In addition, the same model predicted a second pole of the $\Lambda(1405)$ at 1.42 GeV/c$^2$ which strongly couples to the $\bar{K}N$ channel [11]. According to their prediction, the second pole become visible for the reaction in which a virtual $\bar{K}$ interacts with a nucleon. For the study of the structure of the $\Lambda(1405)$ , the experimental data on the pole position and width of the $\Lambda(1405)$ produced by various initial states is desired.
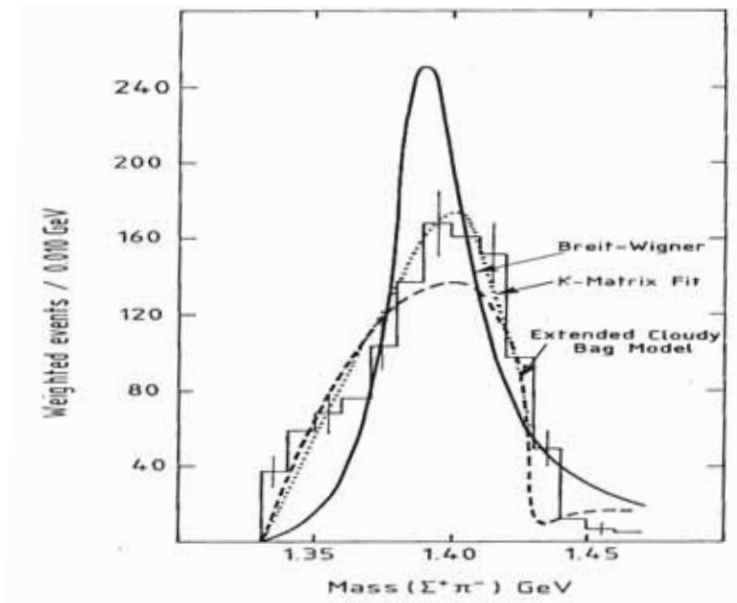


Figure 1.1: Invariant mass spectrum of the $\Lambda(1405)$ measured by Hemingway via the $K^-p \to \pi^-\Sigma^+(1660) \to \pi^-\pi^+\Lambda(1405)$ reaction.

Contrary to the intensive theoretical study, the experimental study on the the $\Lambda(1405)$ is not sufficient. It is difficult to measure the $\Lambda(1405)$ due to the background of the $\Sigma^0(1385)$ because the intrinsic widths of these resonances, 36 MeV/c$^2$ for the $\Sigma^0(1385)$ and 50 MeV/c$^2$ for the $\Lambda(1405)$, are much larger than their mass difference. There are two old bubble chamber experiments which measured the lineshape of the $\Lambda(1405)$. The first one was done by Thomas *et al.* in BNL in the year 1973 via the $\pi^-p \to K_s^0\Lambda(1405) \to K_s^0\pi^\pm\Sigma^\mp$ reaction [12]. The second one

was done by Hemingway in CERN in the year 1984 via the $K^- p \to \pi^- \Sigma^+ (1660) \to \pi^- \pi^+ \Lambda(1405) \to \pi^- \pi^+ \pi^- \Sigma^+$ reaction [13]. The histogram in Fig. 1.1 shows the invariant mass spectrum of the $\Lambda(1405)$ measured by Hemingway. The lineshape of the $\Lambda(1405)$ is asymmetric because it couples to the $KN$ channel which opens from 1.43 GeV/c$^2$, and therefore, it is hard to be fitted by the Breit-Wigner function. In Fig. 1.1, the theoretical curves of K-matrix fit and an extended cloudy bag model are shown by the dotted and dashed lines, respectively. Both models contain $\bar{K}N$ and $\Sigma\pi$ scattering amplitudes to reproduce the lineshape of the $\Lambda(1405)$. From these results, the strong coupling of the $\Lambda(1405)$ to the meson-baryon channel has been suggested.
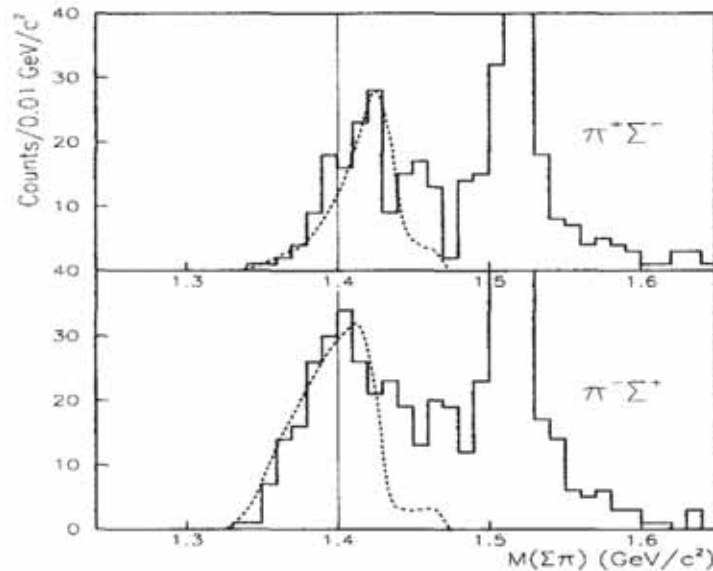


Figure 1.2: Invariant mass spectra of the $\Lambda(1405)$ obtained by the previous measurement at LEPS [14]. The dotted lines show the theoretical spectra by Nacher *et al.*

In the year 2002, Ahn *et al.* measured the lineshape of the $\Lambda(1405)$ at SPring-8/LEPS via the $\gamma p \to K^+ \Lambda(1405) \to K^+ \pi^{\pm} \Sigma^{\mp}$ reaction [14]. The observed lineshapes of the $\Lambda(1405)$ in the $\pi^+ \Sigma^-$ and $\pi^- \Sigma^+$ modes are shown in top and bottom plots of Fig. 1.2, respectively. The dotted lines show the theoretical spectra by Nacher *et al* [10]. In this measurement, the mass peak positions and widths of the $\Lambda(1405)$ in $\pi^+ \Sigma^-$ and $\pi^- \Sigma^+$ modes were different, which can be understood as the result of the interference between the isospin 0 and 1 amplitudes of the $\Sigma\pi$ interaction [10]. Recently, two more experimental studies have been reported. Prakhov *et al.* measured the cross section for $K^- p \to \pi^0 \pi^0 \Sigma^0$ reaction and observed that the contribution of $\pi^0 \Lambda(1405)$ production dominates in this reaction [15]. Magas *et*

*al.* compared their model calculation with this data and claimed the evidence of the second pole of the $\Lambda(1405)$ [16]. Fig. 1.3 shows the mass spectra of the $\Lambda(1405)$ obtained by Prakhov *et al.* (solid) and Thomas *et al.* (dashed). The triangles indicate the mass peak positions of the $\Lambda(1405)$ calculated by Magas *et al.* The mass peak positions of these two spectra are different. The peak position measured by Prakhov *et al.* is around 1.41 GeV/c$^2$, while that measured by Thomas *et al.* is 1.39 GeV/c$^2$. According to the model calculation by Magas *et al.*, the second pole of the $\Lambda(1405)$ is enhanced in the $K^-p \to \pi^0\pi^0\Sigma^0$ reaction, and the peak position of the mass spectrum of $\Lambda(1405)$ is shifted to the higher mass side. Thus, they claimed the evidence of the second pole of the $\Lambda(1405)$ .
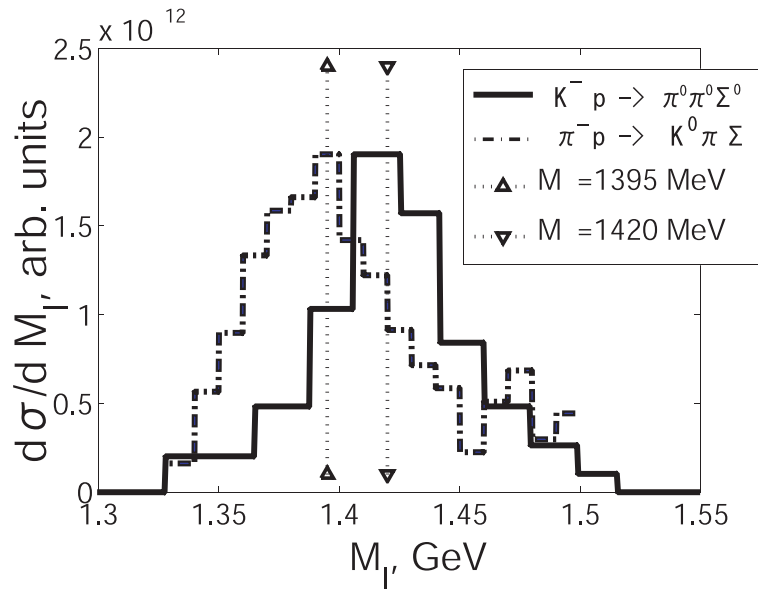


Figure 1.3: Mass spectra of the $\Lambda(1405)$ measured by Prakhov *et al.* (solid) and Thomas *et al.* (dashed). The triangles indicate the mass peak positions of the $\Lambda(1405)$ calculated by Magas *et al.*

The second experimental study was reported by Zychor *et al.* They measured the lineshape and the production cross section of the $\Lambda(1405)$ via the $pp \to pK^+\Lambda(1405) \to pK^+\pi^0\Sigma^0$ reaction [17]. Closed circles in Fig. 1.4 show the invariant mass spectrum of the $\Lambda(1405)$ measured by Zychor *et al.* The lineshape of the $\Lambda(1405)$ was compared with those measured by Hemingway (solid histogram) and Thomas *et al.* (dashed histogram). In their measurement, the observed lineshape was consistent with those obtained by Hemingway and Thomas *et al.*

The mass peak position and width of the $\Lambda(1405)$ are not established firmly. These values are important to study the internal structure of the $\Lambda(1405)$, and more experimental data are necessary.
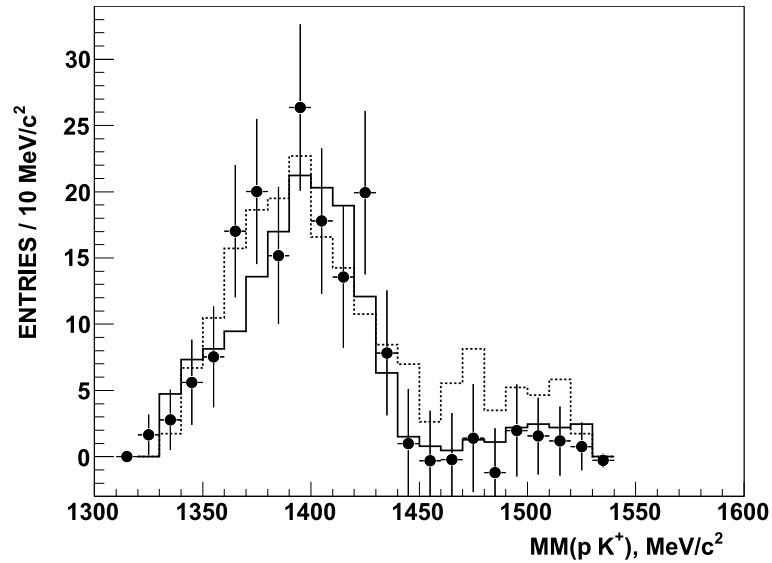
Figure 1.4: The invariant mass spectrum of the $\Lambda(1405)$ . Closed circles show the spectrum obtained by Zychor *et al.* via the $pp \rightarrow pK^+\Lambda(1405)$ reaction. The solid and dashed histograms show the spectra obtained by Hemingway and Thomas *et al.*, respectively. The solid and dashed histograms are normalized to the height of the spectrum measured by Zychor *et al.*

## 1.2 Low energy $\bar{K}N$ interaction and kaonic hydrogen

The $\Lambda(1405)$ lies about 30 MeV below the $\bar{K}N$ threshold and has a strong influence on the low energy $\bar{K}N$ interaction. There was a long standing problem, so-called kaonic hydrogen puzzle, which was concerned with a discrepancy between the $1S$ level shift of the kaonic hydrogen atom determined from measurements of the atomic X-rays [18–20] and that from the low-energy $\bar{K}N$ scattering data [21–23]. The atomic data indicated a downward shift of the $1S$ level, while the scattering data were extrapolated to the $K^-p$ threshold to predict an upward shift. The kaonic hydrogen puzzle was solved by a precise measurement of kaonic hydrogen X-rays by Iwasaki *et al* [24]. They reported an upward shift of the $1S$ level: $\epsilon + i\frac{\Gamma}{2} = -323 + 407\frac{i}{2}$ eV. The observed level shift corresponds to the $K^-p$ scattering length as $A_{K^-p} = -0.78 + 0.49i$ fm. This scattering length was consistent with the one extracted from the $K^-p$ scattering data, which indicates a strong attractive interaction between $K^-p$. The strong attractive $\bar{K}N$ interaction can be interpreted as due to the existence of the

bound state of $\bar{K}$ and $N$, and it suggests that the $\Lambda(1405)$ is a $\bar{K}N$ molecule.

Based on the $\bar{K}N$ molecular picture of the $\Lambda(1405)$ , Akaishi and Yamazaki calculated $\bar{K}N$ and $\bar{K}$-nucleus potentials and predicted the existence of deeply bound kaonic nuclear states [25, 26]. In addition, Dote *et al.* predicted that a $\bar{K}$ strongly attracts nucleons in nucleus and forms a high density and low temperature nuclear matter [27]. The existence of the kaonic nucleus is concerned with the kaon condensation in the neutron star. Experimentally, the kaonic nucleus has been searched for via various reactions [28–35], and the FINUDA group and OBELIX group reported the evidence of bound $\bar{K}$ nuclear states [33–35]. However, the existence of the kaonic nucleus is not established firmly, and further experimental studies are planned [36–38]. The assumption that the $\Lambda(1405)$ is a deeply bound $\bar{K}N$ state by Akaishi and Yamazaki contradicts with the prediction of the second pole of the $\Lambda(1405)$ by Jido *et al.* Jido *et al* predicted that $\bar{K}N$ component of the $\Lambda(1405)$ has the pole at 1.42 GeV/c$^2$ and $\bar{K}N$ interaction is weaker than that calculated by Akaishi and Yamazaki. Thus, the experimental study on the internal structure of the $\Lambda(1405)$ is important for the study of the kaonic nucleus.

## 1.3   Photoproduction of hyperon resonances

The photoproduction of the $\Lambda$ and $\Sigma^0$ hyperons off protons has been studied with high statistics data [39–42], mainly motivated by missing resonances which could couple to the $KY$ channels [43]. On the other hand, photoproduction of the $\Lambda(1405)$ and the $\Sigma^0(1385)$ has not been studied well. Photoproduction of the $\Sigma^0(1385)$ has been measured by bubble chamber experiments with limited statistics [44, 45]. Recently, the CLAS Collaboration at TJNAF has measured the photoproduction of the $\Sigma^0(1385)$ with a photon energy range of 1.5-3.8 GeV [46]. A theoretical calculation by Oh *et al.* [47] using an effective Lagrangian was then compared with the preliminary data of total cross section by the CLAS experiment, and the contributions from nucleon resonances were discussed.

The $\Lambda(1405)$ has been studied in meson-induced and proton-induced reactions so far [12,13,15,17]. However, understanding of the photoproduction of the $\Lambda(1405)$ is very limited because of the lack of experimental data. Theoretically, Nacher *et al.* [10] predicted the cross section of the $\Lambda(1405)$ photoproduction to be 5 $\mu$b/GeV at the peak of the invariant mass spectrum of the $\Lambda(1405)$ using a chiral unitary model. Lutz and Soyeur calculated the differential cross section for the sum of the $\Sigma(1385)$ and $\Lambda(1405)$ photoproduction using a chiral coupled-channel effective model [48]. In both theoretical calculations, the effect of the interference between the $\Lambda(1405)$ and $\Sigma^0(1385)$ production amplitudes was neglected.

The production mechanisms for the $\gamma p \rightarrow K^+ Y^*$ reaction are shown in Fig. 1.5, where $Y^*$ stands for a hyperon resonance, $\Lambda(1405)$ or $\Sigma^0(1385)$. Fig. 1.5(a) shows the $t$-channel $\bar{K}$ and $\bar{K}^*$ meson exchange diagram. The $s$-channel diagram shown in Fig. 1.5(b) contains contributions from nucleon and $\Delta$ resonances. The $u$-channel

diagram shown in Fig. 1.5(c) contains the contributions from hyperons and their resonances. Fig.1.5(d) is the contact diagram required by the gauge invariance.
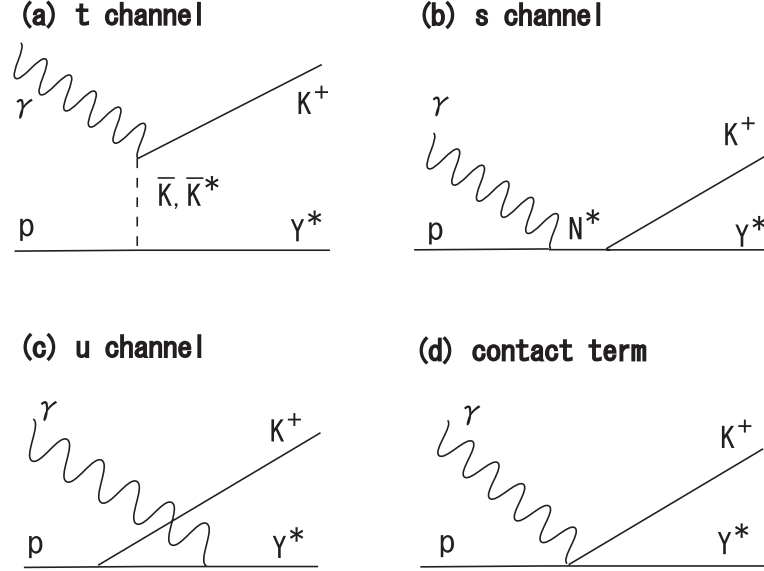


Figure 1.5: Feynman diagrams for the $\gamma p \to K^+ Y^*$ reaction.

In the SPring-8/LEPS, $K^+$'s produced by the $\gamma p \to K^+ Y^*$ reaction is detected in the forward angles, and hyperon resonances are produced with a small momentum transfer. In general, $t$-channel $\bar{K}$ meson exchange diagram (Fig. 1.5(a)) is dominant in such a kinematical region. The $\bar{K} N Y^*$ vertex in Fig. 1.5(a) depends on the the spin and parity of the hyperon resonances, $\frac{1}{2}^-$ for the $\Lambda(1405)$ and $\frac{3}{2}^+$ for the $\Sigma^0(1385)$, and shows the different energy dependence for each hyperon resonance. The $\bar{K} N \Lambda^*$ vertex consists of the $\bar{K} N \Lambda^*$ coupling constant, and does not depend on the three momentum transfer, $q$. On the other hand, the $\bar{K} N \Sigma^*$ vertex contains $\partial_\mu \bar{K} \Sigma^{*\mu} N$ term, and the $T$ matrix is proportional to $q$. By taking account of an additional $q$-dependence due to the phase volume, the production cross section of $\Lambda(1405)$ is proportional to $q$, and that of $\Sigma^0(1385)$ is proportional to $q^3$. Because the momentum transfer increases as the photon energy, the contribution of $\Sigma^0(1385)$ is expected to increase in higher photon energy region. In this work, the differential cross section of the $\Lambda(1405)$ photoproduction and its comparison with that of the $\Sigma^0(1385)$ are reported for the first time. The cross section was measured in two photon energy bins: near production threshold region and far from it.

## 1.4    Hyperon photoproduction experiment at LEPS

A hyperon photoproduction experiment was carried out at the backward Compton
$\gamma$-ray beamline in SPring-8 facility (SPring-8/LEPS) to study the structure of the
$\Lambda(1405)$, whether the $q^3$ state or the meson-baryon molecular state. This experiment
aims to measure the lineshape of the $\Lambda(1405)$ and $\Sigma^0(1385)$ produced in the nuclear
medium. If the $\Lambda(1405)$ is a meson-baryon molecule, its width is expected to become
wider in the medium due to the interaction with nucleons in the nucleus. The width
of the $\Lambda(1405)$ can be compared with that of the $\Sigma(1385)$ which is established as
a $q^3$ state. Fig. 1.6 shows a theoretical calculation of the lineshape of the $\Lambda(1405)$
by Nacher *et al.* The spectrum in the free space is shown as the solid line. The
spectra with the Pauli blocking effect and in the nuclear medium are shown by dot-
dot-dashed line and dot-dashed line, respectively. The broadening of the lineshape
of the $\Lambda(1405)$ can be seen.
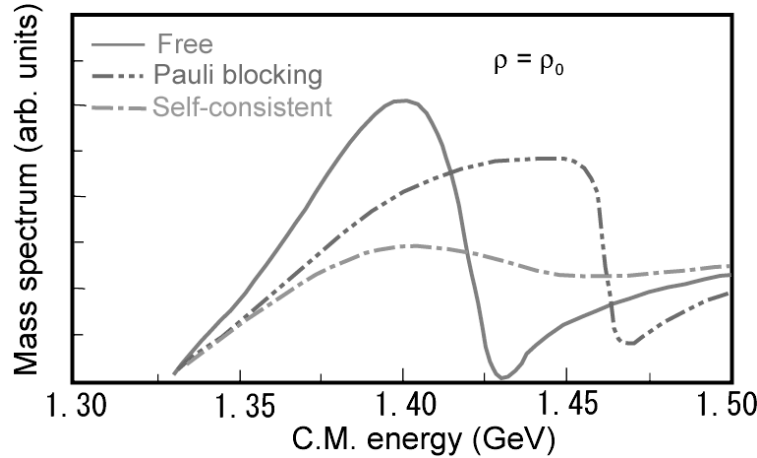


Figure 1.6: Theoretical calculation of the invariant mass distribution of the $\Lambda(1405)$.
The spectrum in the free space is shown as the solid line. The spectra with the Pauli
blocking effect and in the nuclear medium are shown by the dot-dot-dashed line and
dot-dashed line, respectively.

Before measuring the lineshape of the $\Lambda(1405)$ in the nuclear medium, it is nec-
essary to understand the lineshape in the free space. Especially, the interference
between the isospin 0 and 1 terms of the $\Sigma\pi$ interaction which was observed by
the previous measurement at LEPS [14] must be understood because it affects the
shape of the $\Lambda(1405)$. In this work, the lineshapes of the $\Lambda(1405)$ and $\Sigma^0(1385)$
in the free space and the differential cross sections of the $\Lambda(1405)$ and $\Sigma^0(1385)$
photoproduction on the proton are reported.

The photoproduction of the $\Lambda(1116)$ and $\Sigma^0(1192)$ on the proton has been mea-

sured at SPring-8/LEPS facility to search for a missing resonance which decays to $K^+Y$ channels [42]. The $K^+$'s from a liquid hydrogen target were measured at the forward angles by the LEPS spectrometer. The statistics of this data set were sufficiently high to determine the differential cross sections accurately for the ground state $\Lambda$ and $\Sigma^0$ hyperons. Nevertheless, in principle, it is impossible to separate the $\Lambda(1405)$ and $\Sigma^0(1385)$ from a missing mass of the $\gamma p \to K^+Y^*$ reaction, $MM(K^+)$, because the spectra overlap each other. In the previous measurement [14], both a $K^+$ and a charged pion were detected by the LEPS spectrometer, and the $\Sigma^+$ or $\Sigma^-$ was identified from a missing mass of the $\gamma p \to K^+\pi^\pm X$ reaction. Then, the lineshape of the $\Lambda(1405)$ was measured in the $MM(K^+)$ for the $(K^+\Sigma^\pm\pi^\mp)$ final states. Fig. 1.7 shows the invariant mass spectra of the $\Lambda(1405)$ in the $\pi^+\Sigma^-$ channel (top) and the $\pi^-\Sigma^+$ channel (bottom). The peak positions in two decay modes seem different, which can be understood as the result of the interference of the isospin 0 and 1 amplitudes of $\Sigma\pi$ scattering. The theoretical spectra by Nacher *et al.* are shown as dotted lines, which show a good agreement with the experimental data.
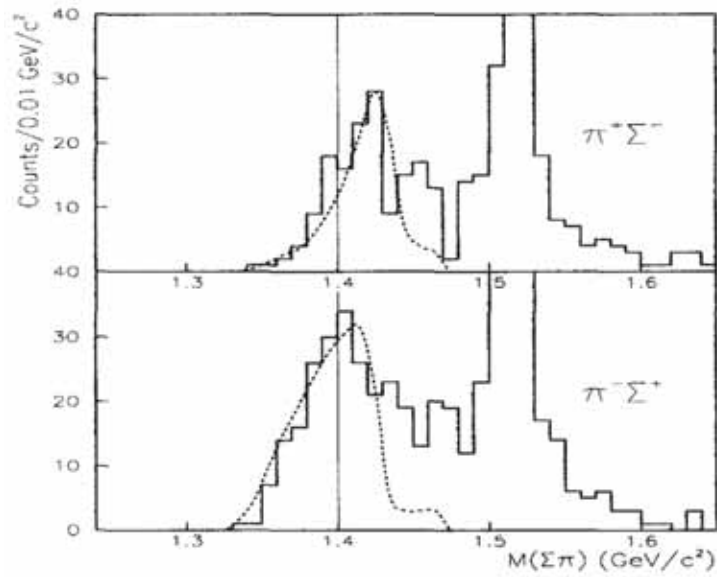


Figure 1.7: Invariant mass spectra of the $\Lambda(1405)$ obtained by the previous measurement at LEPS [14].

In the previous measurement, the contamination from the $\Sigma^0(1385)$ production was not studied because it was impossible to identify all of the decay products from the hyperon resonances due to the limited acceptance. In order to enlarge the acceptance and detect the decay products from hyperon resonances, a time projection chamber (TPC) was used in this work together with the LEPS spectrometer. The

yields of the $\Sigma^0(1385)$ and $\Lambda(1405)$ were measured from their $\Lambda\pi^0$ and $\Sigma^\pm\pi^\mp$ decay modes, respectively. The production ratio of the $\Lambda(1405)$ to $\Sigma^0(1385)$ was then compared in two photon energy regions: $1.5 < E_\gamma < 2.0$ GeV and $2.0 < E_\gamma < 2.4$ GeV.

In Chapter 2, the experimental apparatus is described. The data analysis for the measurement of the production ratio between the $\Sigma^0(1385)$ and $\Lambda(1405)$ is described in Chapter 3. The absolute values of the differential cross sections are described in Chapter 4. The results of the obtained lineshapes and the differential cross sections are discussed in Chapter 5. Finally, this work is concluded in Chapter 6.

# Chapter 2

# Experiment

The experiment was carried out at the backward Compton $\gamma$-ray beamline in SPring-8 (SPring-8/LEPS). The SPring-8/LEPS facility provides a linearly polarized photon beam with high intensity and a large degree of polarization. The photons with the energy of 1.5-2.4 GeV are produced by the backward-Compton-scattering process of laser photons with 8-GeV electrons circulating in the storage ring.

The data were collected using two different experimental setups, referred to hereafter as data set (I) and data set (II). Photoproduction of $\Lambda$ and $\Sigma^0$ has been studied at LEPS using high statistics data with a liquid hydrogen target and the LEPS spectrometer (data set (I)) [42]. The data set (I) was taken in the year 2000 and 2001. The total beam time was about 100 days. The number of photons at the target was about $2 \times 10^{12}$. The statistics of this data set were sufficiently high to determine the differential cross sections accurately for the ground state $\Lambda$ and $\Sigma^0$ hyperons. Nevertheless, in principle, it is impossible to separate $\Lambda(1405)$ and $\Sigma^0(1385)$ from a missing mass of $\gamma p \to K^+ Y^*$ reactions, $MM(K^+)$, because the intrinsic widths of these resonances, 36 MeV/c$^2$ for $\Sigma^0(1385)$ and 50 MeV/c$^2$ for $\Lambda(1405)$, are much larger than their mass difference. In order to distinguish these two, a time projection chamber (TPC) was used for data set (II) together with the LEPS spectrometer to facilitate the detection of the decay products of these hyperon resonances. The data set (II) was taken in the year 2004. The total beam time was about 100 days. Using this data set, the production ratio between $\Sigma^0(1385)$ and $\Lambda(1405)$ was fixed from the yields of $\Sigma^0(1385)$ and $\Lambda(1405)$ measured from their $\Lambda\pi^0$ and $\Sigma^\pm\pi^\mp$ decay modes, respectively. The absolute values of the differential cross sections were then obtained from the $MM(K^+)$ distribution measured in data set (I) with the input of the production ratio between $\Sigma^0(1385)$ and $\Lambda(1405)$ in the common detector acceptance of the two data sets. In this chapter, the details of SPring-8/LEPS facility, the LEPS spectrometer and the TPC are described.

## 2.1   LEPS facility

At the SPring-8/LEPS facility, a photon beam with a energy of few GeV is produced
by the backward-Compton-scattering (BCS) process of laser photons with the 8-GeV
electrons [49]. The 8-GeV electrons circulate in the storage ring with a circumference
of 1435.95 m.  The maximum current is 100 mA. Electrons are filled in some of
the total 2436 bunches with various filling patterns, where the time interval of the
successive bunches is 1.966 nsec. The emittance is $6.89\pi$ nm rad, and the averaged
widths are 75 $\mu$m and 25 $\mu$m in the horizontal and vertical directions, respectively.

    The schematic view of the LEPS beam line is shown in Fig. 2.1. The beam line
consists of three parts: (a) laser-electron collision part in the storage (SR) ring, (b)
the first hutch for laser injection (laser hutch), and (c) the second hutch where a
spectrometer is placed (experimental hutch).
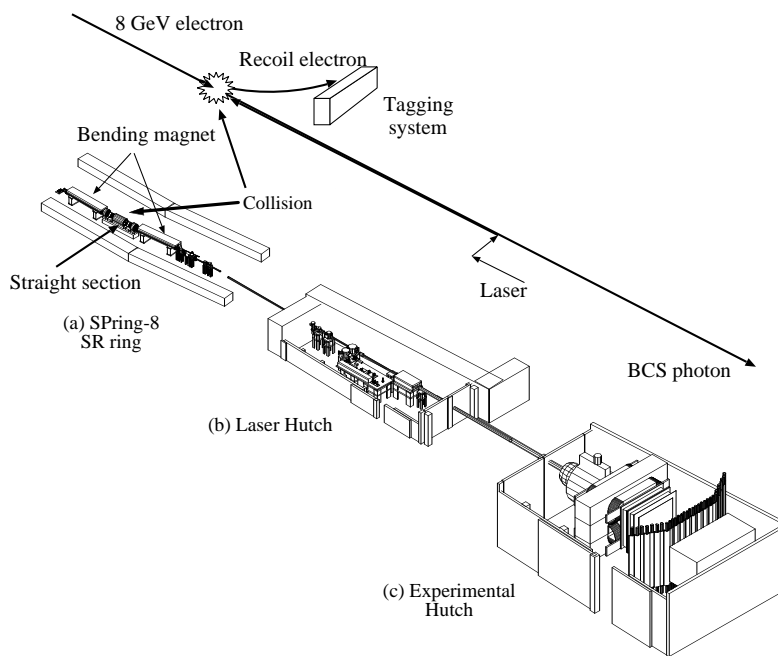


Figure 2.1: Schematic view of the LEPS facility at SPring-8. The facility consists of
three parts:(a) laser-electron collision part in the storage (SR) ring, (b) laser hutch
for a laser injection, and (c) experimental hutch. A schematic explanation of the
collision between an electron and a laser photon in backward-Compton scattering is
inserted in the figure.

Laser photons optimized in the laser hutch are injected to the storage ring. There is a 7.8 m long straight section between two bending magnets in the storage ring as shown in Fig. 2.1. In this straight section, the BCS process takes place if a laser photon collides with a 8-GeV electron. Photons produced by the BCS process are provided to the experimental hutch and irradiate a target. The recoiled electrons are detected by a tagging system placed at the exit of the bending magnet to measure the photon energy.

## 2.1.1 Backward Compton scattering

The backward-Compton-scattering process is well understood by the quantum electrodynamics. Fig. 2.2 shows the kinematical variables of the backward-Compton-scattering process. If a laser photon with an energy $k_1$ strikes an electron with a high energy $E_e$ with a relative angle $\theta_1 \simeq 180°$, it is scattered with a scattering angle of $\theta_2$. The energy of a BCS photon $E_\gamma$ is described as

$$E_\gamma = k_1 \frac{1 - \beta \cos \theta_1}{1 - \beta \cos \theta_2 + \frac{k_1(1-\cos \theta)}{E_e}}, \tag{2.1}$$

where $\beta$ is an incident electron velocity in unit of the speed of light and $\theta = \theta_2 - \theta_1$.
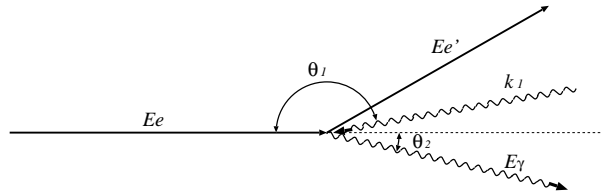


Figure 2.2: Kinematical variables of the backward-Compton-scattering process in the laboratory frame.

In the present experiment, a linear-polarized photon beam was produced by an Ar laser with a 351 nm wavelength. The differential cross section and the polarization for 275 nm, 351 nm and 488 nm laser are shown in Fig. 2.3.
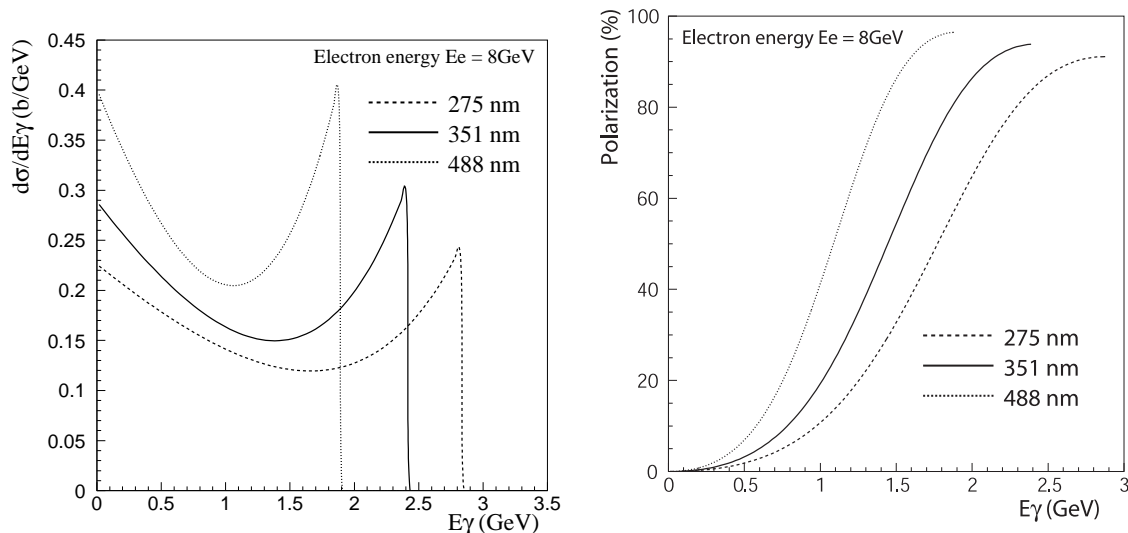
Figure 2.3: Left: Differential cross section of BCS process. Right: Polarization as a function of the photon energy.

## 2.1.2   Laser operating system

Fig. 2.4 shows the laser-operating system placed in the laser hutch (see Fig. 2.1). The operating system consists of an Ar laser, a half-wave-length plate ($\lambda/2$ plate), a beam expander, four mirrors and a polarization monitor. The direction, shape, and polarization of laser photons are controlled by this system to achieve high intensity and a high polarization of the $\gamma$-ray photon beam. The laser photons pass through the $\lambda/2$ plate to change the direction of the polarization. The shape of the laser beam is tuned by the beam expander. The direction and position of the laser beam are tuned by the third and forth mirrors. The laser beam is transferred to the beam line by the first and second mirrors. The polarization monitor is placed at the upstream of the collision part in the storage ring to measure laser photons which do not collide with the 8-GeV electrons.
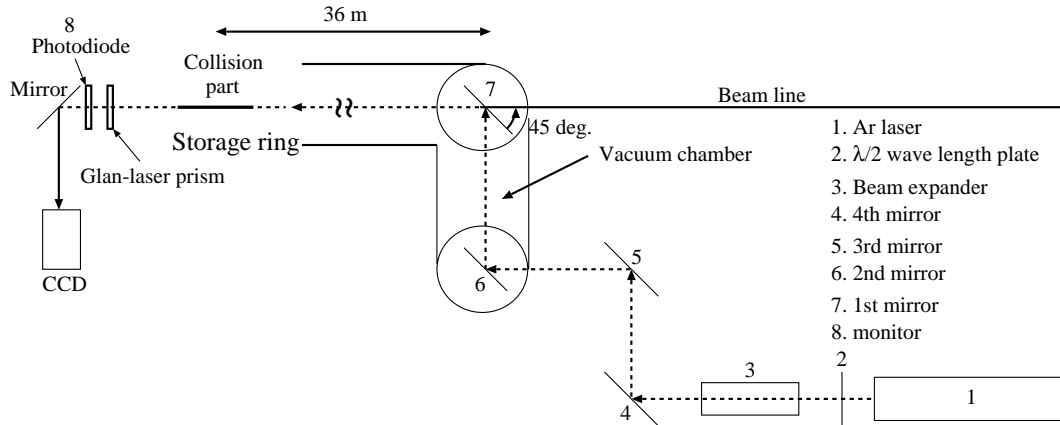
Figure 2.4: Schematic view of the laser operation system.

## 2.1.3 Energy tagging system

The energy of a $\gamma$-ray photon, $E_\gamma$, is obtained from the energy of the recoiled electron, $E_{e'}$, as $E_\gamma = E_e - E_{e'}$. The energy of the circulating electron in the storage ring, $E_e$, was calculated using the measured field distributions of magnets to be $7.975 \pm 0.003$ GeV [50]. The energy $E_{e'}$ is measured by a tagging system (TAG) located in the storage ring. Since the electron scattered by the BCS process loses its energy, it is strongly bent and deviates from the normal orbit in the 8-GeV ring when it passes through the bending magnet placed at the end of the straight section.

Fig. 2.5 shows the structure of the tagging system. The tagging system is placed at the outside of a vacuum pipe of the 8 GeV-electron storage ring. The tagging system covers a region, 4.5-6.5 GeV, in the energy of recoiled electrons. This energy region corresponds to the range of 1.5-3.5 GeV for the $\gamma$-ray photons.
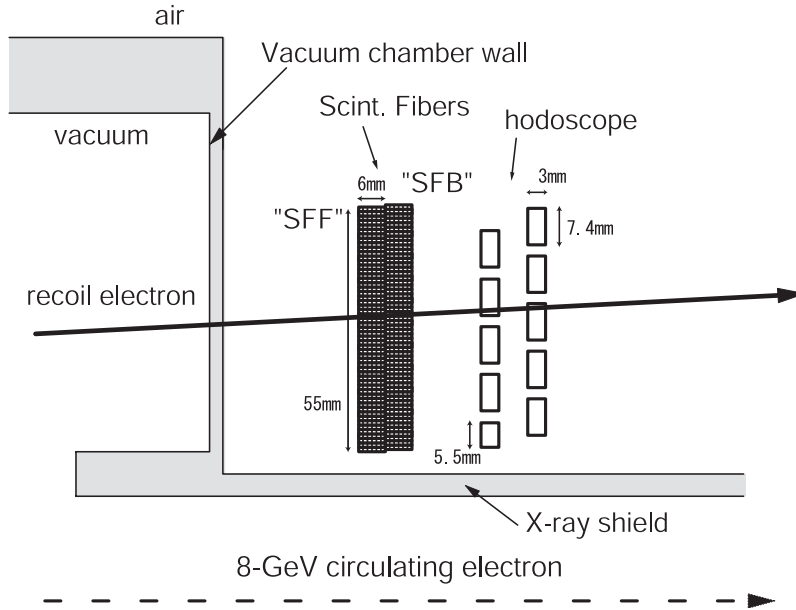
Figure 2.5: Schematic view of the tagging system.

The tagging system consists of the plastic scintillator (TAG-PL) hodoscope and the scintillating fibers as shown in Fig. 2.5. There are one layer of the TAG-PL hodoscope and two layers of the scintillating fibers. The TAG-PL hodoscope consists of 2 layers of 5 plastic scintillation counters. The size of the plastic scintillator is 10.0 mm high, 7.4 mm wide, and 3.0 mm thick. The plastic scintillator which is closest to the 8-GeV electron beam, placed in the upstream layer, has the width of 5.5 mm. The plastic scintillators are arranged with an overlap of 2.7 mm as illustrated in Fig. 2.5. The signal of the TAG-PL was read through the photo-multiplier-tube (PMT) of a 3/8 inch diameter (HAMAMATSU H3164-10). The hit position of a recoil electron is measured by two scintillating fiber layers (TAG-SFB and TAG-SFF). Each fiber layer consists of 55 fiber bundles. Each fiber bundle is made of six fibers with the cross section of $1 \times 1$ mm$^2$. Each fiber bundle was read through the PMT (HAMAMATSU R5900-00-M4, H6568-10). The trajectory of the recoiled electron was reconstructed using the hit position in two fiber layers. Then, a hit associated with the track was searched in the TAG-PL hodoscope. If the associated hit is found, we obtain the energy $E_{e'}$ from the hit positions in the fiber layer. Finally, the photon energy is obtained using $E_{e'}$.

## 2.1.4   Beam line setup

The $\gamma$-ray beam travels from the collision point to the experimental hutch through the laser hutch. Fig. 2.6 illustrates the setup of the beam line.
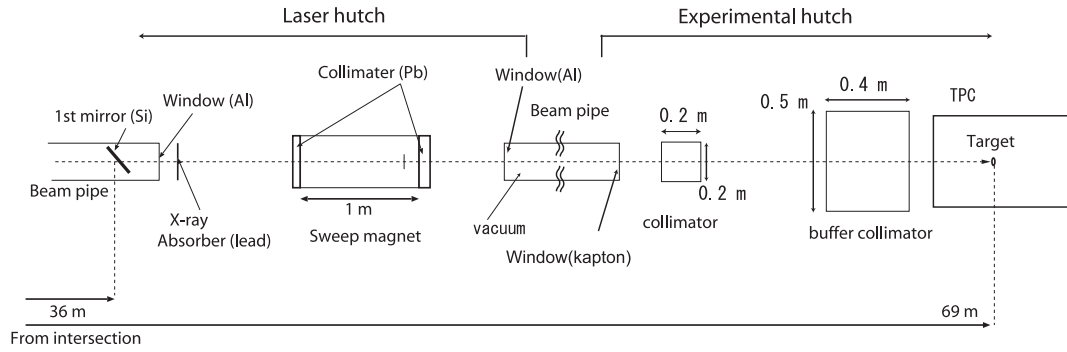


Figure 2.6: Schematic view of the LEPS beam line setup.

There are some materials in the path of the photon beam: the first mirror, aluminum and kapton windows of the beam pipes, the X-ray absorber, collimators and air in the laser and experimental hatch. When the photon beam hits these materials, some of photons are converted to $e^+e^-$ pairs. The materials and their conversion rate to $e^+e^-$ pairs are summarized in Table 2.1. The first mirror is made of silicon with a thickness of 6 mm. The mirror is tilted by 45° to inject laser photons into the storage ring. Aluminum plates with a thickness of 0.55 mm are used as windows of beam pipes at the exit of the beam pipe from the SR ring and the entrance window of a beam pipe which connects the laser hutch and experimental hutch. At the exit of the beam pipe in the experimental hatch a kapton (polyimide) membrane of 78 $\mu$m thick was used as a window. An absorber made of 2.0 mm-thick lead is placed after the beam pipe from the SR ring in order to absorb X-rays. The detectors of the spectrometer are protected with this absorber from a radiation damage. The thickness of 2.0 mm is determined by the operation of the detectors and the radiation safety.

Table 2.1: Materials inserted in the beam line.

|  | Material | Radiation length (mm) | Thickness (mm) | Conversion rate (%) |
|---|---|---|---|---|
| First mirror | Si | 93.6 | 8.4 | 11.0 |
| Vacuum windows | Al | 89.0 | 1.1 | 1.6 |
| Vacuum window | kapton | 283 | 0.078 | 0.035 |
| Air |  | 304200 | ~4000 | ~1.3 |
| Absorber | Pb | 5.6 | 2.0 | 36.8 |

In order to remove the $e^+e^-$ pairs, we use a sweep magnet located in the laser hutch. The size of the iron yoke is 176 mm high, 560 mm wide, and 1000 mm long. Two permanent magnets are installed in the iron yoke. The size of each magnet is 35 mm high, 58 mm wide, and 1000 mm long. They are faced with a gap of 44 mm. The strength of the magnetic field is 0.6 T at the center. The $e^+e^-$ pairs produced at the first mirror, the aluminum window, the X-ray absorber and air are removed from the beam line by the sweep magnet. Lead collimators are placed at the upstream and downstream positions of the sweep magnet. The thickness of the upstream (downstream) collimator is 50 (150) mm. The upstream (downstream) collimator has a hole with a diameter of 20 (25) mm. The $e^+$ or $e^-$ with a momentum below 2.1 GeV/c are blocked by the downstream collimator. The $e^+$ or $e^-$ with a momentum above 2.1 GeV/c pass through the hole of the downstream collimator.

The photon beam was collimated further in the experimental hatch to pass through the target holder. The photon beam distributes widely in horizontal direction up to 30 mm at the target because the horizontal divergence of the electron beam is large due to the bending magnet at the upstream of the straight section. The diameter of the target holder is set as 25 mm to detect short track of low momentum hyperons. Two collimators made of lead blocks were used to make the beam narrower, referred to as the shield collimator and the buffer collimator. The shield collimator has the aperture of 23 mm in diameter, the thickness of 200 mm and the area of $200 \times 200$ mm$^2$. The photons in the peripheral part of the beam are converted to $e^+e^-$ pairs by the shield collimator, and the primary $e^+e^-$ pairs make an electromagnetic shower. The electromagnetic shower develops and eventually becomes less energetic in the shield collimator. The buffer collimator, with the aperture of 24 mm in diameter, 400 mm thick and $500 \times 500$ mm$^2$ area, was installed at about 2 m downstream of the shield collimator. The buffer collimator was used to absorb electromagnetic shower. The photon beam does not interact with the buffer collimator because the beam size is made to be smaller than the aperture. The shield and buffer collimators were designed to minimize the background events in the TPC.

## 2.2  Nuclear targets

Nuclear targets of $CH_2$, carbon and copper were used in the experiment. The data with the $CH_2$ and carbon targets were used for the measurement of $\Lambda(1405)$ and $\Sigma^0(1385)$ photoproduction. Fig. 2.7 shows pictures of the targets.
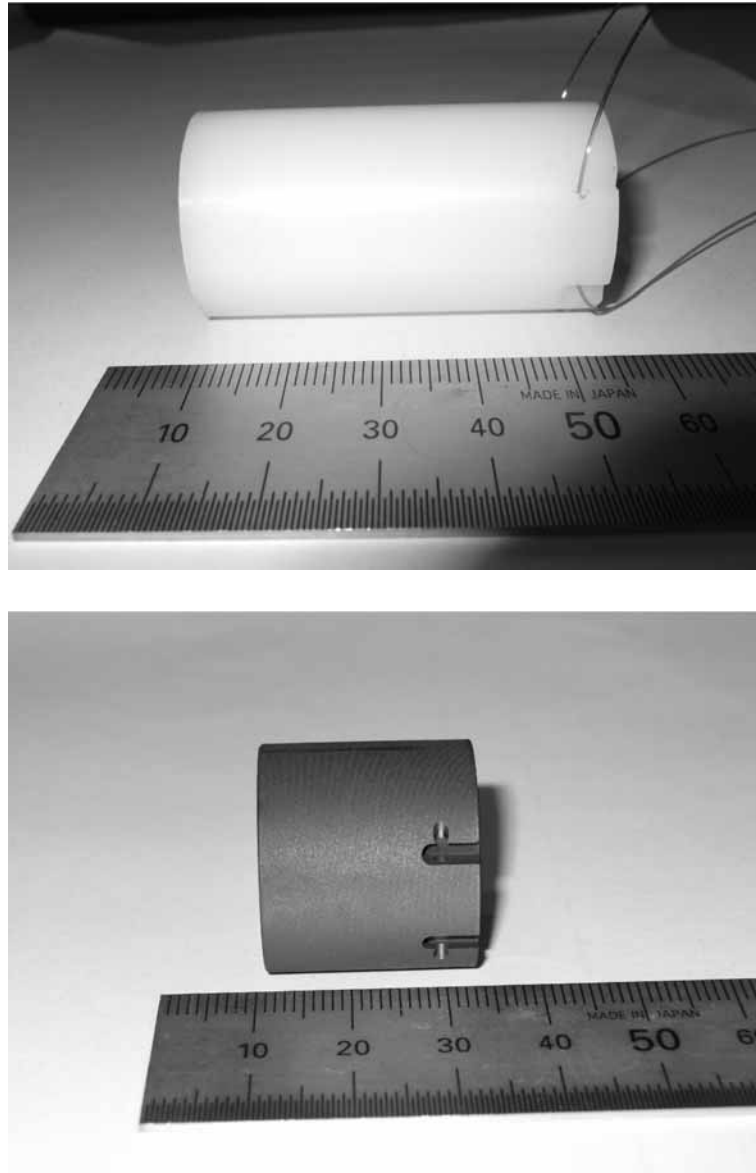




Figure 2.7: Pictures of nuclear targets: $CH_2$ (top) and carbon (bottom).

The diameters of the targets were 25 mm, and the thickness of the targets was set to 0.1 radiation length: 47 mm for $CH_2$, 22.4 mm for carbon and 1.4 mm for copper.

## 2.3   LEPS spectrometer

The $K^+$'s produced by the $\gamma p \rightarrow K^+ X$ reaction were identified by the mass obtained from the momentum and velocity measured with the spectrometer (LEPS spectrometer) located at the downstream of the target.
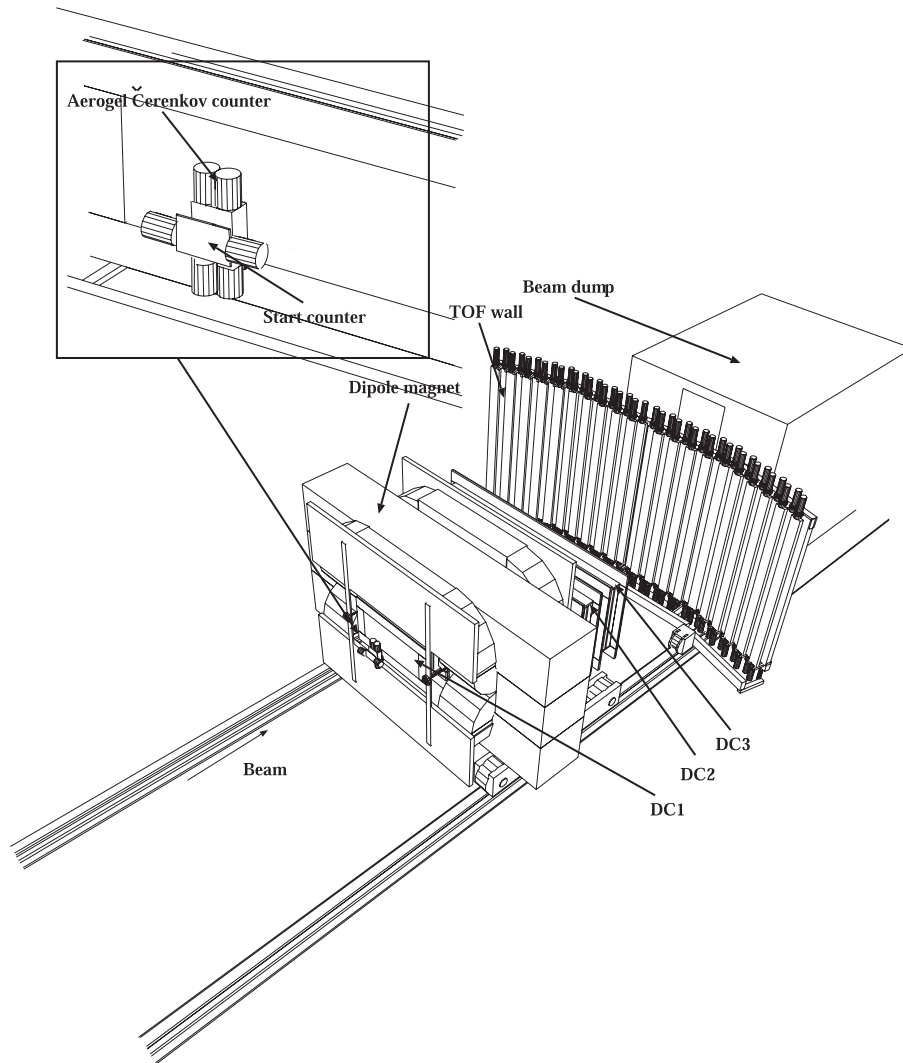
Figure 2.8: Overview of the LEPS spectrometer.

The LEPS spectrometer consists of an upstream-veto counter, a start counter, a silica-aerogel Čerenkov counter, a dipole magnet, three drift chambers (DC1, DC2 and DC3), and a TOF wall. Charged particles produced at the target and entered into the aperture of the dipole magnet were identified by the start counter. The silica-aerogel Čerenkov counter was used to eliminate the $e^+e^-$ background events.

Three drift chambers were used as tracking devices with the dipole magnet to measure momenta of charged particles. The velocity of the particle was obtained using the time-of-flight from the target to the TOF wall and the path length of the trajectory.

## 2.3.1 Upstream-veto counter

The photon beam is partly converted to $e^+e^-$ pairs until achieving to the target in the air in the beam line, Al windows of the beam pipe or the collimators. These $e^+e^-$ pairs were identified using the upstream veto counter, and vetoed at the trigger level. This counter is a plastic scintillator (kuraray-SCSN-81) located at just downstream of the buffer collimator in the experimental hatch. The size is 620 mm high, 620 mm wide, and 3 mm thick. A 2-inch fine-mesh PMT (HAMAMATSU H6614) is connected to the plastic scintillator through a light guide.

## 2.3.2 Start counter (SC)

The start counter (SC) is a plastic scintillation counter located at the position of 667 mm downstream from the center of the target to identify the charged particles which were produced at the target and entered into the aperture of the dipole magnet. Fig. 2.9 shows a schematic drawing of the SC. The size of the plastic scintillator is 190 mm high, 370 mm wide, and 5 mm thick. Two 2-inch-diameter fine-mesh PMT's (HAMAMATSU H6614) are connected to the left and right sides of the plastic scintillator through light guides. The start counter is used as a reference counter to measure the time-of-flight with the RF signals.
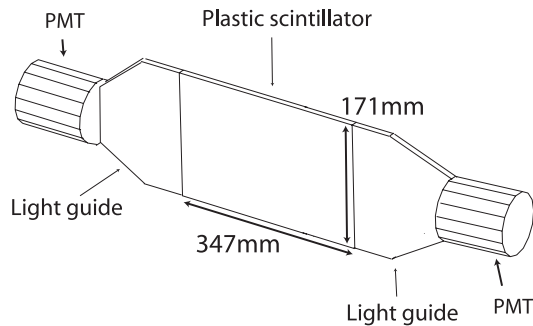


Figure 2.9: Schematic drawing of the start counter.

### 2.3.3   Silica-aerogel Čerenkov counter

Main background events in a measurement of hadronic reactions were the $e^+e^-$ pairs produced at the target and at the SC. An aerogel Čerenkov counter (AC) was used to reject the $e^+e^-$ production events at the trigger level. The AC consists of two sheets of silica aerogel radiators with a refractive index of 1.03, which are covered by a box made of black paper. Each radiator has a volume of 110(W)×25(T)×110(H) mm$^3$. White sheets of Gortex were spread over the inner surface of the box as a random reflector. Fig. 2.10 shows a schematic view of the aerogel Čerenkov counter.
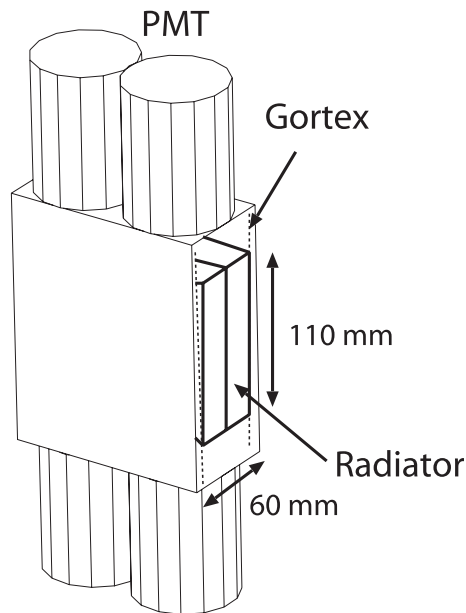


Figure 2.10: Silica aerogel Čerenkov counter (AC).

The threshold momenta of Čerenkov radiation for $e^+e^-$, pion and kaon are 0.002 GeV/c, 0.57 GeV/c and 2.0 GeV/c, respectively. The AC was installed just downstream of the start counter to detect both an electron and a positron simultaneously. The collected lights were read by four 2-inch fine-mesh PMT's (HAMAMATSU H6614), which were connected to the upper and lower sides of the box.

### 2.3.4 Drift chambers

The trajectory of a charged particle was reconstructed using hit information from the three drift chambers. The DC1 was located upstream of the dipole magnet. It has the active area of $600 \times 300$ mm$^2$. Fig. 2.11 shows a schematic drawing of the wire configuration in the DC1.
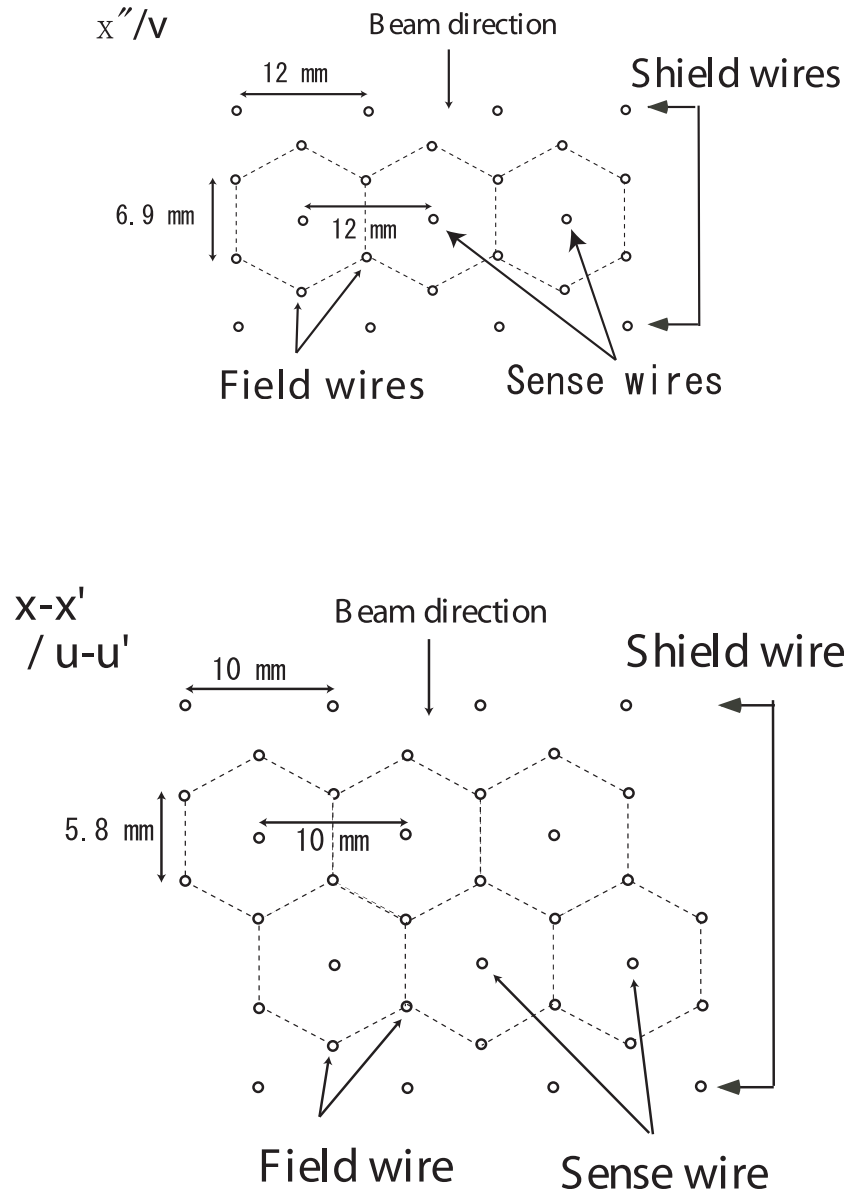


Figure 2.11: Schematic drawing of the wire configuration in the drift chambers.

The DC1 has 6 planes, x, x', u, u', v and x". The wire spacing was 6 mm for x-x'

and u-u' plane and 12 mm for x" and v plane. The field wires are arranged in a hexagonal shape. The shield wires are positioned along the windows to shape the electric field. The orientation of the u and v wires is 45° with respect to the vertical plane.

The DC2 and DC3 were installed downstream of the dipole magnet and have the active area of $2000 \times 800$ mm$^2$. Both DC2 and DC3 have 5 planes, x, x', u, u' and v. The design of DC2 and DC3 is similar to that of DC1 as shown in Fig. 2.11, but there is no x" wires in DC2 and DC3. Sense wires of x-x' and u-u' are positioned with a 10 mm spacing, and the wires of v are positioned with a 20 mm spacing. The u and v direction are oriented at angles 30° with respect to the vertical plane. The material of the sense wires is gold-plated tungsten (Au-W) and the wire diameter is 25 and 30 $\mu$m for DC1 and DC2, DC3, respectively. The field and shield wires are made of Au-BeCu with a diameter of 100 $\mu$m. The design parameters of the DC's are shown in Table 2.2. The gas mixture used to operate the DC's was 70 % argon and 30 % isobutane. The spatial resolution and detection efficiency were obtained using proton tracks. The spatial resolution of the DC's was found to be approximately 200 $\mu$m, and the detection efficiency was more than 95%.

Table 2.2: Design parameters of the DC's. The location of the center of each DC along the z-axis is measured from the center of the dipole magnet.

|       | Plane | Orientation | # of sense wires | Wire spacing (mm) | Active area x $\times$ y (mm$^2$) | Location z (mm) |
|-------|-------|-------------|------------------|-------------------|-----------------------------------|-----------------|
| DC1   | x-x'  | 0°          | 48×2             | 6                 | 600 $\times$ 300                  | -466.0          |
|       | u-u'  | +45°        | 48×2             | 6                 |                                   |                 |
|       | v     | -45°        | 48               | 12                |                                   |                 |
|       | x"    | 0°          | 48               | 12                |                                   |                 |
| DC2   | x-x'  | 0°          | 104×2            | 10                | 2000 $\times$ 800                 | 860.5           |
|       | u-u'  | +30°        | 78×2             | 10                |                                   |                 |
|       | v     | -30°        | 79               | 20                |                                   |                 |
| DC3   | x-x'  | 0°          | 104×2            | 10                | 2000 $\times$ 800                 | 1260.5          |
|       | u-u'  | +30°        | 78×2             | 10                |                                   |                 |
|       | v     | -30°        | 79               | 20                |                                   |                 |

## 2.3.5    Dipole magnet

The dipole magnet was used as a momentum analyzer magnet to bend charged particles. The magnet is placed at the center of the spectrometer. The magnet has an aperture with 55 cm high and 135 cm wide. The length of the pole along the beam is 60 cm.
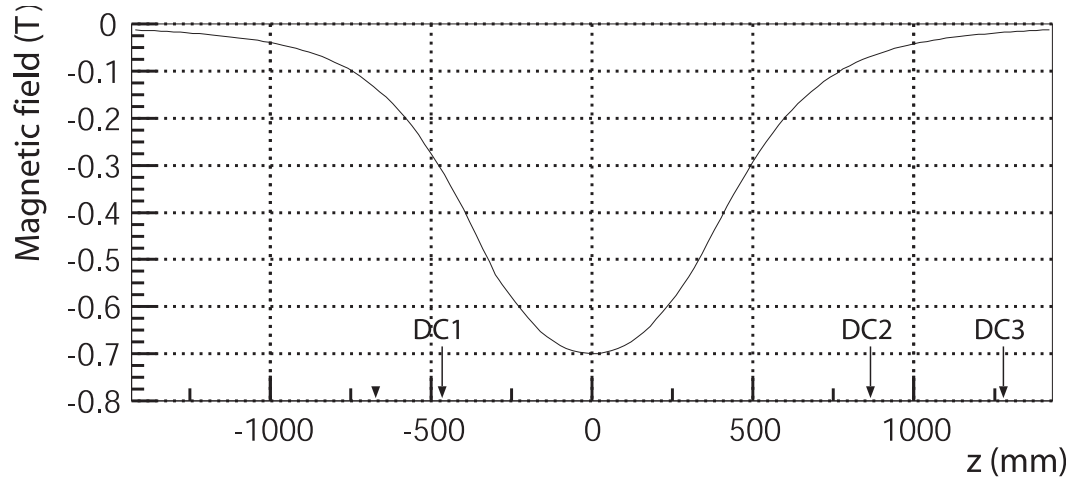


Figure 2.12: Distribution of the magnetic field $B_y$ as a function of the z-position at x=0 and y=0. The position of z=0 corresponds to the center of the dipole magnet.

Fig. 2.12 shows the distribution of the magnetic field $B_y$ along the y-direction as a function of the z-axis at x=0 and y=0. We used the RADIA simulation program to obtain the distribution [51]. The magnetic field was measured with a hole probe and the measured distribution was compared with the result obtained by the RADIA simulation. They show a good agreement and then we used the distribution of the magnetic field obtained by RADIA in the tracking. The direction of the magnetic field is from up to down. The strength of the magnetic field is 0.7 Tesla at the center.

## 2.3.6   TOF wall

The time-of-flight of a charged particle was measured using the TOF wall. The TOF wall was placed downstream of the DC3 which determined the angular coverage of the LEPS spectrometer.
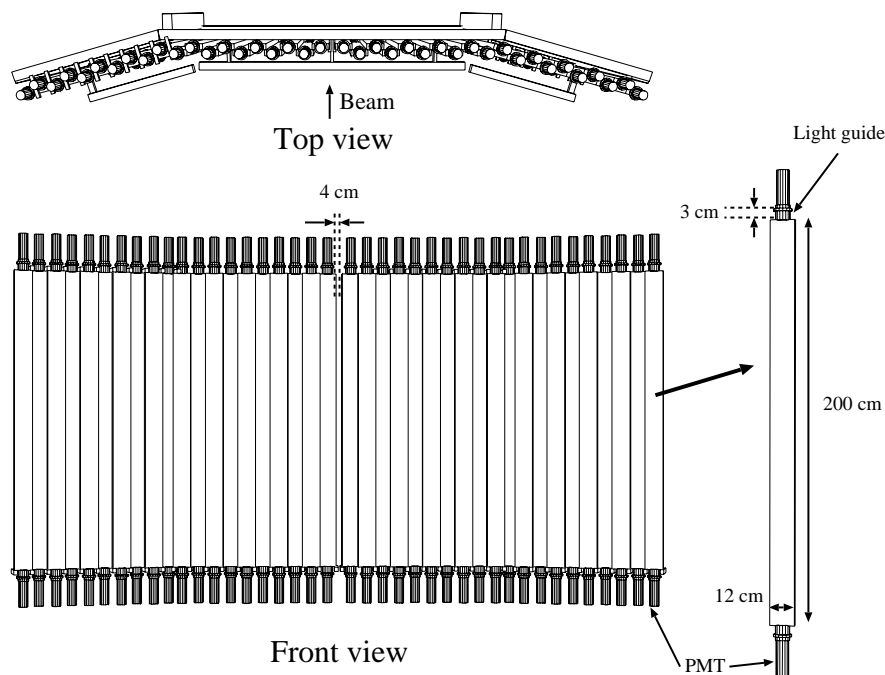


Figure 2.13: Drawing of the TOF wall.

Fig. 2.13 shows a schematic view of the TOF wall and drawing of a TOF counter. The TOF wall consists of 40 plastic scintillator bars (BC-408). The size of a plastic scintillator bar (TOF counter) is 200 cm long, 12 cm wide, and 4 cm thick. Two 2-inch PMT's (HAMAMATSU H7195) are attached to both sides through a light guide with a thickness of 3 cm. Each bar is overlapped with adjacent bars by 1 cm. Sideway bars are aligned in the planes tilted by $\pm$ 15 degrees as shown in the top view of Fig. 2.13. Ten bars are arranged in the right side and ten bars are placed in the left side. A 4-cm gap between the two TOF counters at the center allows for the photon beam to pass through. In the present experiment, the z-position of the TOF wall was set at 3151.5 mm away from the center of the dipole magnet.

## 2.4  Time Projection Chamber

A time projection chamber (TPC) was used to detect decay products from hyperon resonances. In this section, the mechanical design and operation of the TPC is described. Fig. 2.14 shows a schematic drawing of the TPC. One of the features of this TPC is to detect the decay topology of a low momentum hyperon, $\Lambda$ or $\Sigma$, which was produced from the decay of hyperon resonances. A typical flight length of $\Sigma^-$ hyperons is a few cm. In order to detect such a short track, the target was installed in the TPC, and the trajectory of the particle was measured at the distance of 1.6 cm from the center of the target. The TPC has a cylindrical active volume of 195 mm in radius and 730 mm in length. The signals are read through 1055 cathode pads arranged as concentric circles. It was operated with an argon-methane (90% : 10%) gas mixture (p10 gas) at atmospheric pressure and provides 14 three-dimensional coordinate measurements and energy-deposition information for fully contained tracks.
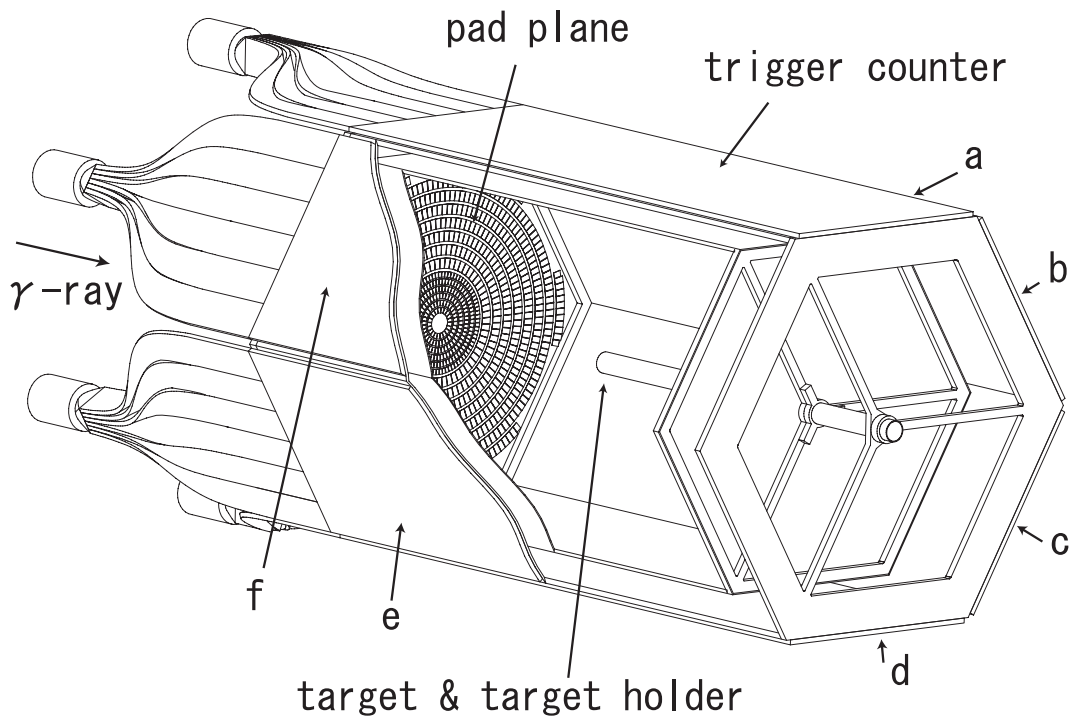


Figure 2.14: Schematic view of the TPC. The arrows (a to f) indicate the trigger counters.

### 2.4.1   Field cage

A charged particle traversing the active volume of the TPC ionizes electrons and ions from argon atoms. The electrons from the primary ionization drift up to 0.77 m towards the upstream end-plate in an axial magnetic field of 2.0 T and an electrical field of 180 V/cm pointing parallel to the magnetic field in the TPC. The electric field is formed by the high voltage membrane and field strips embedded on the inner and outer sides of the field cage and on the target holder. Fig. 2.15 shows a picture of the field cage, which has a hexagonal prism shape with 500 mm in diameter and 730 mm in length.



Figure 2.15: Picture of the field cage.

The high voltage membrane is made of a copper-coated kapton. It is located at the downstream end of the active volume. The field cage consists of six 1.6 mm-thick G10 plates. On both side of the plate copper strips of 35 $\mu$m thick and 8 mm wide are embedded. The electrodes are connected to a resister chain ($138 \times 1$ M$\Omega$) mounted on the outside of the cage. The target holder is a 1 mm-thick cylinder made of G10, and is put in the active volume of the TPC. The outer surface of the cylinder is covered with copper strips to form the electric field. Fig. 2.16 shows a picture of the target holder. The field cage was operated with high voltage of 12.3 kV corresponding to an electric field of 180 V/cm.
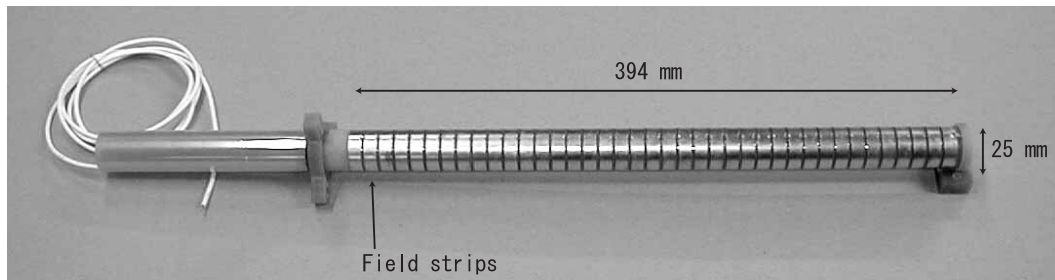


Figure 2.16: Picture of the target holder.

A simulation of the electric field in the TPC was performed using GARFIELD [52]. In the simulation, the high voltage membrane, the field strips, the target holder, the shield and sense wires, and the cathode pad plane were included. The length of the field cage in the z-direction was shorter than the real length because the memory size was not sufficiently large to include all strips on the field cage. The equipotential contour plot obtained by the simulation is shown in Fig. 2.17.
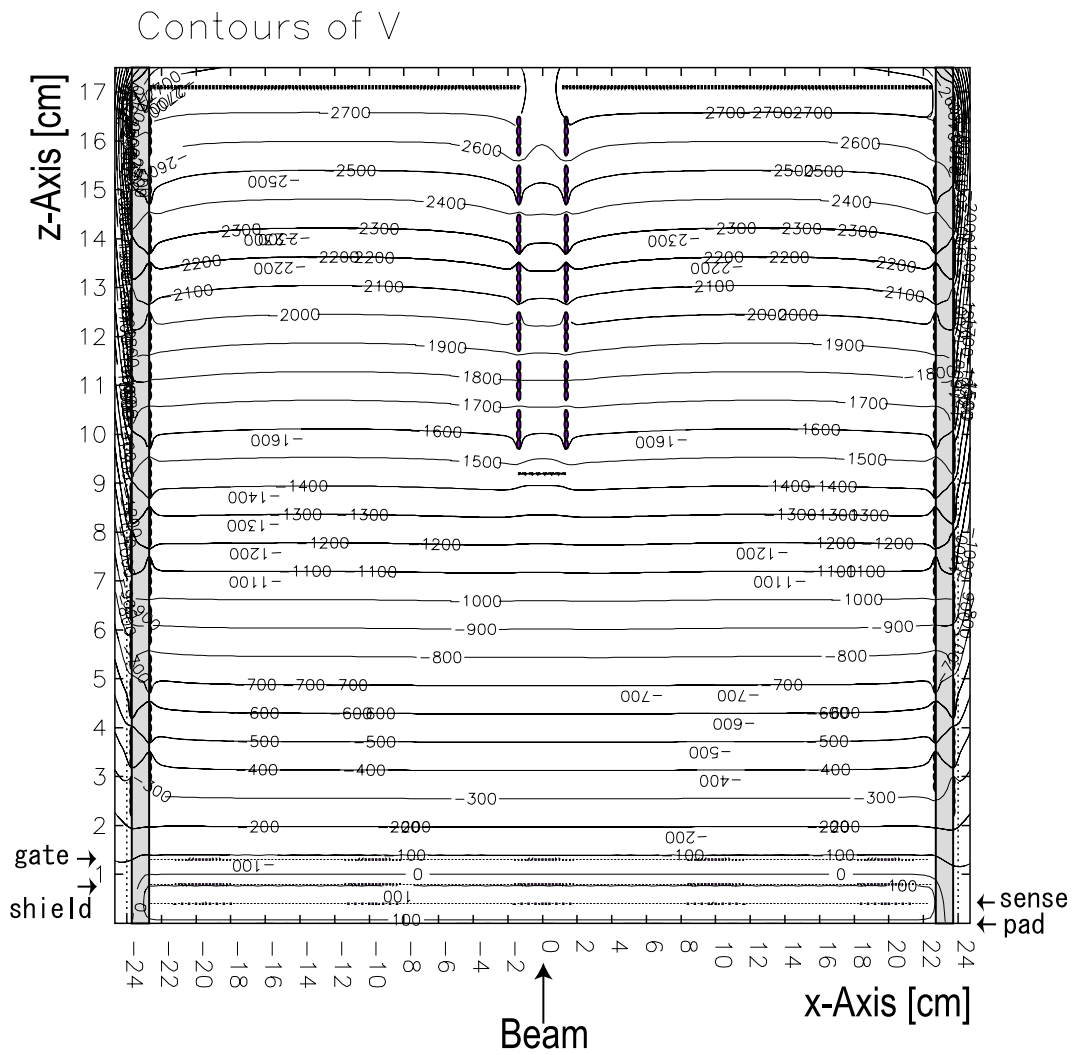
Figure 2.17: Schematic view of the equipotential lines in the TPC, where z-coordinate is not scaled.

## 2.4.2   Gas amplification part

The gas amplification part of the TPC consists of a gate-wire grid, a shield-wire grid, a sense-wire grid and a cathode pad plane. Fig. 2.18 shows a schematic drawing of the gas amplification part.
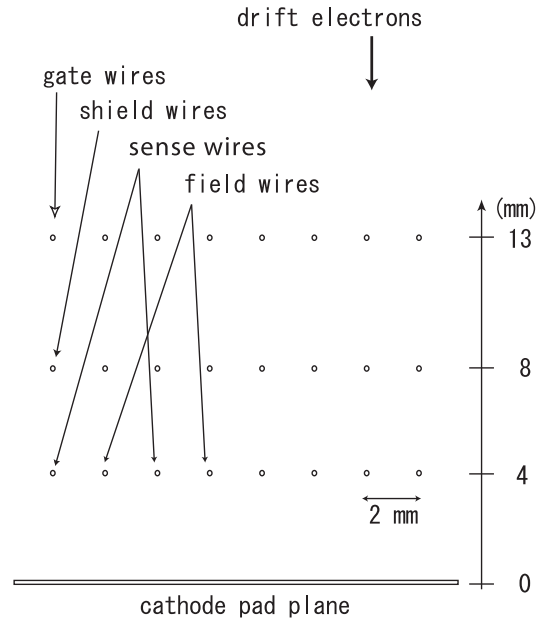


Figure 2.18: Schematic view of the gas amplification part of the TPC.

**Gate-wire grid**

The gate-wire grid was used to prevent electrons ionized by mainly synchrotron X-rays from reaching the sense-wire region. When the gate was closed, the voltage of the gate wires was set to be $-290$ V/$-110$ V alternately, and the gate wires absorb the electrons. Fig. 2.19 shows the trajectory of electrons when the gate is closed. The voltage was determined to minimize the current on the sense wires. When the trigger signal comes, the voltage is set to $-90$ V, and the gate is opened for 25 $\mu$sec.
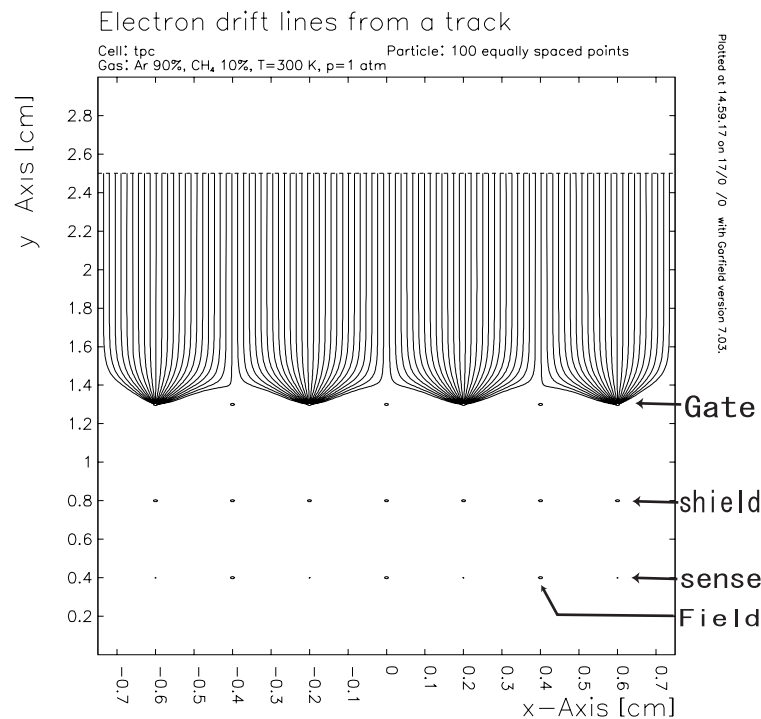
Figure 2.19: Drift line of electrons when gate is closed.

## Shield and sense wire grid

The shield wires were set to be 0 V to form the electric field in the avalanche region. The photon beam is injected to the active volume around $x \sim 0$ in Fig. 2.17, where no cathode pad is arranged but anode wires are stretched. The X-rays and electron positron pairs near the beam axis ionize argon or methane atoms to the electron ion pairs in the gas. The amount of ionized electrons in this region was too large to operate the chamber. In order to prevent these ionized electrons from entering into the avalanche region, a carbon plate with a thickness of 100 $\mu$m and diameter of 26.5 mm was put on the shield wires.

The sense and field wires were stretched alternately with 4 mm spacing and glued with epoxy resin on the frame of G10 material. The voltage of the sense wires was set to be +1.62 kV. In order to avoid an electric discharge between the sense and field wire, the voltage of the field wires were set to +220 V. Characteristics of the wire grids are summarized in Table 2.3.

Table 2.3: Characteristics of the wire grids.

|  | Material | diameter ($\mu$m) | Wire spacing (mm) | Distance from pad plane (mm) | # of wires | Applied voltage (kV) |
|---|---|---|---|---|---|---|
| sense | Au-W | 20 | 4 | 4 | 95 | +1.62 |
| field | Au-BeCu | 100 | 4 | 4 | 96 | +0.22 |
| shield | Au-BeCu | 100 | 2 | 8 | 191 | 0 |
| gate | Au-BeCu | 100 | 2 | 13 | 191 | -0.90 (open) -0.29/-0.11 (close) |

**Cathode pad plane**

In the vicinity of a sense wire, the electrons create an avalanche and induce signals
on the cathode pads. The signals are read through cathode pads which are arranged
as 14 concentric circles. There are two different sizes of pad: 6 rows of $4.5 \times 7.0$ mm$^2$
pads which span from 16.5 to 61.5 mm in radii and 8 rows of $7.5 \times 13.0$ mm$^2$ pads
are located from 75.5 to 194.5 mm in radii. The total number of pads are 1055. The
configuration of the pad plane is shown in Fig. 2.20. The wires are stretched in one
direction as indicated by the arrow in Fig. 2.20.
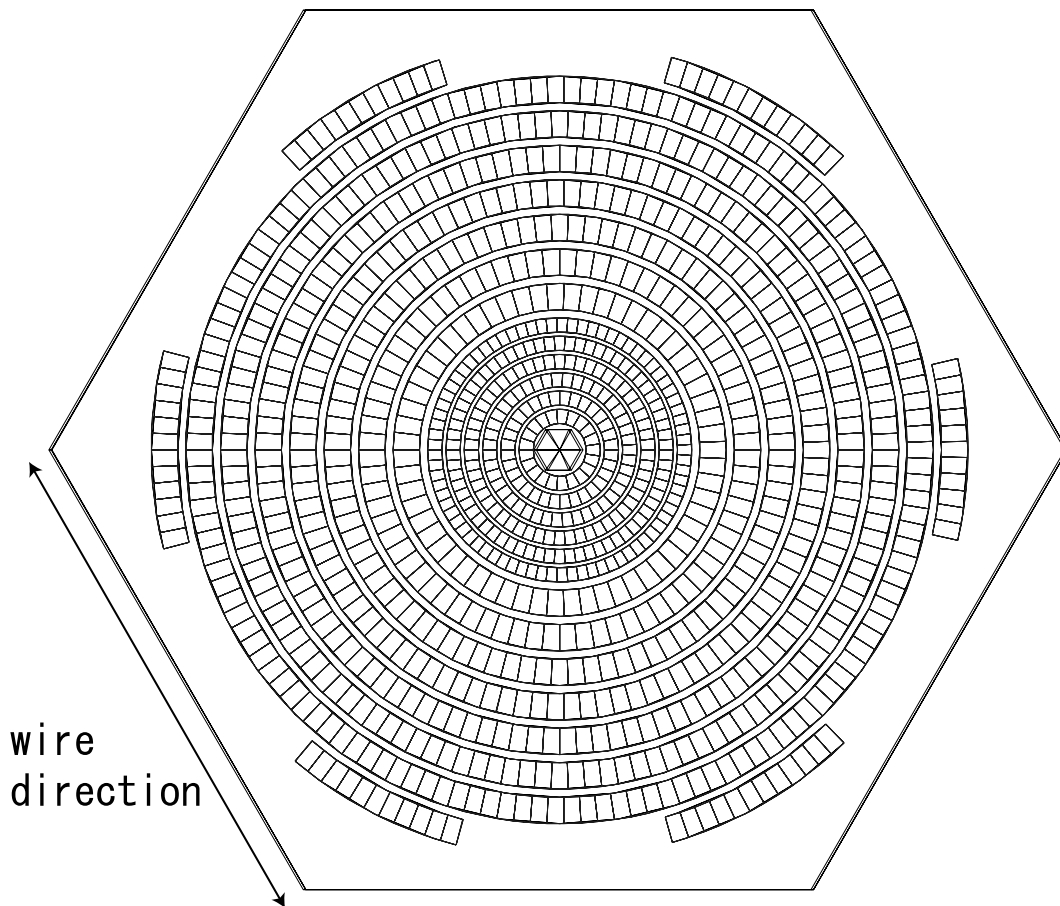


Figure 2.20: Schematic drawing of pad rows.

Fig. 2.21 shows a sample of event measured by the TPC. The cathode pads are shown in green. The pads with signals are shown in gray in the pad plane. These pads are shifted in the drift direction using the drift time information as shown as the red and blue rectangles. The azimuthal coordinate along the pad row is obtained from the center-of-gravity of induced charges on pads, whereas longitudinal coordinate is obtained from their measured drift times. The details on the measurement of the coordinate is described in section 3.2.
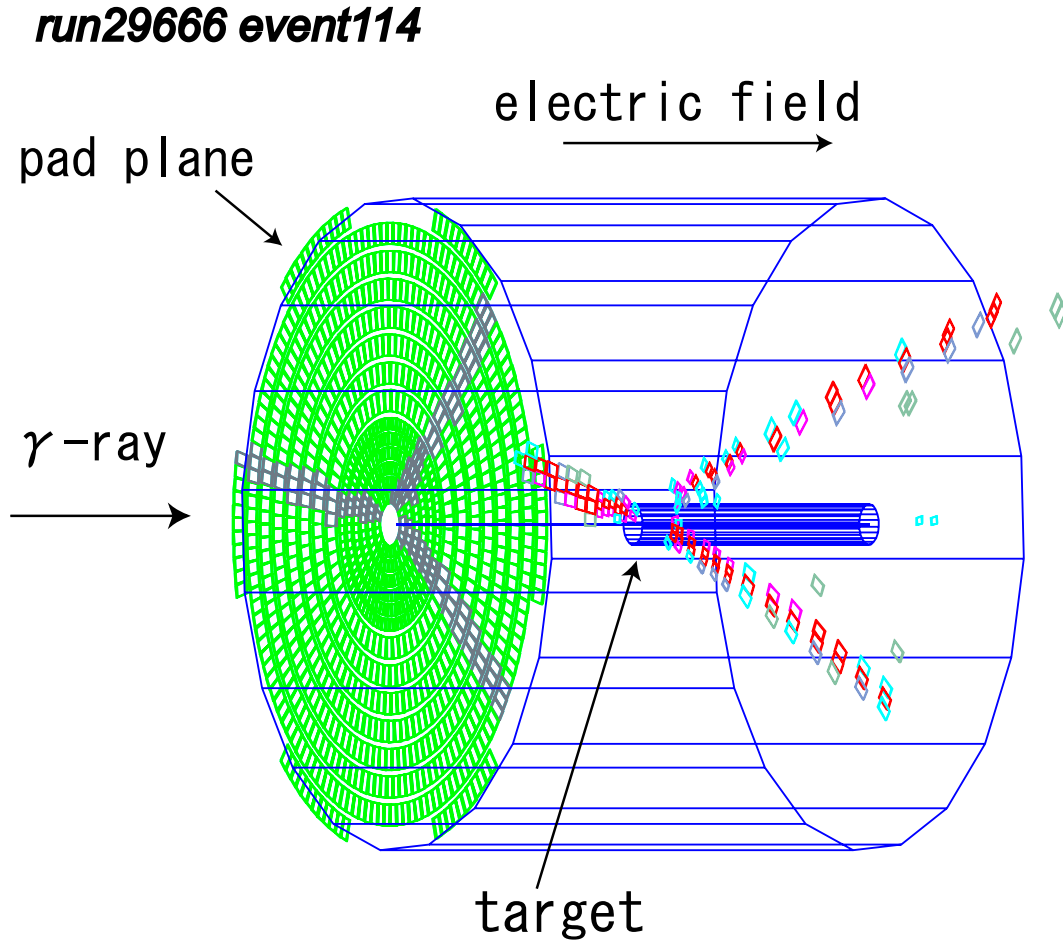


Figure 2.21: A sample of event measured by the TPC. The cathode pads are shown in green. The pads with signals are shown in gray in the pad plane. These pads are shifted in the drift direction using the drift time information as shown as the red and blue rectangles.

Fig. 2.22 shows distributions of the tracking residuals in the azimuthal direction (left) and drift direction (right) obtained using cosmic ray tracks. The typical spatial resolutions were obtained to be $\sim 400$ $\mu$m in the pad plane and $\sim 800$ $\mu$m in the drift direction. The details on the spatial resolutions and detection efficiency are described in Appendix B. The hit coordinate in the drift direction for the most inner layer could not be obtained correctly due to the distortion of the electric field by the target holder, and the signals from the most inner layer were not used for the track reconstruction. The signals from the most outer layer (14th layer) were also not used for the track reconstruction because the 14th layer is arranged only in the corners of the TPC, and the improvement of the momentum resolution is negligible.
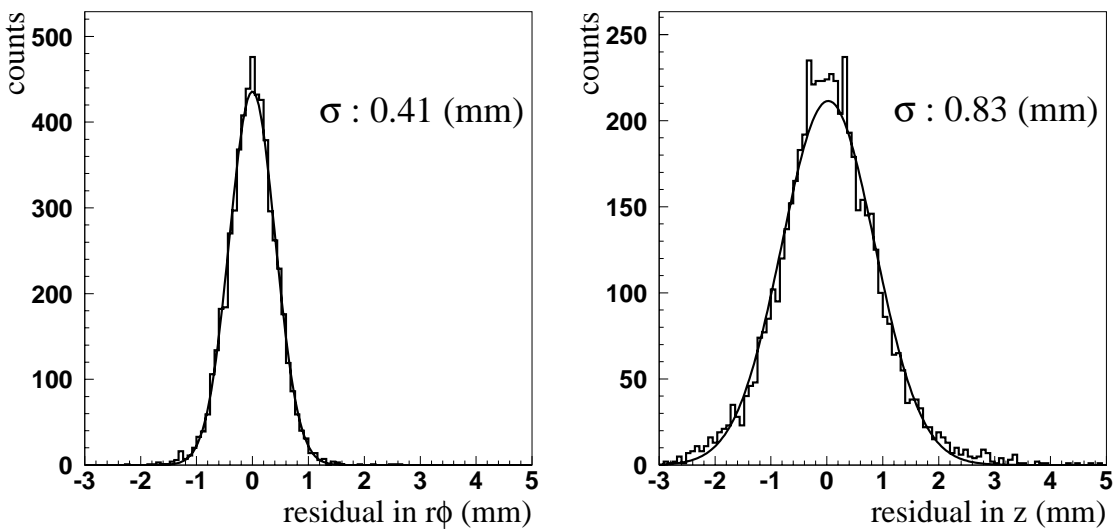


Figure 2.22: Distributions of the tracking residuals in the azimuthal direction (left) and drift direction (right).

## 2.4.3  Trigger counters

The TPC was surrounded by ten scintillation counters (ELJEN EL-200) to detect charged particles passing through the active volume of the TPC. Six scintillation counters (TPC-SIDE) were put on the sides of the TPC as shown in Fig. 2.14, and the remaining four were (TPC-FWD) placed between the TPC and the LEPS spectrometer, see Fig. 2.23. The length and thickness of the TPC-SIDE counters (a∼f in Fig. 2.14) are 880 mm and 1/4 inches, respectively, and the width is 285 mm, 270 mm, 285 mm, 240 mm, 270 mm, 270 mm for the counter a, b, c, d, e, f, respectively. The thickness of the TPC-FWD counters is 1/4 inches for the trapezoidal one and 5 mm for the rectangular one. The trapezoidal counters are viewed by two PMT's. The size of the TPC-FWD counters are indicated in Fig. 2.23.
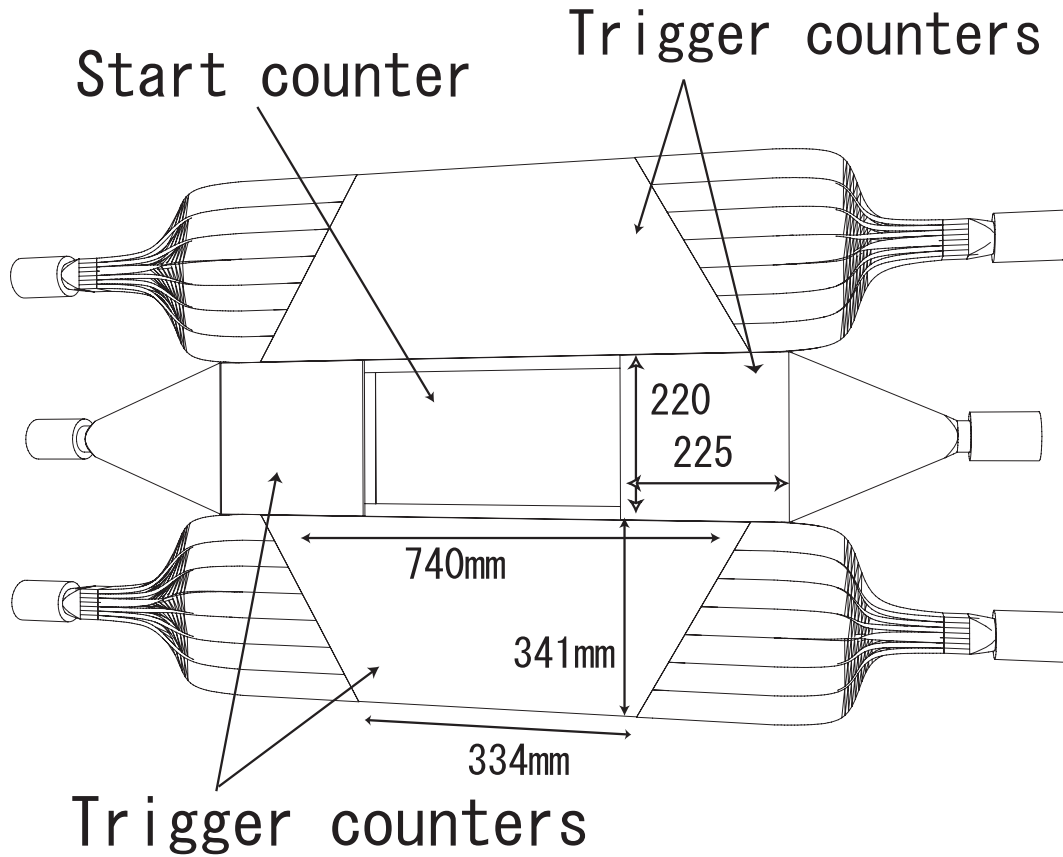
Figure 2.23: Schematic drawing of forward trigger counters for TPC.

## 2.4.4 Solenoid magnet

A superconducting solenoid magnet was used to momentum-analyze the charged particles detected by the TPC. The magnitude of the magnetic field was 2 Tesla at the center of the magnet. The solenoid magnet has an aperture of 300 mm in radius. The center of the magnet was placed at -1510 mm along the beam axis from the center of the dipole magnet. The center of the target was at -1527 mm, which is slightly upstream from the center of the solenoid magnet. The magnetic field was measured with a hole probe and the measured distribution was compared with the result obtained by the RADIA simulation. The distribution of the magnetic field obtained by RADIA was used in the tracking. Fig. 2.24 shows the distribution of the magnetic field $B_z$ calculated by the RADIA as a function of the z-coordinate at x=0 and y=0. The sum of magnetic field of the solenoid and dipole magnet is shown.
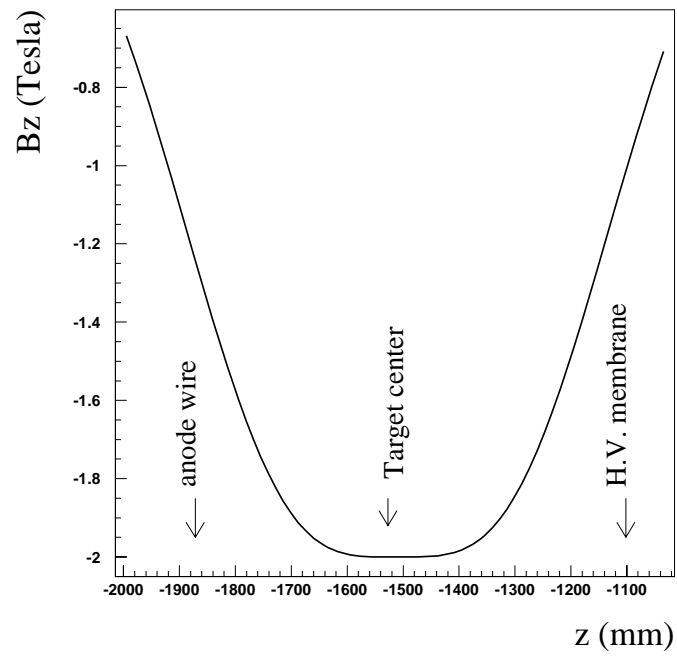
Figure 2.24: The z-component of the magnetic field at $x = y = 0$ mm in the solenoid magnet.

## 2.5   Electronics and Triggers

### 2.5.1   Readout electronics for the LEPS spectrometer

The analog-to-digital converter (ADC) modules and the time-to-digital converter (TDC) modules used to read the signals from the detectors of the LEPS spectrometer are summarized in Table 2.4.

Table 2.4: Readout modules (digitizers) for detectors

| Detector | ADC | TDC | abbrev. |
|----------|------|---------------------|------------|
| TAG | FERA | FASTBUS 1875A | TAG |
| UPveto | FERA | FASTBUS 1875A | UPveto |
| SC | FERA | FASTBUS 1875A | SC |
| AC | FERA | FASTBUS 1875A | AC |
| DC's | - | FASTBUS 1877S | - |
| TOF | FERA | FASTBUS 1875A | TOF (M$\geq$1) |
| RF | - | FASTBUS 1875A/1877S | - |

The signals from the tagging system, the upstream-veto counter, the SC, the AC counter, the TOF counters and the TPC-SIDE and TPC-FWD counters were digitized by the LeCroy 4300B FERA (Fast Encoding & Readout ADC) modules and LeCroy FASTBUS 1875A TDC modules. LeCroy FASTBUS 1877S TDC modules were used to digitized the drift time of electrons in the DC1, DC2 and DC3.

### 2.5.2   Readout electronics for the TPC

Signals from the TPC were amplified by charge-sensitive preamplifiers and shaping amplifiers. The preamplifier has the integration time of 132 nsec and the gain of 2.5 V/pC. The shaping amplifier is the CR-$(RC)^4$ type band-pass filter with the shaping time of 20 nsec. The FWHM of the output signal from the shaping amplifier was typically 200 nsec. The signal to noise ratio of the readout electronics affects on the measurement of the coordinate in the pad plane using the center-of-gravity of the charge induced on pads. In order to achieve the resolution of 350 $\mu$m in pad row direction for minimum-ionizing particles (MIPs), the noise level must be less than 1% of the signal height. The waveform of signals was digitized by the flash analog-to-digital converter (FADC) module of 10 bit resolution and 40 MHz sampling rate. The FADC modules were installed in the 9U-VME crate, and the data are read through the VME bus-line. The baseline and the RMS noise were measured every five hours using data taken by the clock trigger. The RMS of the noise on a pad was found to be $\sigma \sim 0.8$ ADC channel. The gain of the anode wire was adjusted to set the signal height from MIPs to be 100 ADC channel, and thus, the required noise level of 1% was satisfied. In order to reduce the data size, the zero-suppression

for the data at the threshold of 3 $\sigma$ of RMS noise was applied on FADC board. In addition, the noise which has the width of less than 4 time bins (100 nsec) were rejected before storing into the FIFO memory on the FADC module to reduce the data size.

### 2.5.3   Trigger

The trigger signal was made using the signals from the tagging system (TAG), upstream-veto counter (UP), aerogel Čerenkov counter (AC), TOF counters, TPC-SIDE counters and TPC-FWD counters. The trigger signals for each detector subsystem is described below, and the logic diagram is shown in Fig. 2.25.

**TAG** In the tagging system, OR signals from the scintillation fibers are mode in each layer (TAG-SFF and TAG-SFB) and TAG-PL hodoscope. Then the AND signal of them were used in the trigger logic.

**UP** The logic signal from the upstream-veto counter was used as a veto signal. The width of the veto signal was set to be 75 nsec.

**SC** The coincidence signal from both PMT's of the SC was used in the trigger logic. The coincidence signal supplies the common start and stop in the TDC modules. The width of the coincidence signal was set 25 nsec.

**AC** The OR signal from four PMT's of the AC was used to make a veto signal for a trigger logic. The width of the veto signal was set 75 nsec.

**TOF** In the TOF system, the mean timing of the logic signals from the two PMT's of a TOF counter was made by a mean timer module (CAMAC C561). The signal from the mean timer module was read by the majority logic unit module 4532 (CAMAC). The signals of the multiplicity $\geq 1$ or $\geq 2$ were used in the trigger logic.

**TPC-SIDE, TPC-FWD** All of counters except for two trapezoidal counters of TPC-FWD were viewed by one PMT, and the logic signal was used for the trigger. The trapezoidal counters of TPC-FWD were viewed by two PMT's, and the mean timing of the the signals were used for the trigger logic. The logic signal from the trigger counters for the TPC was read by the majority logic unit module.

**Tagging counter (TAG)**

TAG-PL

fiber (SFF) (#1–#55)

fiber (SFB) (#1–#55)

TAG

Tag * $\overline{\text{Up}}$

**Up veto counter (UP)**

PMT

**Start Counter (SC)**

PMT left

PMT right

mean timer

SC

**TOF counters (TOF)**

TOF1 (top)

TOF1 (bottom)

mean timer

#1

TOF#2-40

majority

Multiplicity ≧ 1    TOF **or**

Multiplicity ≧ 2    TOF≧2

**Aerogel counter (AC)**

PMT 1

PMT 2

PMT 3

PMT 4

or

AC

**TPC-SIDE counter**

Side #1-6

**TPC-FWD counter**

trapezoid up PMT1

trapezoid up PMT2

mean timer

trapezoid down PMT1

trapezoid down PMT2

mean timer

rectangle 1

rectangle 2

Figure 2.25: Diagram of the readout circuits for triggers.

The particles scattered to forward angles and passed through the LEPS spectrometer were identified by the coincidence of SC and TOF counters. The $e^+e^-$ pair creation events were vetoed by the AC counter. Three trigger conditions were used for the data taking: (a) the trigger for events in which at least three counters have signal, (b) the trigger for events in which at least two counters have signal and (c) the trigger for events with two charged particles in the LEPS spectrometer and at least one particle hitting the TPC-SIDE counter. The trigger logic can be written as

$$
\begin{aligned}
\text{Trigger(a)} &= \text{TAG} \otimes \overline{\text{UP}} \otimes \overline{\text{AC}} \otimes (\text{TPC-SIDE} + \text{TPC-FWD} + \text{SC} \otimes \text{TOF}) \geq 3 \\
\text{Trigger(b)} &= \text{TAG} \otimes \overline{\text{UP}} \otimes \overline{\text{AC}} \otimes (\text{TPC-SIDE} + \text{TPC-FWD} + \text{SC} \otimes \text{TOF}) \geq 2 \\
\text{Trigger(c)} &= \text{TAG} \otimes \overline{\text{UP}} \otimes \overline{\text{AC}} \otimes (\text{TPC-SIDE} \geq 1) \otimes \text{SC} \otimes (\text{TOF} \geq 2),
\end{aligned}
$$

where "$\otimes$" represents the AND logic, and the "$+$" represents the OR logic. The logic diagram is shown in Fig. 2.26. Typical trigger rates with the $CH_2$ and carbon target were 55 cps for the trigger (a), 120 cps for the trigger (b) and 1.8 cps for the trigger (c) for 710 kcps of tagged photons. Because the rate of the trigger (b) was too high to read out the data of the TPC, the trigger (b) was scaled down by a factor of 2~3. In the study of $\Lambda(1405)$ production by $\gamma p \to K^+ \Lambda(1405) \to K^+ \Sigma^\pm \pi^\mp \to K^+ \pi^+ \pi^-$ reaction, three charged particles are produced in the final state. Thus, the trigger (a) was used as the main trigger for the data taking. For the analysis of the $\Lambda(1405)$ and $\Sigma^0(1385)$ photoproduction, the data taken with the trigger (a) was used.

**Trigger (a)**   Tag*$\overline{\text{Up}}$*$\overline{\text{AC}}$*(SC*TOFor+TPC)$\geqq$ 3
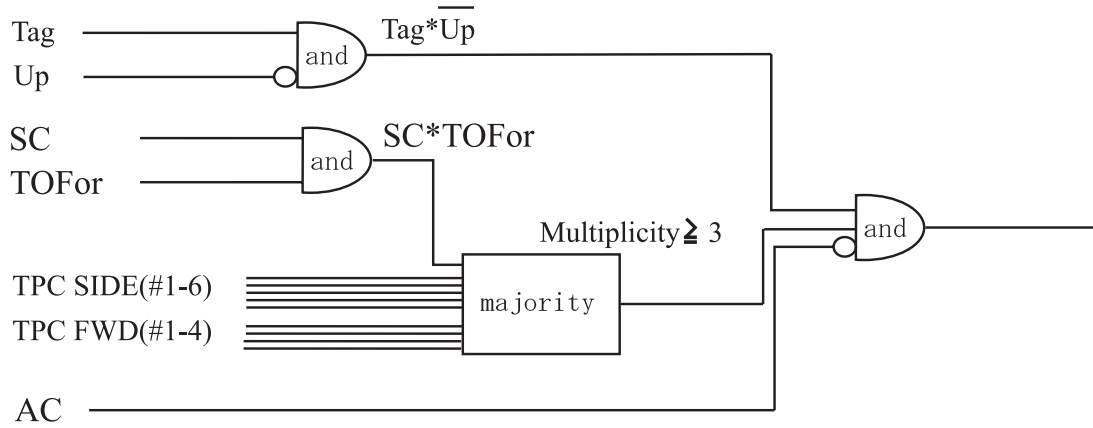


**Trigger (b)**   Tag*$\overline{\text{Up}}$*$\overline{\text{AC}}$*(SC*TOFor+TPC)$\geqq$ 2
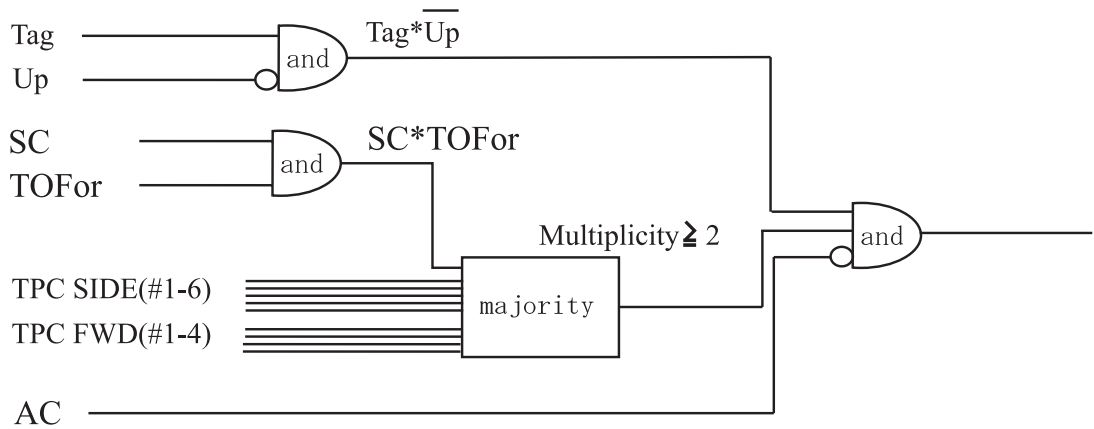


**Trigger (c)**   Tag*$\overline{\text{Up}}$*$\overline{\text{AC}}$*SC*(TPC-SIDE or)*(TOF$\geqq$ 2)
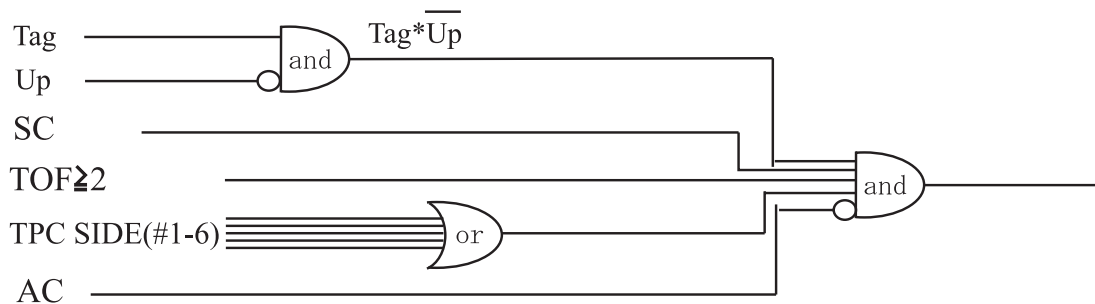


Figure 2.26: Diagram of the readout circuits for triggers.

## 2.6   Data acquisition system (DAQ)

There were three local DAQ systems. The first one handles the pulse-height of signals from the TAG-PL, the UPveto, the SC, the AC, TOF counters, TPC-SIDE and TPC-FWD counters. The digitized data from the FERA modules were collected by the universal I/O module (UIO) which is a VME module with an 8-MB memory through the FERA divider. The UIO module is designed as a buffer sequencer which is used for data readout and buffering. The buffer data are transferred from the UIO to a VME CPU-board. The CPU sends the data to the data builder.

The second system handles the timing information from the TAG-PL, the UP-veto, the SC, the AC, TOF counters, TPC-SIDE and TPC-FWD counters, and the drift time information from the DC's. The Next-Generation FASTBUS (NGF) was used as a buffer sequencer module and a FASTBUS-VME interface. The NGF has a sequencer and memory to readout and store the data from the TDC modules. The NGF has a VME bus in which a CPU and a interrupt register was installed. The CPU reads data from the NGF memory and sends it to the data builder when the buffer-change request come to the interrupt register.

The third system handles the signals from the TPC. The waveform of the signals was digitized by the FADC and stored to the FIFO memories on the FADC board for four events. The data were read by the on-board CPU through the VME bus and sent to the data builder when the buffer-change request comes to the interrupt register. The typical data size was 50 kbyte/events. The data transfer time through the VME bus was the major part of the busy time of DAQ. The dead time of the DAQ in the experiment was 30% under the condition with the trigger rate of 70 Hz.

## 2.7   Data summary

The experiment for the data set (II) was carried out in the year 2004. The total beam time used for this study was about 100 days. The data for the $CH_2$ and carbon targets were used for the study of $\Lambda(1405)$ and $\Sigma^0(1385)$ production. The numbers of tagged photon were about $9 \times 10^{11}$ for $CH_2$, and $5 \times 10^{11}$ for carbon. About half of data were collected with vertically polarized photons and the remaining half were taken with horizontally polarized photons.

# Chapter 3

# Production ratio of $\Lambda(1405)$ to $\Sigma^0(1385)$

The procedure of the analysis for the measurement of the production ratio of $\Lambda(1405)$ to $\Sigma^0(1385)$ is described in this chapter. First of all, $K^+$'s produced from the $\gamma p \to K^+ X$ reaction were identified from the mass reconstructed by the LEPS spectrometer. Then, the decay products of these hyperon resonances were detected by the TPC. The production ratio between $\Sigma^0(1385)$ and $\Lambda(1405)$ was obtained from the yields of $\Sigma^0(1385)$ and $\Lambda(1405)$ measured from their $\Lambda\pi^0$ and $\Sigma^\pm\pi^\mp$ decay modes, respectively.

## 3.1   Event selection by the LEPS spectrometer

For the analysis of $\Lambda(1405)$ and $\Sigma^0(1385)$ production, $K^+$'s produced from the $\gamma p \to K^+ X$ reaction were identified by the LEPS spectrometer. Event selection criteria for $K^+$ photoproduction by the LEPS spectrometer were (1) $K^+$ selection by the reconstructed mass, (2) rejection of decay-in-flight of $K^+$'s, (3) vertex selection at the target and (4) reconstruction of one recoiled electron in the tagging counter. The numbers of events after these cuts are summarized in Table 3.1.

Table 3.1: Cut summary of $K^+$ selection by the LEPS spectrometer.

| Selection cuts | number of events (CH$_2$) | number of events (C) |
|---|---|---|
| $K^+$ selection | $1.39 \times 10^5$ | $7.38 \times 10^4$ |
| $K^+$ decay-in-flight rejection | $1.30 \times 10^5$ | $6.88 \times 10^4$ |
| Vertex selection at the target | $1.26 \times 10^5$ | $6.68 \times 10^4$ |
| One recoil electron in the tagging counter | $1.12 \times 10^5$ | $5.92 \times 10^4$ |

### 3.1.1   Identification of $K^+$'s by the LEPS spectrometer

The momentum of a track was reconstructed from the hit coordinates in three drift chambers. The trajectory of the particle was reconstructed by solving the equation of motion of a particle in the magnetic field using Runge-Kutta integration. In addition, the Kalman filtering method was applied to take into account of the effect of multiple scattering in the spectrometer and the decay-in-flight of a pion or a $K^+$. Figure 3.1 shows distributions of $\chi^2$ probability for track fitting. If the $\chi^2$ probability is less than 0.02, the hit with the largest $\chi^2$ value is removed from the track as an outlier and the track fitting is applied again. This procedure is repeated until the $prob(\chi^2)$ become larger than 0.02 or the number of outliers become larger than 6. The cut condition of $prob(\chi^2) > 0.02$ was required to reject $K^+$ decay events.
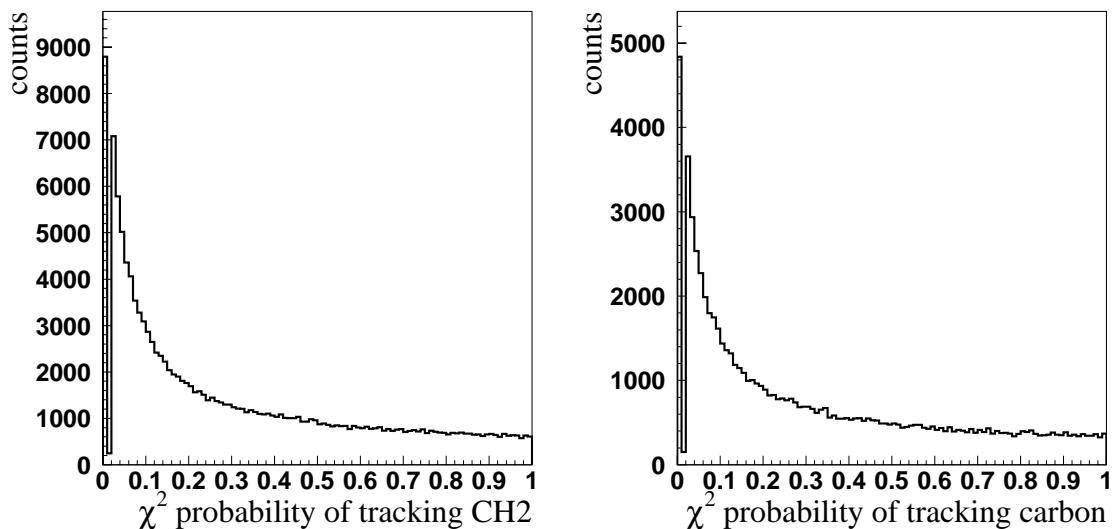


Figure 3.1: Distribution of $\chi^2$ probability of track reconstruction for $K^+$'s from the CH$_2$ target (left) and the carbon target (right).

The mass of each charged particle was reconstructed using the momentum and velocity measured from the path length of the particle trajectory and the time-of-flight from the target to the TOF counters, where the start time was determined using the RF signal of the electron storage ring. Figure 3.2 shows correlation plots between the momentum and reconstructed mass of particles produced from the $CH_2$ target (left) and the carbon target (right).
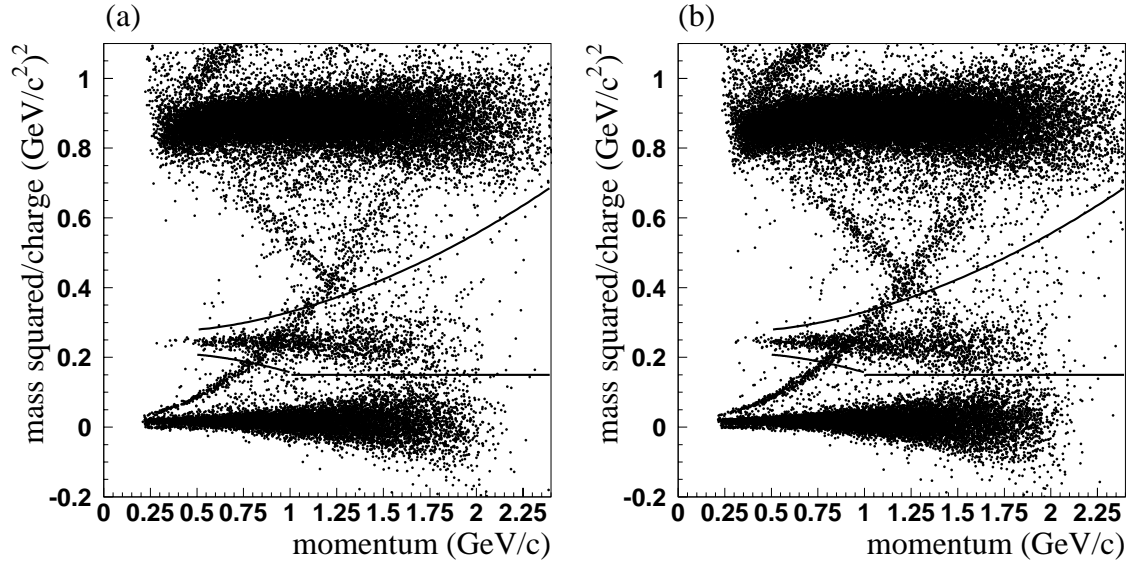


Figure 3.2: Correlation plots between the momentum and reconstructed mass of particles produced from the $CH_2$ target (left) and the carbon target (right). The solid lines indicate boundaries for the $K^+$ selection.

For the selection of $K^+$'s, $4\,\sigma$ cut was used with momentum dependent mass resolution. The mass resolution is described as

$$\sigma_{M^2}^2 = 4M^4\left(\frac{a_1^2}{\beta^2} + p^2 a_2^2\right) + 4p^2(p^2 + M^2)\left(\frac{c}{L}a_3\right)^2,$$

where $M$ is the mass of the kaon, $c$ is the speed of light and $L$ is the typical path length (4100 mm). The first and second terms represent the effect of the multiple scattering and the spatial resolutions of the drift chambers, respectively. The third term represents the effect of the resolution of the time-of-flight measurement. The boundary between pions and kaons was set to 0.1 $(GeV/c^2)^2$ where the $4\sigma$ boundaries overlap each other. The parameters, $a_1$, $a_2$ and $a_3$, were obtained by fitting to be 0.0087, 0.0042 and 0.13 respectively. The momentum resolution can be written as $(\sigma_p/p)^2 = (a_1/\beta)^2 + p^2 a_2^2$.

Since the time resolution of the start counter was not sufficient to separate 2 nsec interval of the RF signal, the RF bucket adjacent to the correct one corresponding

to the Compton scattering was selected. In such events, the masses of particles were not correctly obtained, and $e^+$'s, $\pi^+$'s and protons were contaminated into the $K^+$ selection region. The contamination due to particle misidentification was estimated in the analysis for each reaction.

### 3.1.2 Event selection by reaction vertices

The reaction vertex between a photon and a $K^+$ was defined as the closest point between the beam axis (z-axis) and a reconstructed $K^+$ track. Figure 3.3 shows the distribution of z coordinate of reaction vertices (vtz) for the CH$_2$ target (left) and the carbon target (right). A peak around vtz = -1520 mm corresponds to the z coordinate of the target. The distributions of reaction vertices were much wider than the real size of the target, 47 mm for the CH$_2$ and 22 mm for the carbon, because angles between the beam axis and $K^+$'s were small and the resolution for vtz was not good. The loose cut boundaries were applied for vtz as follows, $-1656\,\text{mm} < \text{vtz} < -1386\,\text{mm}$.
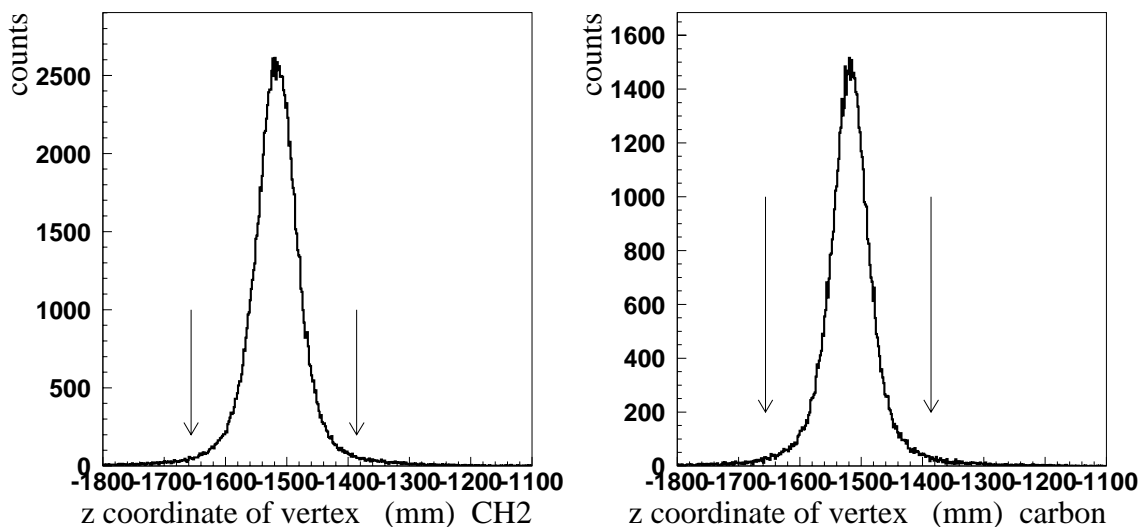


Figure 3.3: The distribution of z coordinate of closest point of a $K^+$ trajectory with the beam axis (vtz) for the CH$_2$ target (left) and for the carbon target (right). Cut boundaries are shown by the arrows.

### 3.1.3 Event selection by the number of tracks in the tagging counter

The energy of incident photons was obtained from the momentum of a recoiled electron detected by the tagging counter. There were events in which the reconstruction of a track was failed although a signal of the tagging counter was required in the trigger condition. Figure 3.4 shows distributions of the number of tracks in the tagging counter for the $CH_2$ target (left) and the carbon target (right). We selected events where one track was found in the tagging counter.
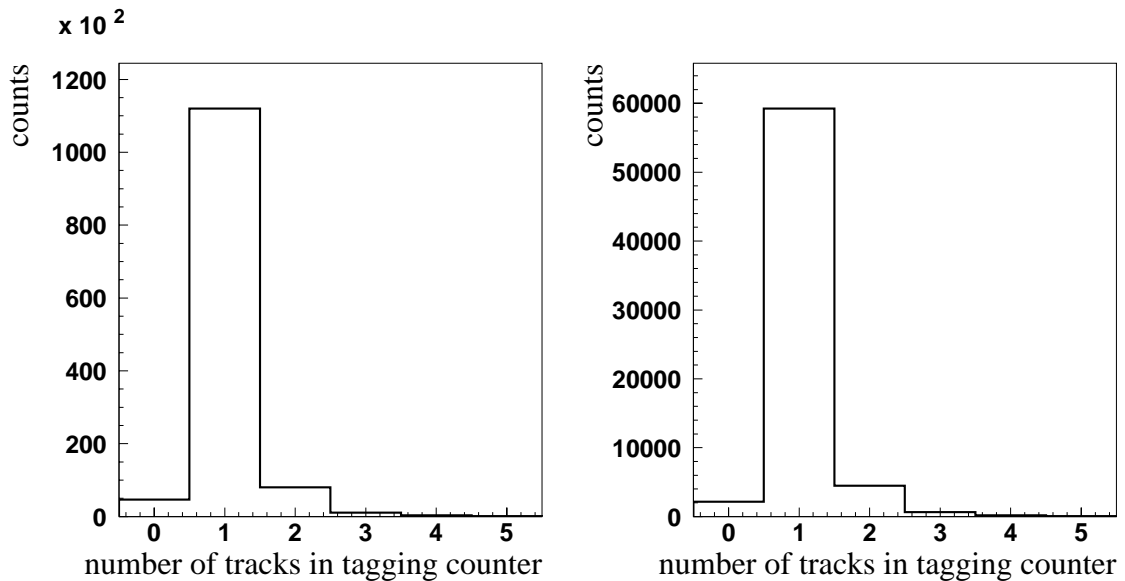


Figure 3.4: Distribution of the number of tracks in the tagging counter for the $CH_2$ target (left) and for the carbon target (right).

### 3.1.4   The missing mass distribution of $\gamma p \to K^+ X$ reaction

Figure 3.5 shows missing mass of the $\gamma p \to K^+ X$ reaction ($MM(K^+)$). Plot (a) shows spectra for the $CH_2$ target (solid) and for the carbon target (dashed). The spectrum from free protons in $CH_2$ was extracted by subtracting the spectrum for carbon from the one for $CH_2$ after proper normalization by the number of photons and number of carbon nuclei in the target. Plot (b) shows a spectrum for free protons in the $CH_2$ target.
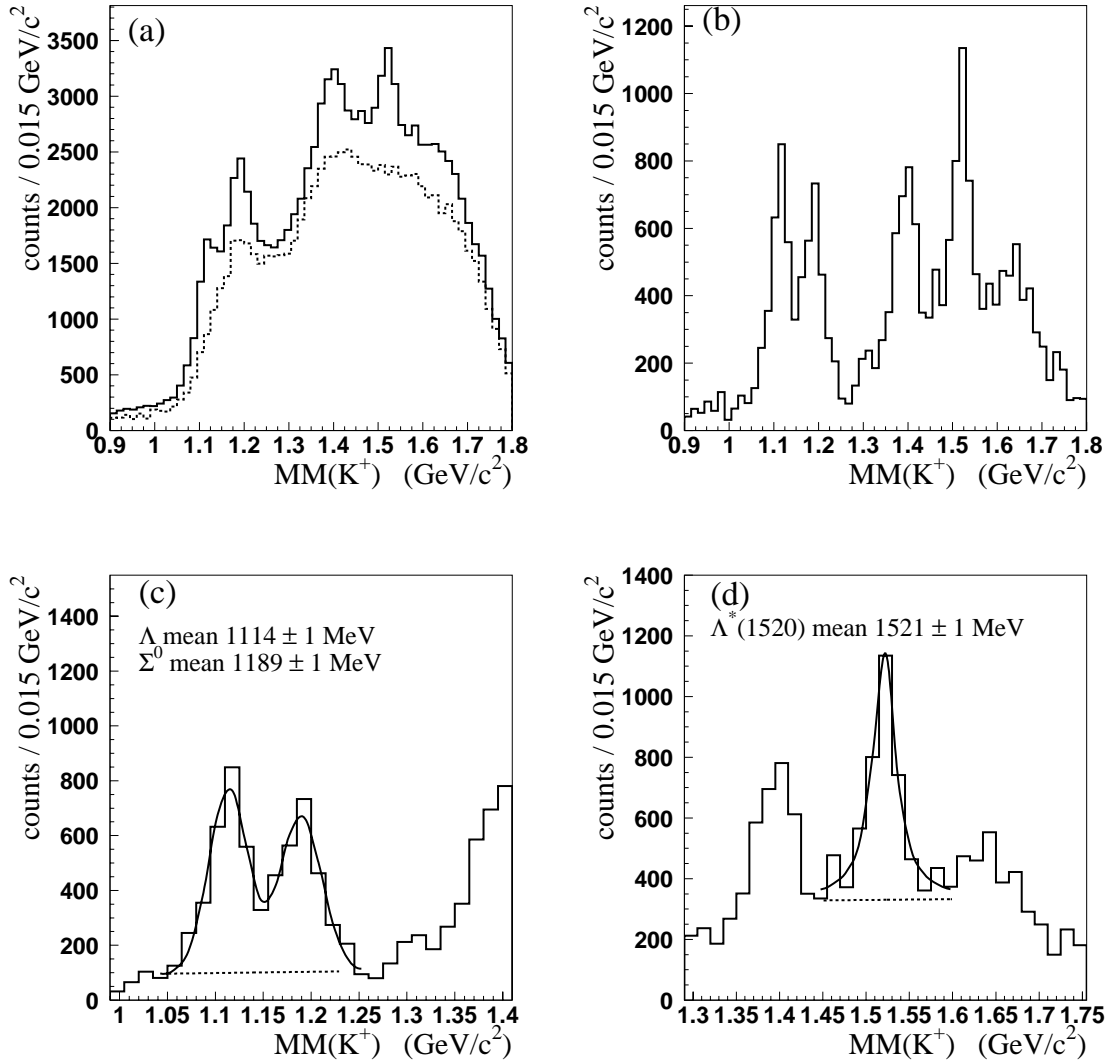


Figure 3.5: Distribution of $MM(K^+)$. (a) shows a spectrum for the $CH_2$ target (solid) and the one for the carbon target (dashed). (b), (c) and (d) show a spectrum for free protons in the $CH_2$ target. (c) and (d) show spectra around $\Lambda(1116)$ region and $\Lambda(1520)$ region, respectively.

Plot (c) and (d) show spectra for free protons around $\Lambda(1116)$ and $\Lambda(1520)$ mass region, respectively. The mass peak positions of $\Lambda(1116)$ and $\Sigma^+(1192)$ were obtained from Gaussian fit to the data with a linear background assumption to be $1114 \pm 1$ MeV/c$^2$ and $1189 \pm 1$ MeV/c$^2$. The mass peak position of $\Lambda(1520)$ was measured from Breit-Wigner fit with a linear background to be $1521 \pm 1$ MeV/c$^2$. The measured masses of these hyperons are consistent with the world average values (PDG values) [1].

### 3.1.5   Acceptance of $K^+$'s in the LEPS spectrometer

In order to match the acceptance of $K^+$'s in the data set (II) to that of the data set (I), a cut was applied in the polar angle distribution of $K^+$'s in the center of mass frame. Fig. 3.6 (left) shows distributions of polar angles of $K^+$'s ($\Theta_{K_{CM}}$) in the center-of-mass frame for events in the region of $1.3 < MM(K^+) < 1.45$ GeV/c$^2$. The solid (dashed) histogram shows distribution for the CH$_2$ (carbon) target. Fig. 3.6 (right) shows the same distribution obtained by a Monte Carlo simulation. Events with $\cos(\Theta_{K_{CM}}) > 0.8$ were selected for the analysis. The arrows indicate the cut point. The acceptance for this cut was about 80% for both CH$_2$ and carbon.
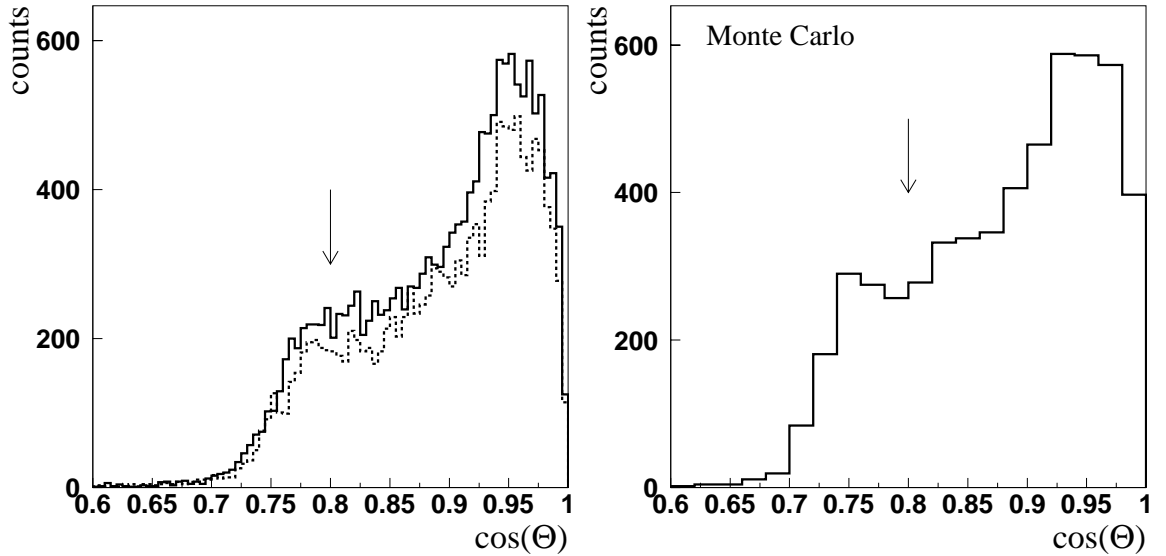


Figure 3.6: Distributions of polar angles of $K^+$'s in the center of mass frame. Left: Solid histogram is for the CH$_2$ target and dashed one is for the carbon target. Right: Monte Carlo simulation. The arrows indicate the cut point.

## 3.2    Reconstruction of tracks in TPC

The momentum and the energy deposition of particles detected by the TPC were obtained using signals from cathode pads. First of all, the peak of the waveform of a signal was searched and the height and time information at the peak of the signal were obtained. Protons with small momenta give large energy deposition, and the height of the signals sometimes extends beyond the dynamic range of the FADC module. The height of such a saturated signal was estimated by fitting the Gaussian convoluted exponential function to the waveform. The histogram in Fig. 3.7 (left) shows the waveform of a saturated signal, and the dashed line shows the fit result. The height and timing information at the peak was obtained from the fitted function. If the signal has more than one peak structure, the signal is divided at the minimum between peaks and split into the several sequences. Fig. 3.7 (right) shows an example of a signal which has two peaks. The signal was divided into two at the drift time indicated by the line.
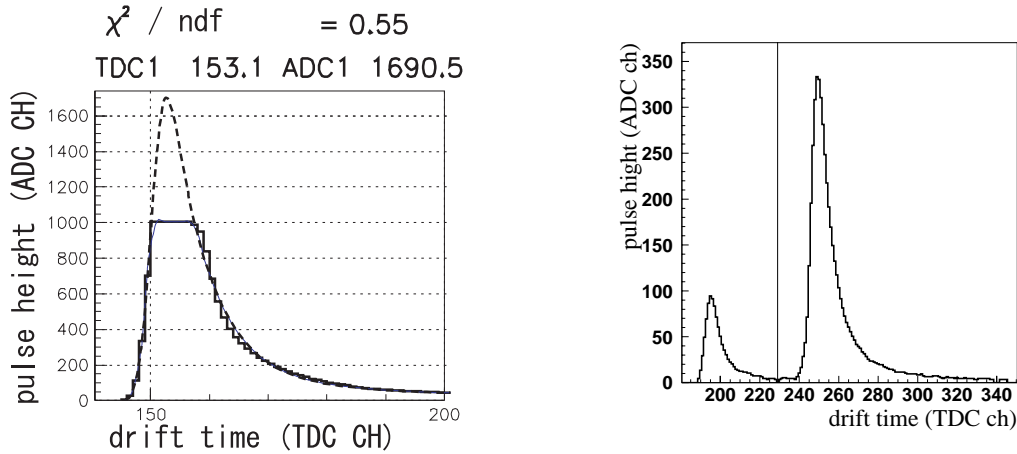


Figure 3.7: (left): Waveform of a saturated signal. The dashed line shows the fit result. (right) : An example of a signal which has two peaks. The signal was divided into two at the drift time indicated by the line.

Secondly, a cluster of the signals which corresponds to an avalanche was searched in each layer. If a signal overlaps the other signals on adjacent pads in the time spectra, these signals are registered to a cluster. The hit coordinates were obtained in the cylindrical coordinate, $r, \phi, z$, where the $z$-axis is parallel to the beam direction. The radial coordinate ($r$) was obtained from the center of the pad layer. The coordinate along the pad row ($\phi$) was obtained from the center-of-gravity of the induced charges, where typically three pads have induced charges from an avalanche, and a Gaussian charge distribution was assumed. The drift time was obtained from the time information at the one fifth of the highest signal in the cluster. Then, the coordinate along the drift direction ($z$) was obtained by solving the equation of mo-

tion of electrons in the gas with the electric and magnetic field using the drift time. Details of the measurement of the $z$ coordinate is described in Appendix A.

Thirdly, a track was reconstructed from the coordinates of the clusters on all layers. The algorithm of the track finding is as follows: (1) to select the clusters on the most outer three layers, (2) to reconstruct a helix from the coordinates of the selected clusters, (3) to search a cluster which associates with the helix in the next inner layer, and to register the cluster to the track candidate if it is close to the helix within 3 mm in pad row direction and 6 mm in z direction, (4) to obtain the helix parameters using all of the clusters registered to the track candidate. The procedures (3) and (4) were repeated until all layers are searched. If the number of clusters associated with the track candidate is less than 5, the track candidate is discarded.

In order to reconstruct trajectories of charged particles in the TPC, each track was required to reach at least the 7th pad layer. Fig. 3.8 shows a correlation plot between the momentum and scattering angle of particles reconstructed by the TPC for the events where a $K^+$ was detected in the LEPS spectrometer. The left top plot shows the distribution for positively charged particles which reached at least the 7th layer. The left bottom one shows the same distribution for positively charged particles which did not reach the 7th layer. The right two plots are same distributions for negatively charged particles. Particles with small polar angles or small momenta which did not reach the 7th layer of the TPC were rejected by these criteria.
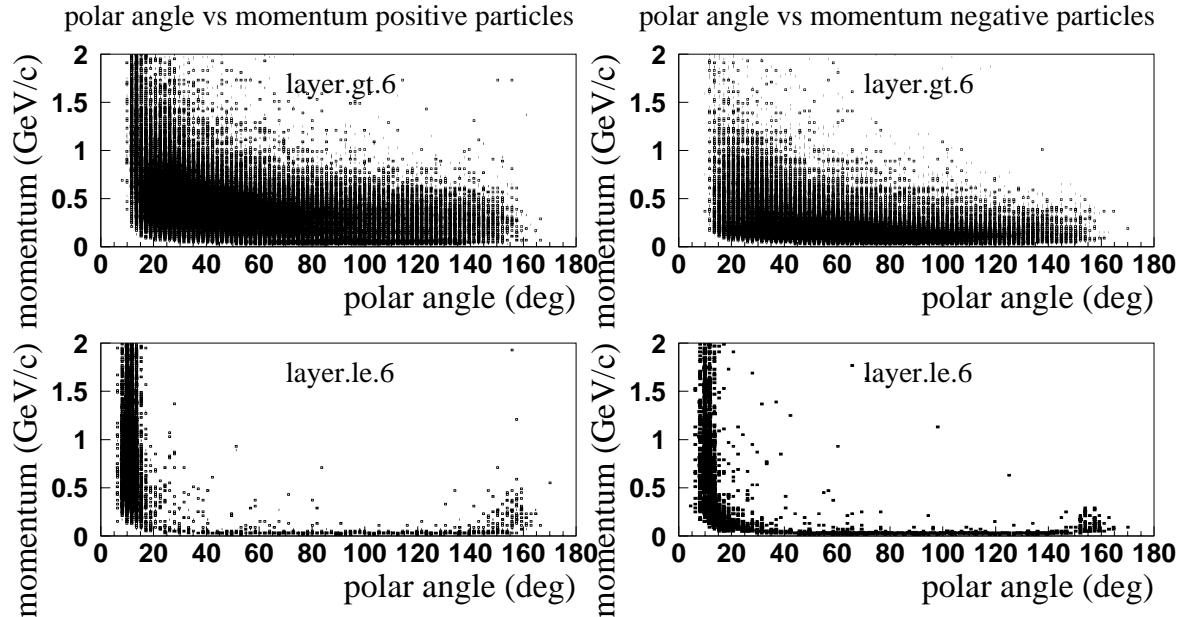


Figure 3.8: Correlation plots of momentum and scattering angle for positively (left) and negatively (right) charged particles for the events where a $K^+$ was detected at the LEPS spectrometer. The cut conditions were written in each plot.

The momentum of a detected particle was obtained by solving the equation of motion in the nonuniform magnetic field with the Runge-Kutta integration. If the $\chi^2$ probability ($prob(\chi^2)$) for the track fitting is less than 0.02, the hit with the largest $\chi^2$ value is removed, and the track fitting is applied again. This procedure was repeated until the $prob(\chi^2)$ become larger than 0.02, or the number of hits associated with the track becomes less than 6. Fig. 3.9 shows $\chi^2$ probability distributions for the track fitting. In order to reject noise, tracks with $prob(\chi^2) > 0.02$ were selected.
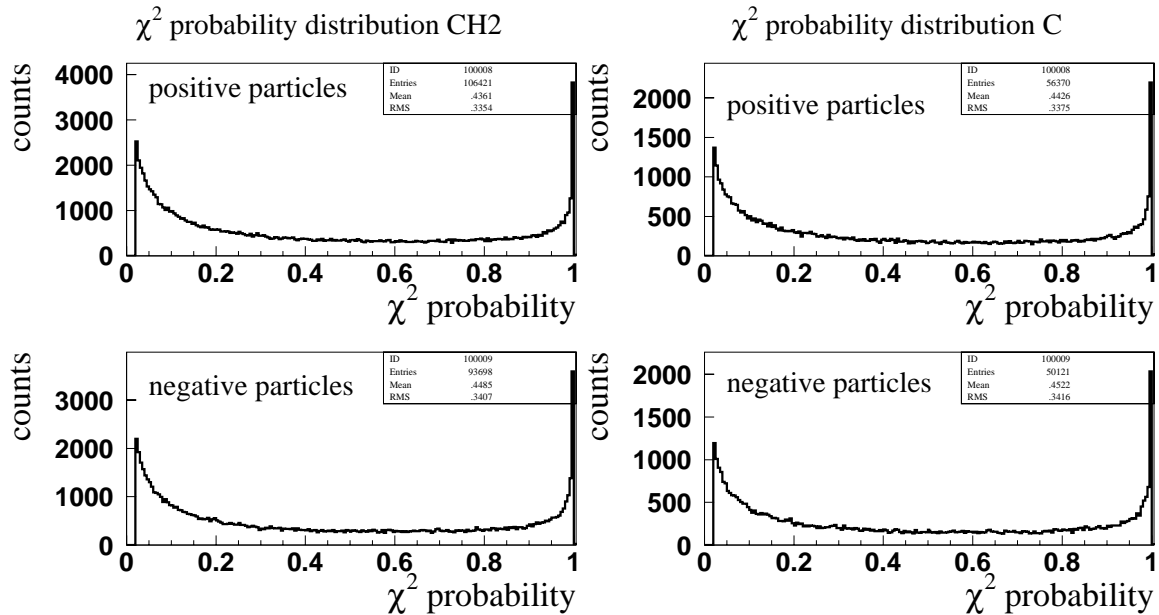


Figure 3.9: $\chi^2$ probability distributions of the track reconstruction for the CH$_2$ target (left) and the carbon target (right).

## 3.2.1  Particle identification by the TPC

Protons and charged pions were identified by the truncated mean of the energy de-
position ($dE/dx$) of the particle on the all hit layers. The threshold of the truncation
was set to about 60% of the largest signal to minimize the RMS of the $dE/dx$ distri-
bution. The energy deposition on the truncated layers measured along the track was
used to calculate the $dE/dx$. Correlation plots between the $dE/dx$ and momentum
of a reconstructed track in the TPC are shown in Fig. 3.10.
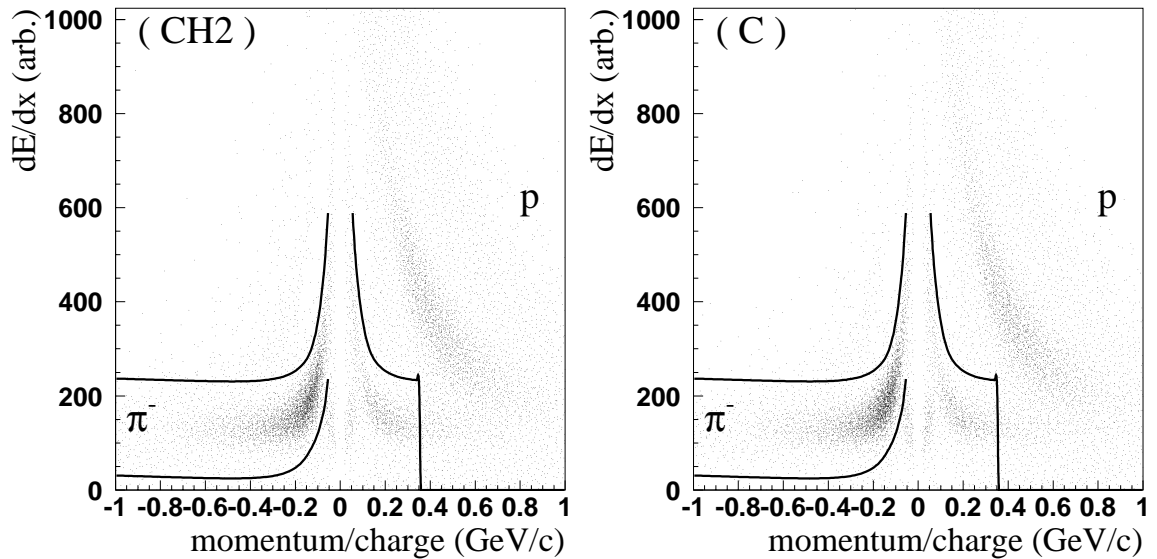


Figure 3.10: Correlation between the $dE/dx$ and momentum of tracks reconstructed
by TPC for the events where a $K^+$ was detected in the LEPS spectrometer for $CH_2$
(left) and for carbon (right).

The solid lines show cut boundaries for the $\pi^-$ selection and the proton selec-
tion. The $\pi^-$'s were selected by 3 $\sigma$ of the RMS of the $dE/dx$ distribution. A
positively charged particle with larger $dE/dx$ than 3 $\sigma$ boundary for $\pi^+$ selection
was identified as a proton. The proton/$\pi^+$ separation capability becomes worse for
higher momentum region because the energy deposition by a proton become small.
In order to select these high momentum proton, a positive particle with the momen-
tum of more than 0.35 GeV/c was identified as a proton. For the $\pi^+$ selection, the
same cut boundaries as for the $\pi^-$ selection were used. More details on the particle
identification by the TPC are described in Appendix C.

## 3.3   Photoproduction of $\Sigma^0(1385)$

In this section, the analysis for the measurement of $\Sigma^0(1385)$ photoproduction using $\Lambda\pi^0$ decay mode is described. The reaction studied by this analysis is as follows,

$$
\begin{aligned}
\gamma\, p \quad &\rightarrow \quad K^+ \; \Sigma^0(1385) \\
&\rightarrow \quad K^+ \; \Lambda \; \pi^0 \\
&\rightarrow \quad K^+ \; p \; \pi^- \; \pi^0 \; .
\end{aligned}
$$

The $K^+\Sigma^0(1385)$ production events were identified from a peak in the missing mass of the $\gamma p \rightarrow K^+X$ reaction ($MM(K^+)$) for $(K^+\Lambda\pi^0)$ final state, because $\Lambda(1405)$ is prohibited from decaying into $\Lambda\pi^0$ by isospin conservation. For this analysis, the $\Lambda$ hyperon was detected from the invariant mass of $(p\,\pi^-)$ pairs, and the $\pi^0$'s were identified through the missing mass technique. We selected events in which a $K^+$ was detected in the LEPS spectrometer and a proton and $\pi^-$ in TPC. Since there was no photon-sensitive detector in this experiment, the $\pi^0$ was identified from the missing mass of $\gamma p \rightarrow K^+ p\pi^-X$ reaction. The main background reactions were $\Sigma^0\,\pi^0$ decay of $\Lambda(1405)$ and $\Sigma^+\,\pi^-$ decay of $\Lambda(1405)$ and $\Sigma^0(1385)$ , namely,

$$
\begin{aligned}
\gamma\, p \quad &\rightarrow \quad K^+ \; \Lambda(1405) \\
&\rightarrow \quad K^+ \; \Sigma^0 \; \pi^0 \\
&\rightarrow \quad K^+ \; \Lambda\,\gamma \; \pi^0 \\
&\rightarrow \quad K^+ \; p \; \pi^- \; \gamma \; \pi^0
\end{aligned}
\tag{3.1}
$$

and

$$
\begin{aligned}
\gamma\, p \quad &\rightarrow \quad K^+ \; \Lambda(1405)/\Sigma(1385) \\
&\rightarrow \quad K^+ \; \Sigma^+ \; \pi^- \\
&\rightarrow \quad K^+ \; p \; \pi^0\,\pi^- \; .
\end{aligned}
\tag{3.2}
$$

The contamination of the reaction (3.1) was estimated from the missing mass of the $\gamma p \rightarrow K^+ p\pi^- X$ reaction, where $X = \pi^0$ for $\Sigma^0(1385)$ production, and $X = \pi^0\gamma$ for the background of the reaction (3.1). On the other hand, the contamination of the reaction (3.2) was estimated from missing mass of the $\gamma p \rightarrow K^+\pi^- X$ reaction, where $X = p\,\pi^0$ for the $\Sigma^0(1385)$ production, and $X = \Sigma^+$ for the background of the reaction (3.2)

The outline of the analysis is as follows, (1) selection of a $K^+$ in the LEPS spectrometer, (2) selection of a $(p\pi^-)$ pair in the TPC, (3) identification of a $\Lambda$ from invariant mass of $(p\pi^-)$ pair, (4) estimation of the contamination from $\Sigma^0\pi^0$ decay of $\Lambda(1405)$ , (5) estimation of the contamination from $\Sigma^+\pi^-$ decay of $\Lambda(1405)$ , and (6) extraction of the yield of $\Sigma^0(1385)$ photoproduction from $MM(K^+)$ for the $\Lambda$ tagged events after subtracting the contamination of the reaction (3.1) and (3.2).

## 3.3.1   Identification of Λ's by TPC

The invariant mass spectra of $(p\pi^-)$ pairs $(M(p\pi^-))$ for $CH_2$ and carbon are shown in Fig. 3.11 (left) and (right), respectively. The peaks corresponding to the mass of Λ are clearly observed.
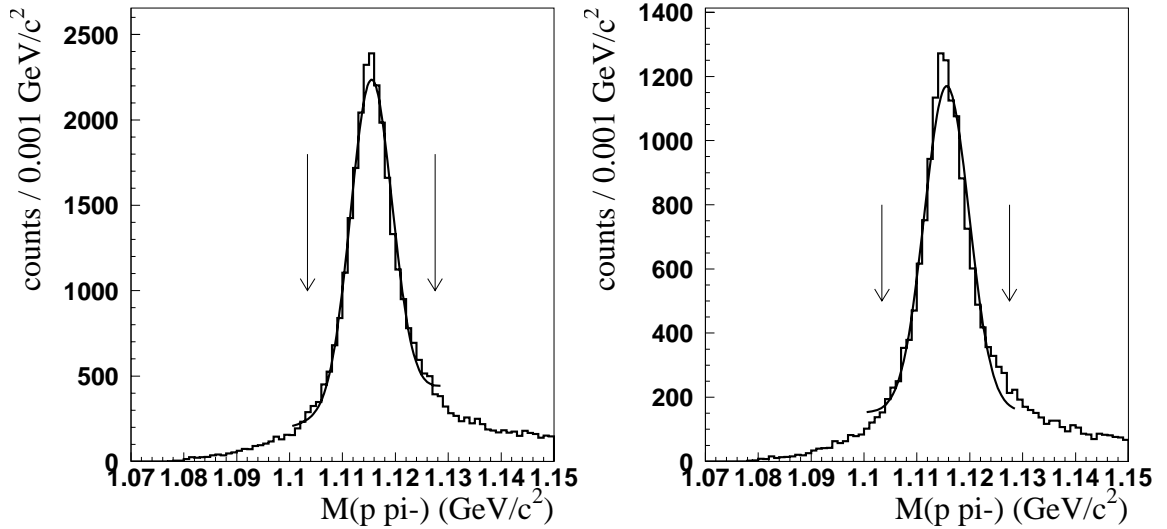


Figure 3.11: Invariant mass spectra of $(p\ \pi^-)$ pairs for $CH_2$ (left) and carbon (right). The solid lines and the arrows show the fit results and the boundaries of Λ selection cut, respectively.

The mass peak values were obtained from a Gaussian fit with a linear background assumption to be $1115.4\pm0.4$ MeV/$c^2$ and $1115.6\pm0.4$ MeV/$c^2$ for $CH_2$ and carbon, respectively. The solid lines in Fig. 3.11 show fit results, and the arrows indicate the boundaries of the Λ selection cut. The measured widths (RMS) were $3.9 \pm 0.5$ MeV/$c^2$ and $4.2 \pm 0.8$ MeV/$c^2$ for $CH_2$ and carbon, respectively. The observed masses are consistent with the PDG value of $1115.6$ MeV/$c^2$, and the widths are consistent with the expected value of $4$ MeV/$c^2$ by a Monte Carlo (MC) simulation. Events in $3\ \sigma$ region were retained for further analysis.

### 3.3.2   $MM(K^+)$ distribution for $\Lambda$ tagged events

The distribution of $MM(K^+)$ for events which survived the $\Lambda(1116)$ selection cut is shown in Fig. 3.12 (a), the solid and dashed histograms are the spectra for $CH_2$ and carbon, respectively. Fig. 3.12 (b) shows a spectrum for free protons. Closed circles show the experimental data, and arrows indicate the PDG values of mass of $\Lambda(1116)$, $\Sigma(1192)$ and $\Sigma^0(1385)$ .
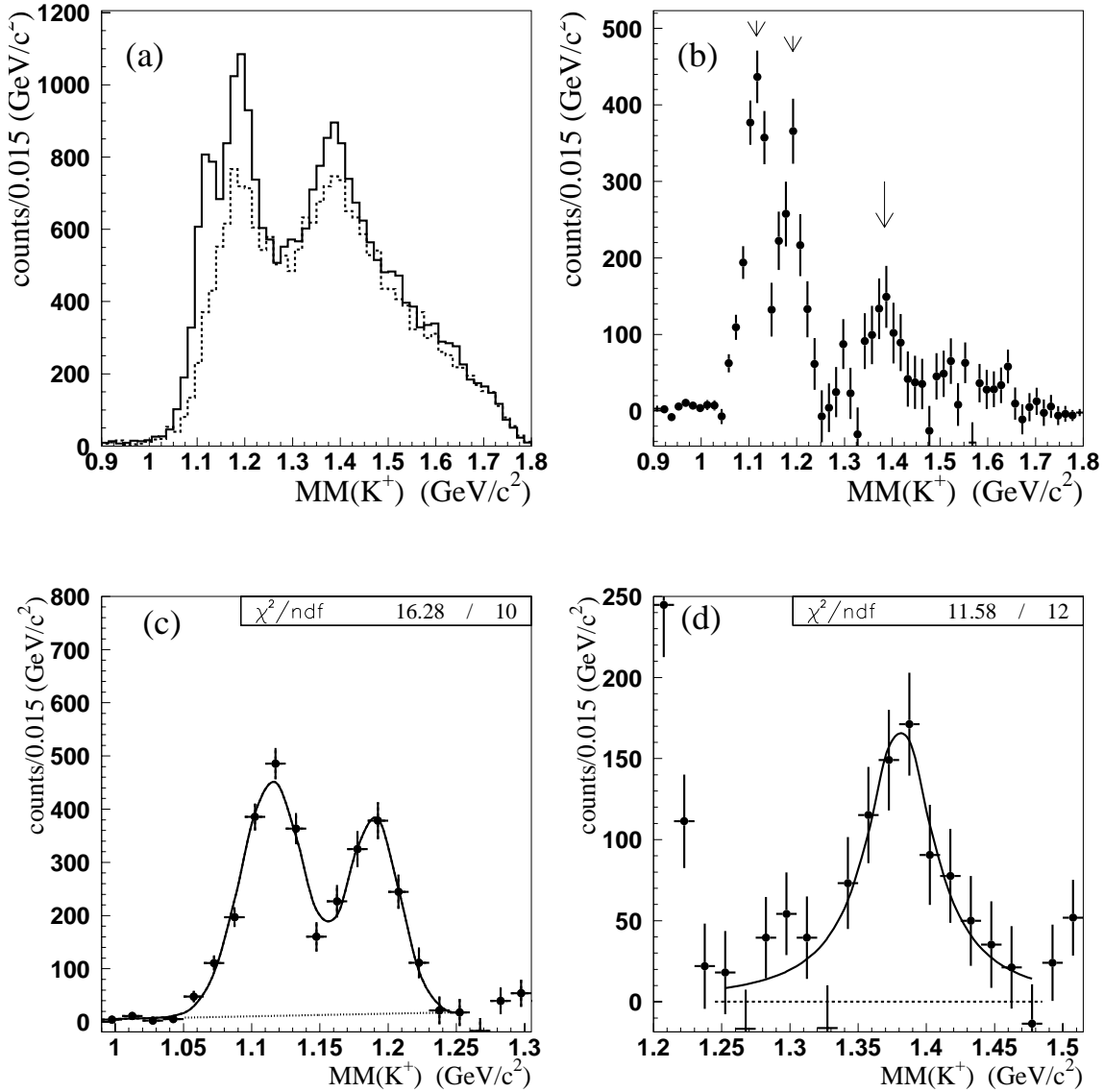


Figure 3.12: Missing mass of the $\gamma p \rightarrow K^+ X$ reaction after the $\Lambda$ selection cut. (a) shows spectra for the $CH_2$ target (solid histogram) and for the carbon target (dashed histogram). (b), (c) and (d) show spectra for free protons in the $CH_2$ target.

Figure 3.12 (c) shows the distribution of $MM(K^+)$ for free protons around $\Lambda(1116)$ mass region. The mass peak positions were obtained by fitting two Gaussians to the data, assuming a linear background. The measured masses of $\Lambda(1116)$ and $\Sigma^0(1192)$ were $1115 \pm 2$ MeV/c$^2$ and $1192 \pm 3$ MeV/c$^2$ respectively. They are consistent with the PDG values. The width of $\Lambda(1116)$ was obtained as $25 \pm 2$ MeV/c$^2$, which is consistent with the expected value of 22 MeV/c$^2$ by the MC simulation. The observed width of $\Sigma^0(1192)$ was also consistent with the expected value. Figure 3.12 (d) shows $MM(K^+)$ distribution around $\Sigma^0(1385)$ mass region. For the resonance around 1.4 GeV/c$^2$, we assumed a Breit-Wigner shape, neglecting any distortion due to the small contamination of $\Lambda(1405)$. The effect of this contamination is considered in the next section. The mass of $\Sigma^0(1385)$ was obtained from a Breit-Wigner fit with a linear background assumption to be $1383 \pm 7$ MeV/c$^2$. The obtained width (FWHM) was $67 \pm 23$ MeV/c$^2$. They are consistent with the PDG value and an expected width of 50 MeV/c$^2$ by the MC simulation.

### 3.3.3   Background of $\Lambda(1405) \to \Sigma^0\pi^0$ mode

In this section, the estimation of the contamination of the $\Lambda(1405)$ production ( reaction 3.1), $\gamma p \to K^+\Lambda(1405) \to K^+\Sigma^0\pi^0 \to K^+\Lambda\gamma\pi^0$, is described. The contamination was estimated in two photon energy ranges: $1.5 < E_\gamma < 2.0$ GeV and $2.0 < E_\gamma < 2.4$ GeV. Fig. 3.13 shows the missing mass of $\gamma p \to K^+p\pi^-X$ reaction ($MM(K^+p\pi^-)$) after the $\Lambda$ selection cut and the cut of $\Lambda(1405)$ and $\Sigma^0(1385)$ selection, $1.3 < MM(K^+) < 1.45$ GeV/c$^2$.
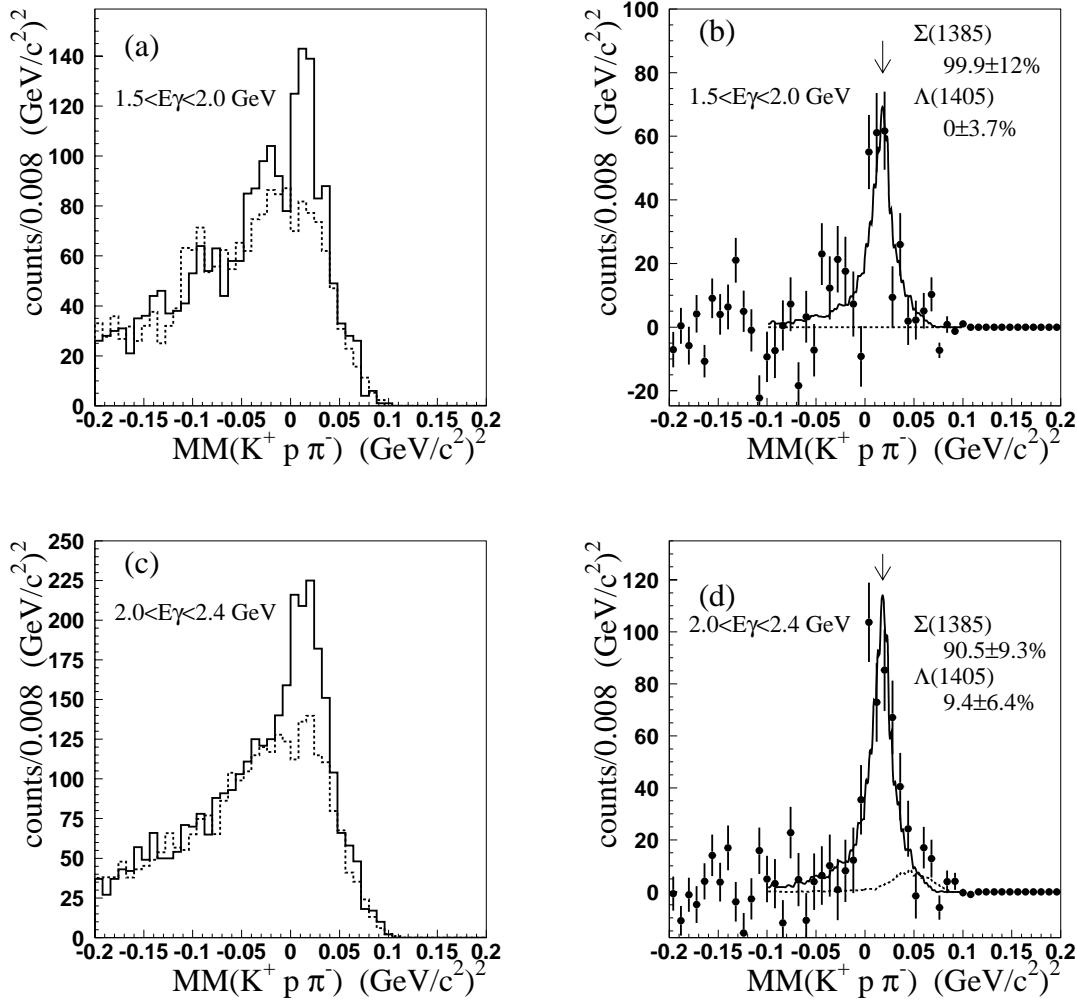


Figure 3.13: Distribution of the $MM(K^+ \, p \, \pi^-)$ after the $\Lambda$ selection cut and the cut of $1.3 < $ MM $(K^+) < 1.45$ GeV/c$^2$ in two photon energy ranges: $1.5 < E_\gamma < 2.0$ GeV (a), (b) and $2.0 < E_\gamma < 2.4$ GeV (c), (d). Plot (a) and (c) show spectra for CH$_2$ (solid) and carbon (dashed). Closed circles in plot (b) and (d) show spectra for free protons. Solid and dashed histograms in plot (b) and (d) show expected spectra for the signal of $\Sigma^0(1385)$ and the background of $\Lambda(1405)$ production, respectively.

The solid and dashed histograms in Fig. 3.13 (a) and (c) show spectra for $CH_2$ and carbon, respectively. Closed circles in (b) and (d) show spectra for free protons, and the solid and dashed histogram shows the expected spectrum for the signal of $\Sigma^0(1385)$ production and the background reaction (3.1) as generated by the MC simulation, respectively. The spectrum for free protons in $CH_2$ was obtained from the spectrum of $CH_2$ after subtracting the one of carbon with the proper normalization. In order to reduce statistical fluctuation, the spectrum for carbon was smoothed by smearing photon energies before the subtraction. For each event, the photon energy was smeared by Gaussian random numbers with the width of 15 MeV and missing masses were calculated using smeared photon energies. The arrows in plot (b) and (d) indicate the mass squared of $\pi^0$. The peaks corresponding to $\pi^0$ are clearly visible. The contamination was found to be small in each photon energy region. In the low photon energy range, the contamination was consistent with 0. On the other hand, that in the high photon energy range was found to be $9.4\pm6.4\%$. However, the contamination is consistent with zero in $1.5\sigma$. In addition, the yield of $\Lambda(1405)$ was found to decrease in higher photon energy region from the analysis of the $\Lambda(1405) \rightarrow \Sigma^\pm\pi^\mp$ modes as described in the section 3.4. Thus, the contamination was neglected in the both photon energy regions.

## 3.3.4    Background of $\Lambda(1405)/\Sigma^0(1385) \to \Sigma^+\pi^-$ mode

In this section, the contamination from the reaction (3.2), $\gamma p \to K^+\Lambda(1405)/\Sigma^0(1385) \to K^+\Sigma^+\pi^- \to K^+\, p\, \pi^0\, \pi^-$, is estimated. Since the particles in the final state are same as those of $\Sigma^0(1385) \to \Lambda\pi^0 \to p\pi^-\pi^0$ mode, these two reactions cannot be separated in $MM(K^+\, p\, \pi^-)$ distribution. Moreover, the distribution of $MM(K^+\pi^-)$ for $\Sigma^0(1385) \to \Lambda\pi^0$ reaction has a peak around 1.2 GeV/c$^2$ which is close to $\Sigma^+$ mass, 1.189 GeV/c$^2$. Figure 3.14 shows the distributions of $MM(K^+\pi^-)$ for $K^+\Sigma^0(1385)$ production (left) and that for $K^+\Lambda(1405)$ production (right) generated by the MC simulation.
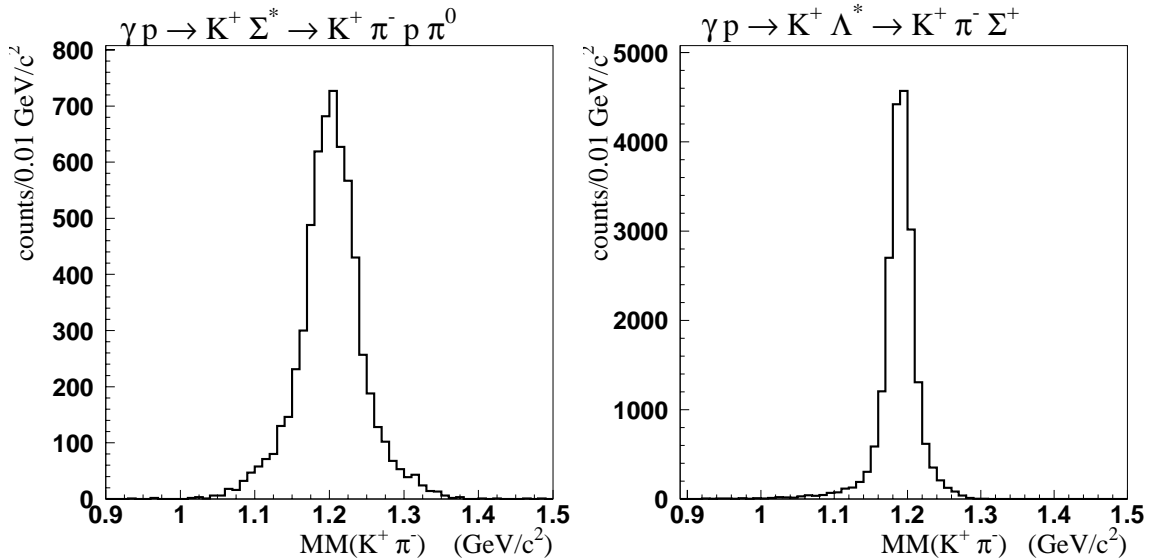


Figure 3.14:   Distributions of $MM(K^+\pi^-)$ obtained by the MC simulation of $\Sigma^0(1385)$ photoproduction (left) and $\Lambda(1405)$ photoproduction (right).

The contamination from the reaction (3.2) was estimated from the distribution of $MM(K^+\pi^-)$ for events which were rejected by the $\Lambda$ selection cut. Figure 3.15 shows the distribution of $M(p\pi^-)$ for $\Sigma^0(1385) \to \Lambda\pi^0$ reaction (left) and for $\Lambda(1405) \to \Sigma^+\pi^-$ reaction (right) which were generated by the MC simulation. The spectrum for $\Sigma^0(1385)$ production has a peak around $\Lambda$ mass, while the one for $\Lambda(1405)$ production shows a broad distribution. The cut of $M(p\pi^-) > 1.13$ GeV/c$^2$ was applied to reject $\Lambda\pi^0$ decay of $\Sigma^0(1385)$ .
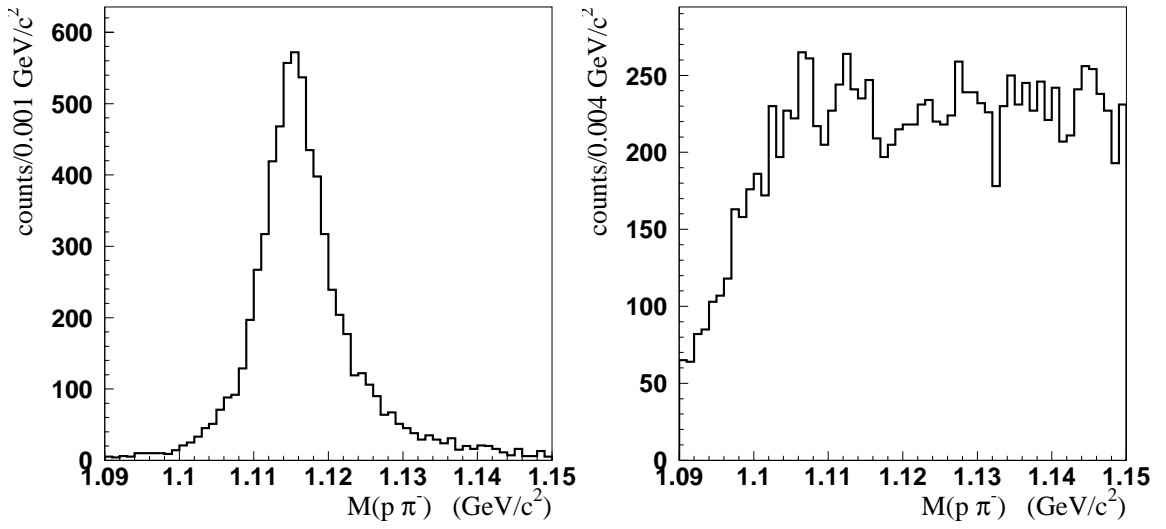
Figure 3.15: Distribution of the invariant mass of $(p\pi^-)$ pairs obtained by the Mont-Carlo simulation of $\Sigma^0(1385)$ photoproduction (left) and $\Lambda(1405)$ photoproduction (right).

Closed circles in Fig 3.16 show the distributions of $MM(K^+\pi^-)$ in two photon energy bins for events which survived $\Lambda$ rejection cut and the cut of $\Lambda(1405)$ and $\Sigma^0(1385)$ selection, $1.38 < MM(K^+) < 1.45$ GeV/$c^2$. The spectrum was fitted with the expected spectrum of $(K^+\Lambda(1405))$ production generated by the MC and the background spectrum due to the particle misidentification by the LEPS spectrometer. The fit results are shown as solid curves. The yields of $\Sigma^+\pi^-$ decay of $\Lambda(1405)$ and $\Sigma^0(1385)$ were found to be $150 \pm 29$ events and $136 \pm 38$ events for $1.5 < E_\gamma < 2.0$ GeV and $2.0 < E_\gamma < 2.4$ GeV, respectively.
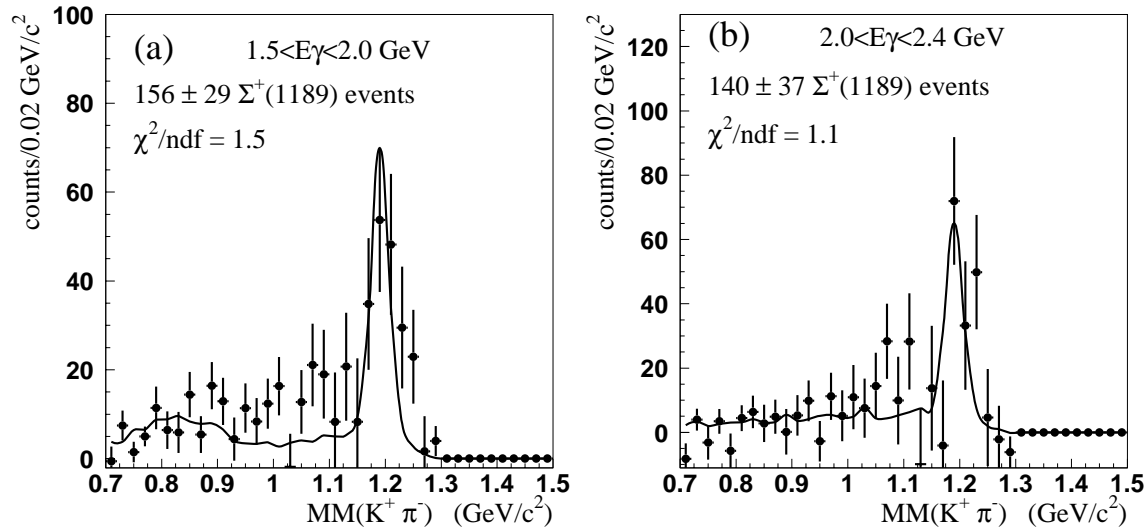


Figure 3.16: $MM(K^+\pi^-)$ for events which survived the $\Lambda$ rejection cut and the cut of $1.38 < MM(K^+) < 1.45$ GeV/$c^2$ for free protons in $CH_2$ in photon energy range of $1.5 < E_\gamma < 2.0$ GeV (a) and $2.0 < E_\gamma < 2.4$ GeV (b).

The contamination of $\Lambda(1405)/\Sigma^0(1385) \to \Sigma^+\pi^-$ mode to $\Sigma^0(1385) \to \Lambda\pi^0$ mode was obtained after taking into account of the acceptance for the $\Lambda$ selection cut and the cut of $1.38 < MM(K^+) < 1.45$ GeV/$c^2$. The acceptance for the cut of $1.38 < MM(K^+) < 1.45$ GeV/$c^2$ was obtained by the MC simulation to be 81% in each photon energy region, and that for the $\Lambda$ selection cut was 25% for $1.5 < E_\gamma < 2.0$ GeV and 28% for $2.0 < E_\gamma < 2.4$ GeV. The numbers of events due to the background reaction (3.2) were found to be $48 \pm 9$ events and $49 \pm 14$ events for $1.5 < E_\gamma < 2.0$ GeV and $2.0 < E_\gamma < 2.4$ GeV, respectively.

### 3.3.5   Yield estimation of $\Sigma^0(1385)$

The number of events in the $\Sigma^0(1385)$ mass region including the background reactions of (3.1) and (3.2) was obtained to be $779\pm163$ events by fitting the spectrum of $\Sigma^0(1385)$ together with the phase space distribution of $(K^+\Lambda\pi^0)$ production which were generated by the MC simulation. The solid histogram in Fig. 3.17 (a) shows the fit result, and the dashed one shows the phase space distribution of $(K^+\Lambda\pi^0)$ production. The yields in two photon energy regions, $1.5 < E_\gamma < 2.0$ GeV and $2.0 < E_\gamma < 2.4$ GeV, were obtained from the photon energy distribution in the missing mass region of $1.3 < MM(K+) < 1.45$ GeV/c$^2$, since the background of nonresonant $(K^+\Lambda\pi^0)$ production was small. Fig. 3.17 (b) shows the photon energy distribution around $1.3 < MM(K^+) < 1.45$ GeV/c$^2$. The ratio of the yield in $1.5 < E_\gamma < 2.0$ GeV to that in $2.0 < E_\gamma < 2.4$ GeV was obtained as $0.48 \pm 0.02$. The yields of events under the peak including the $\Sigma^0(1385)$ and the background were $255 \pm 55$ events for $1.5 < E_\gamma < 2.0$ GeV and $525 \pm 111$ events for $2.0 < E_\gamma < 2.4$ GeV.
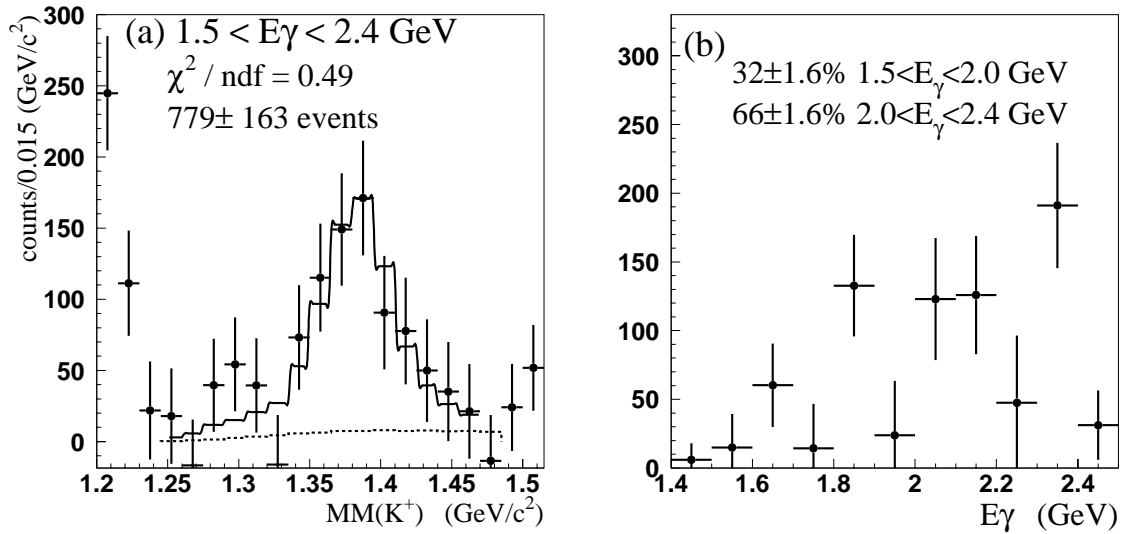


Figure 3.17: (a) $MM(K^+)$ for $\Lambda$ tagged events. The solid and dashed histograms show the fit result and the phase space distribution of $(K^+\Lambda\pi^0)$ production, respectively. (b) Distribution of photon energies for events which survived the $\Lambda$ selection cut and the cut of $1.3 < MM(K^+) < 1.45$ GeV/c$^2$.

Fig. 3.18 shows the distribution of $MM(K^+)$ for $\Lambda$ tagged events in two photon energy regions. In order to reduce the statistical fluctuations, spectra for the carbon target were again smoothed with the photon smearing with 15 MeV energy resolution. Plot (a) and (b) show spectra for $1.5 < E_\gamma < 2.0$ GeV, and plot (c) and (d) show those for $2.0 < E_\gamma < 2.4$ GeV.
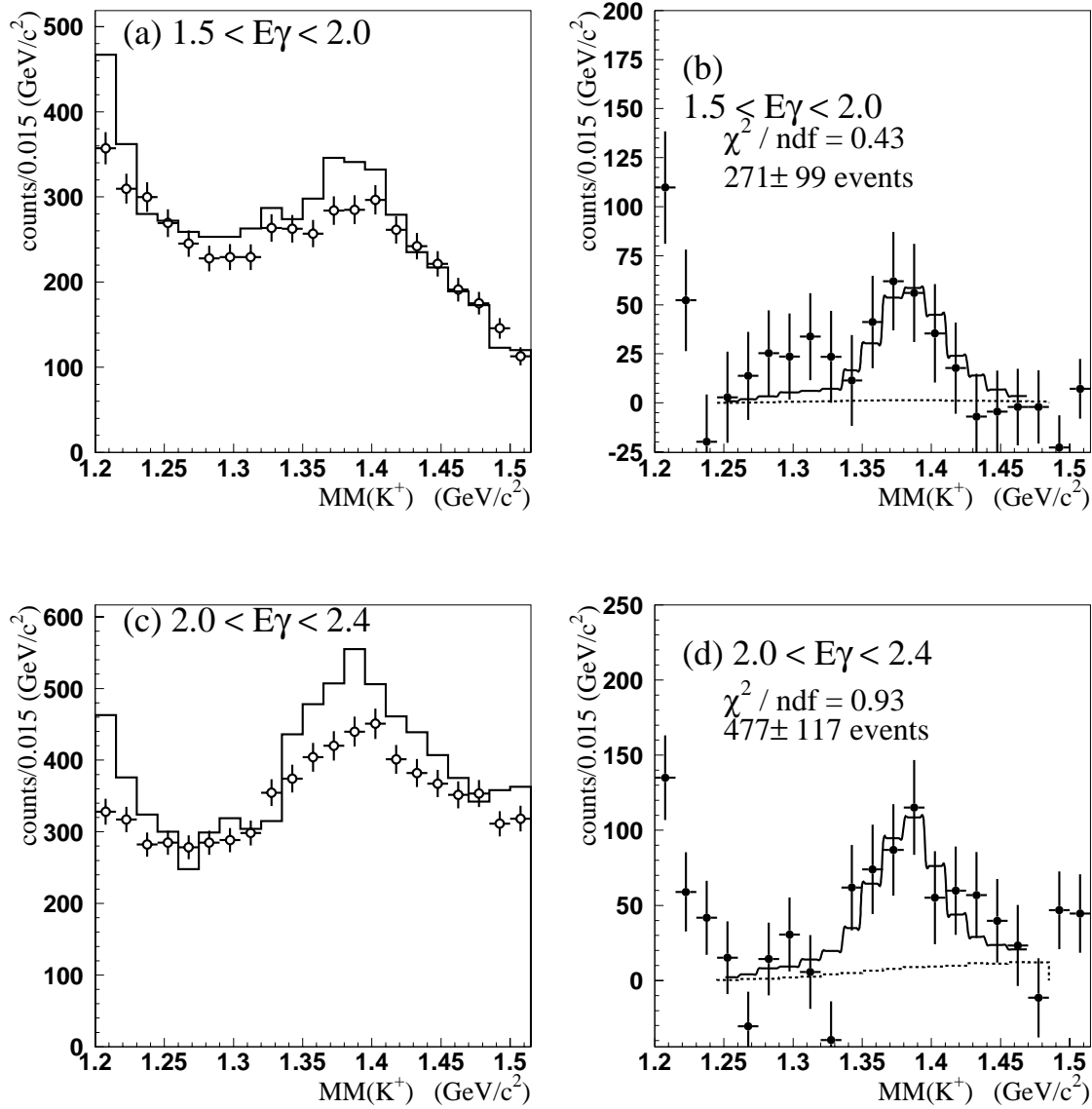


Figure 3.18: $MM(K^+)$ for $\Lambda$ tagged events in two photon energy regions. Solid histograms and open circles in (a) and (c) show spectra for $CH_2$ and carbon after smoothing, respectively. The closed circles in (b) and (d) show spectra for free protons.

The solid histograms in Fig. 3.18 (a) and (c) show spectra for $CH_2$, and open circles show smoothed spectra for carbon. Closed circles in Fig. 3.18 (b) and (d) show spectra for free protons. The solid histograms in Fig. 3.18 (b) and (d) show the expected spectra of $(K^+\Sigma^0(1385))$ generated by the MC simulation. In the simulation, the spectrum shape of $\Sigma^0(1385)$ was assumed to be a Breit-Wigner function with the width listed in the PDG, and the missing mass resolution due to the resolutions of the measurement of the photon energy and momentum of $K^+$ is taken into account. In order to estimated the background under the peak, the phase space distribution of nonresonant $(K^+\Lambda\pi^0)$ production was used for fitting. The heights of each contribution were obtained by fitting. Spectra of nonresonant $(K^+\Lambda\pi^0)$ production are shown as dashed histograms. The numbers of events under the peak were obtained by a fit to the data to be $271 \pm 99$ events for $1.5 < E_\gamma < 2.0$ GeV and $477 \pm 117$ events for $2.0 < E_\gamma < 2.4$ GeV. The ratio of the number of events between two photon energy regions was found to be $0.57 \pm 0.25$, which was consistent with the value obtained from the photon energy distribution.

The numbers of events under the peak obtained from the photon energy distribution were used to extract the yield of the $\Sigma^0(1385)$, because those obtained from the distribution of $MM(K^+)$ in two photon energy regions strongly depend on the width of the photon energy smearing for the spectrum for the carbon target. The yield of $\Sigma^0(1385)$ was found to be $207 \pm 56$ events for $1.5 < E_\gamma < 2.0$ GeV and $475 \pm 112$ events for $2.0 < E_\gamma < 2.4$ GeV after subtracting the contamination of background reaction (3.2). The numbers of events used to obtain the yield of $\Sigma^0(1385)$ are summarized in Table 3.2. The $\Sigma^0(1385)$ has a decay branch of $\Sigma^\pm\pi^\mp$ with $11.7 \pm 1.5\%$, which is the decay mode of $\Lambda(1405)$. The yields of $\Sigma^0(1385)$ in $\Sigma^+\pi^-$ and $\Sigma^-\pi^+$ modes were estimated using the acceptance estimated by the MC simulation assuming flat decay angular distributions. The estimated yields of $\Sigma^0(1385)$ in $\Sigma^+\pi^-$ and $\Sigma^-\pi^+$ modes are summarized in Table 3.3.

Table 3.2: Summary of the yield of $\Sigma^0(1385)$ photoproduction

| | $1.5 < E_\gamma < 2.0$ | $2.0 < E_\gamma < 2.4$ |
|---|---|---|
| yield in $\Lambda\pi^0$ mode | $255 \pm 55$ | $525 \pm 111$ |
| contamination $\Lambda^* \to \Sigma^0\pi^0$ | $0$ | $0.$ |
| contamination $\Lambda^*/\Sigma^* \to \Sigma^+\pi^-$ | $48 \pm 9$ | $49 \pm 14$ |
| yield of $\Sigma^0(1385)$ | $207 \pm 56$ | $476 \pm 112$ |

Table 3.3: Summary of the yield of $\Sigma^0(1385)$ in $\Sigma\pi$ mode

| | $1.5 < E_\gamma < 2.0$ | $2.0 < E_\gamma < 2.4$ |
|---|---|---|
| acceptance of $\Sigma^0(1385) \to \Lambda\pi^0$ | 0.057 | 0.093 |
| yield of $\Sigma^0(1385) \to \Lambda\pi^0$ | $3.6 \pm 0.98 \times 10^3$ | $5.1 \pm 1.2 \times 10^3$ |
| acceptance corrected yield of $\Sigma^0(1385)$ | $4.1 \pm 1.1 \times 10^3$ | $5.8 \pm 1.4 \times 10^3$ |
| acceptance of $\Sigma^0(1385) \to \Sigma^-\pi^+$ | 0.12 | 0.15 |
| yield of $\Sigma^0(1385) \to \Sigma^+\pi^-$ | $14 \pm 4.3$ | $25 \pm 5.9$ |
| yield of $\Sigma^0(1385) \to \Sigma^-\pi^+$ | $30 \pm 8.8$ | $52 \pm 12$ |

## 3.4 Photoproduction of $\Lambda(1405)$

In this section, the analysis for the measurement of $\Lambda(1405)$ photoproduction is described. The $\Lambda(1405)$ was investigated using following reaction,

$$
\begin{aligned}
\gamma\, p \;\; &\rightarrow \;\; K^+\, \Lambda^*(1405) \\
&\rightarrow \;\; K^+\, \Sigma^\pm\, \pi^\mp \\
&\rightarrow \;\; K^+\, n\, \pi^+\, \pi^- \; .
\end{aligned}
$$
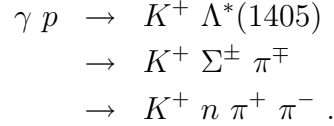
First of all, the $K^+$'s were identified by the LEPS spectrometer as same as the analysis of $K^+\Sigma(1385)$ production. Secondly, neutrons were identified from the missing mass of the $\gamma p \rightarrow K^+\pi^+\pi^- X$ reaction ($MM(K^+\pi^+\pi^-)$) for events in which a $(\pi^+\pi^-)$ pair was identified from the $dE/dx$ and momentum measured by the TPC. In high momentum region, a proton was misidentified as a $\pi^+$ since the energy deposition of the high momentum proton become small, and the separation from $\pi^+$ is difficult. In order to eliminate these background events, an event selection cut was applied in the missing mass of the $\gamma p \rightarrow K^+ p\pi^- X$ reaction ($MM(K^+ p\pi^-)$). Thirdly, a $\Sigma^+$ or a $\Sigma^-$ was identified in the missing mass of $\gamma p \rightarrow K^+\pi^\pm$ reactions ($MM(K^+\pi^\pm)$). The events of $\Lambda(1405)$ production were purified using a kinematic fit requiring $MM(K^+\pi^+\pi^-) = M_n$ and $MM(K^+\pi^\pm) = M_{\Sigma^\mp}$, where $M_n$ and $M_{\Sigma^\pm}$ were the masses of the neutron and $\Sigma^\pm$, respectively. Then, the yield of the $\Lambda(1405)$ was extracted from a peak in the $MM(K^+)$ for the $(K^+\Sigma^\pm\pi^\mp)$ final state after subtracting the contamination from $\Sigma^0(1385) \rightarrow \Sigma^\pm\pi^\mp$ mode which was estimated in the previous section and the contamination of $(K^0(892)\Sigma^+)$ production. The outline of the analysis is as follows, (1) selection of a $K^+$ by the LEPS spectrometer, (2) selection of a $(\pi^+\pi^-)$ pair by the TPC, (3) reduction of background events due to $p/\pi^+$ misidentification by TPC using $MM(K^+ p\pi^-)$, (4) neutron selection in $MM(K^+\pi^+\pi^-)$, (5) $\Sigma^+$ or $\Sigma^-$ selection by the kinematic fit. The numbers of events which survived these conditions are listed in Table 3.4.

Table 3.4: Summary of the number of events which survived cuts.

| Selection cuts | number of events ($CH_2$) | number of events (C) |
|---|---|---|
| number of tracks in TPC $\geq 2$ | $9.18 \times 10^4$ | $4.77 \times 10^4$ |
| $\pi^+\pi^-$ selection in TPC | $4.92 \times 10^4$ | $2.46 \times 10^4$ |
| $MM(K^+ p\pi^-) < -0.05$ $(\mathrm{GeV/c^2})^2$ | $3.33 \times 10^4$ | $1.73 \times 10^4$ |
| neutron selection | $6.46 \times 10^3$ | $2.59 \times 10^3$ |
| $\chi^2$ probatility cut of kinematic fit | $2.98 \times 10^3$ | $7.96 \times 10^2$ |
| $\Sigma^+$ selection by kinematic fit | $1.48 \times 10^3$ | $4.00 \times 10^2$ |
| $\Sigma^-$ selection by kinematic fit | $1.50 \times 10^3$ | $3.96 \times 10^2$ |

### 3.4.1   Neutron identification

Neutrons were identified from the missing mass of the $\gamma p \to K^+\pi^+\pi^- X$ reaction $(MM(K^+\pi^+\pi^-))$, where the $K^+$ was detected by the LEPS spectrometer as same as the analysis for $\Sigma^0(1385)$ production. Then, a $(\pi^+\pi^-)$ pair was identified by the TPC using the information of the $dE/dx$ and momentum of particles. Figure 3.19 shows the distribution of $MM(K^+\pi^+\pi^-)$. The solid and dashed histograms show spectra for $CH_2$ and carbon, respectively. The right plot shows a spectrum for free protons in $CH_2$, which was obtained by subtracting the spectrum of carbon from that of $CH_2$. The arrows indicate the neutron mass. A peak corresponding to the neutron mass at 0.939 $GeV/c^2$ is clearly seen. The background at lower side of the neutron mass was caused by particle misidentification in TPC as described below.
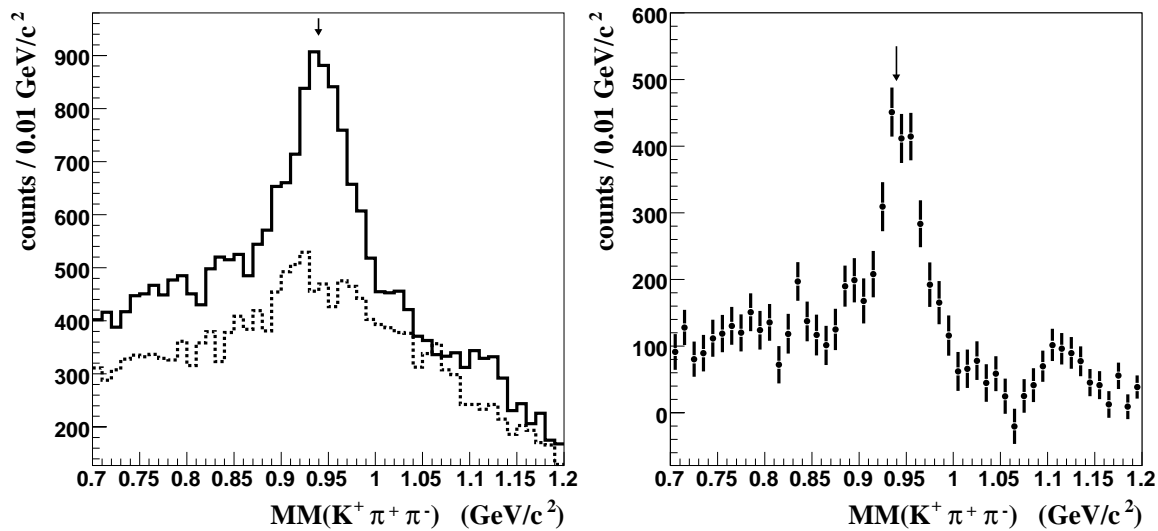


Figure 3.19: Missing mass of the $\gamma p \to K^+\pi^+\pi^- X$ reaction. The left plot shows spectra for the $CH_2$ target (solid histogram) and the carbon target (dashed one). The right plot shows a spectrum for free protons in $CH_2$. The arrows indicate the neutron mass.

Fig. 3.20 shows a correlation plot between the $dE/dx$ and momentum of $\pi^+$ candidates in the background region, $0.7 < MM(K^+\pi^+\pi^-) < 0.85\,\mathrm{GeV/c^2}$. One can see the contamination of protons in the momentum range from 0.4 to 0.8 GeV/c, as indicated by the arrow in the plot. These protons were produced by either the $\gamma\,p \to K^+\Sigma^0(1385) \to K^+\Lambda\pi^0 \to K^+p\pi^-\pi^0$ reaction or $\gamma\,p \to K^+\Lambda(1405) \to K^+\Sigma^+\pi^- \to K^+p\pi^0\pi^-$ reaction. In both reactions, the missing mass of the $\gamma p \to K^+p\pi^-X$ reaction, $MM(K^+p\pi^-)$, corresponds to the $\pi^0$ mass. Thus, these background events can be eliminated by rejecting events for which $MM(K^+p\pi^-)$ corresponds to $\pi^0$ mass, where a $\pi^+$ candidate was assumed as a proton and assigned the proton mass. Fig. 3.20 (b) shows the distribution of the square of $MM(K^+p\pi^-)$. Closed circles show the experimental data. The arrows indicate the $\pi^0$ mass squared and the cut point for the $\pi^0$ rejection. The enhancement of the spectrum at the $\pi^0$ mass due to the background reactions is clearly visible. The solid histogram shows the expected spectrum for the background reaction of $\Sigma^0(1385) \to \Lambda\pi^0 \to p\pi^-\pi^0$ which was generated by the MC simulation. The contamination from this reaction was reduced by requiring the cut of $MM^2(K^+\,p\,\pi^-) < -0.05\,(\mathrm{GeV/c^2})^2$. The expected spectrum from the signal of $\Lambda(1405)$ production is displayed as the dashed histogram. The acceptance of the cut $MM^2(K^+\,p\,\pi^-) < -0.05\,(\mathrm{GeV/c^2})^2$ for $\Lambda(1405)$ was estimated to be 85% by the MC simulation.
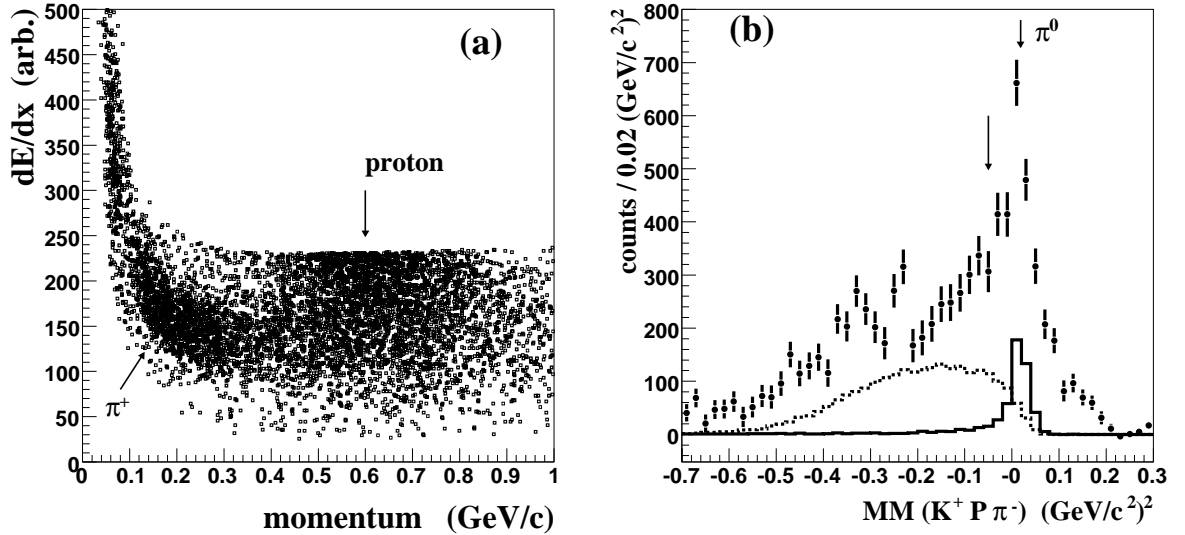


Figure 3.20: (a) Correlation plot between the $dE/dx$ and the momentum of the $\pi^+$ candidates in the background region, $0.7 < MM(K^+\pi^+\pi^-) < 0.85\,\mathrm{GeV/c^2}$. (b) Distribution of missing mass squared for the $\gamma p \to K^+\,p\,\pi^-X$ reaction. The closed circles show experimental data, and the solid and dashed histograms show expected spectra by the MC simulation for the background reaction of $\Sigma^0(1385)$ production and the signal of $\Lambda(1405)$ production, respectively.

Figure 3.21 shows the distribution of $MM(K^+\pi^+\pi^-)$ for events which survived the cut of $MM^2(K^+p\pi^-) < -0.05$ $(GeV/c^2)^2$. The solid and dashed histograms in Fig. 3.21 (a) show spectra for $CH_2$ and carbon, respectively. A spectrum for free protons is shown in Fig. 3.21 (b). The background events in $MM(K^+\pi^+\pi^-) < 0.85$ GeV/$c^2$ were significantly reduced, and a peak corresponding to the neutron mass is clearly visible. The remaining background events in this mass region were likely due to misidentification of a proton or $\pi^+$ as the $K^+$ by the LEPS spectrometer. The estimation of this background is described in Appendix D. The contamination of of this background into the neutron mass region was estimated to be 8%. The enhancement of events around 1.1 GeV/$c^2$ corresponds to the events in which an additional $\pi^0$ is produced.
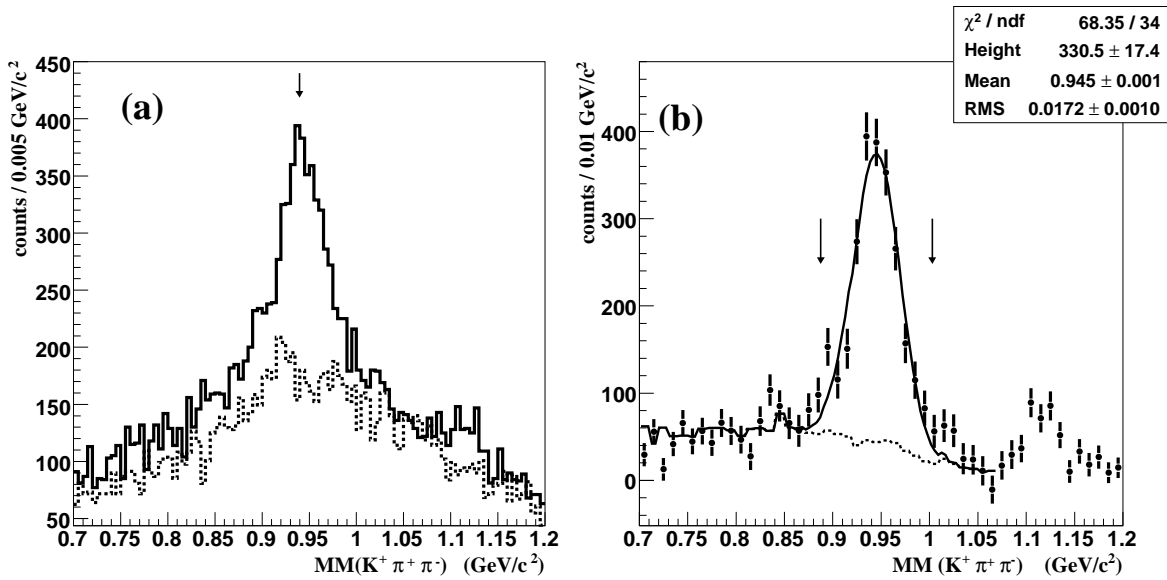


Figure 3.21: Distribution of $MM(K^+\pi^+\pi^-)$ for events which survived the cut of $MM^2(K^+p\pi^-) < -0.05$ $(GeV/c^2)^2$. The solid and dashed histograms in (a) show spectra for $CH_2$ and carbon, respectively. Closed circles in (b) show a spectrum for free protons. The solid and dashed lines in (b) show the fit result and the background due to the particle misidentification by the LEPS spectrometer, respectively.

The mean value and RMS width were obtained from a Gaussian fit to the data to be $945 \pm 1$ MeV/$c^2$ and $17 \pm 2$ MeV/$c^2$, respectively. The measured width was consistent with the expected value of 18 MeV/$c^2$ by the MC simulation, but the mean value was slightly higher than the PDG value of the mass of neutron, 939 MeV/$c^2$. The solid and dashed lines in (b) show the fit result and the background due to the particle misidentification by the LEPS spectrometer, respectively. The neutron selection boundaries were set to $0.89 < MM(K^+\pi^+\pi^-) < 1.00$ GeV/$c^2$, corresponding to $3\sigma$ selection.

## 3.4.2 Event selection by the kinematic fit

The $\Sigma^+$ and $\Sigma^-$ from the decay of the $\Lambda(1405)$ can be identified from the missing mass of the $\gamma p \to K^+\pi^- X$ reaction and $\gamma p \to K^+\pi^+ X$ reaction, respectively. Fig. 3.22 (a) shows the distributions of $MM(K^+\pi^-)$ (solid histogram) and $MM(K^+\pi^+)$ (dashed histogram) from free protons in $CH_2$ for events which survived the neutron selection cut and the cut of $MM^2(K^+p\pi^-) < -0.05$ $(GeV/c^2)^2$. The peaks corresponding to $\Sigma^+$ and $\Sigma^-$ is seen. The arrows indicate the masses of $\Sigma^+$ (1.189 $GeV/c^2$) and $\Sigma^-$ (1.197 $GeV/c^2$). Fig. 3.22 (b) shows the correlation between $MM(K^+\pi^+)$ and $MM(K^+\pi^-)$. Some of events are in the region where $MM(K^+\pi^+) \sim MM(K^+\pi^-) \sim 1.2$ $GeV/c^2$. For such events, it is impossible to separate the $\Sigma^+$ and $\Sigma^-$ from the missing mass.
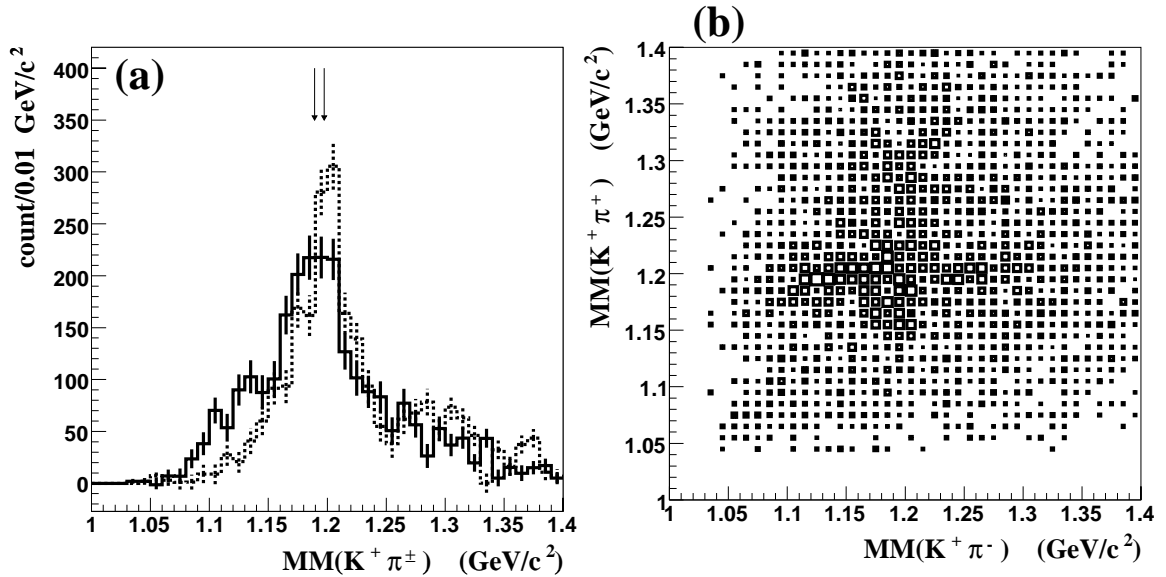


Figure 3.22: Distributions of $MM(K^+\pi^+)$ and $MM(K^+\pi^-)$. (a) Solid and dashed histograms show the distribution of $MM(K^+\pi^-)$ and $MM(K^+\pi^+)$, respectively. (b) Correlation between $MM(K^+\pi^+)$ and $MM(K^+\pi^-)$.

In order to separate $\Sigma^+$ and $\Sigma^-$, a kinematic fit was used with two constraints: $MM(K^+\pi^+\pi^-) = M_n$ and $MM(K^+\pi^\pm) = M_{\Sigma^\mp}$, where $M_n$ and $M_{\Sigma^\mp}$ stand for the mass of neutron and $\Sigma^\mp$, respectively. The kinematical variables for the fit were, the photon energy ($E_\gamma$), the three momenta of the $K^+$, $\pi^+$ and $\pi^-$. The resolution of photon energy was obtained by the measurement [53]. The momentum and angular resolution of reconstructed tracks were obtained from the Monte Carlo simulation. The resolutions used in the kinematic fit are summarized in Table 3.5. The momentum resolution of the LEPS spectrometer, $\sigma^2(p_{spec})$, consists of the contributions of the spatial resolution of the drift chamber (first term) and the multiple scattering effect (second term).

Table 3.5: The resolutions of kinematic variables for the kinematic fit. The variables with the suffix of *spec* and *TPC* represent those measured by the LEPS spectrometer and the TPC, respectively.

| Variable | Resolution |
|---|---|
| $\sigma(E_\gamma)$ GeV | 15 MeV |
| $\sigma^2(p_{spec})$ (GeV/c)$^2$ | $p_{spec}^2 \cdot ((0.003 \cdot p_{spec})^2 + (0.005)^2 \cdot (1. + (M_K/p_{spec})^2))$ |
| $\sigma(\theta_{spec})$ rad | 0.001 |
| $\sigma(\phi_{spec})$ rad | 0.005 |
| $\sigma^2(p_{TPC})$ (GeV/c)$^2$ | $0.002 \cdot p_{TPC}^2$ |
| $\sigma(\theta_{TPC})$ rad | 0.009 |
| $\sigma(\phi_{TPC})$ rad | 0.013 |

Since the mass difference between $\Sigma^+$ (1189.3 MeV/c$^2$) and $\Sigma^-$ (1197.2 MeV/c$^2$) was not negligible, the kinematic fit was applied twice for each event firstly with the $\Sigma^+\pi^-$ decay assumption and secondly with the $\Sigma^-\pi^+$ decay assumption. Figure 3.23 (a) and (b) show the distribution of the $\chi^2$ probability with $\Sigma^+\pi^-$ decay assumption ($prob_{\Sigma^+}(\chi^2)$) and that with $\Sigma^-\pi^+$ decay assumption ($prob_{\Sigma^-}(\chi^2)$), respectively. The solid (dashed) histogram shows the distribution for CH$_2$ (carbon). The mean of the probability for carbon is smaller than that for CH$_2$ due to Fermi motion of target protons in the nucleus.
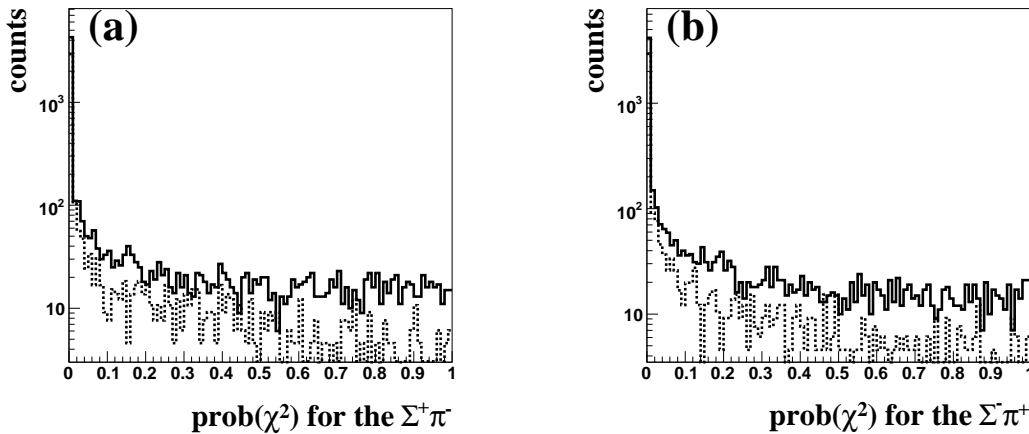


Figure 3.23: Distributions of $\chi^2$ probability for the kinematic fit with $\Sigma^+\pi^-$ decay assumption (a) and with $\Sigma^-\pi^+$ decay assumption (b). The solid (dashed) histogram shows the distribution for CH$_2$ (carbon).

The distributions of $\chi^2$ probability for free protons in CH$_2$ were obtained by subtracting the spectrum of carbon from that of CH$_2$. Fig. 3.24 (a) and (b) show the distributions of $prob_{\Sigma+}(\chi^2)$ and $prob_{\Sigma-}(\chi^2)$ from free protons, respectively. The events with larger $\chi^2$ probability than 0.1 were retained for the further analysis. The arrows indicate the cut position. Figure 3.24 (c) shows the distribution of $MM(K^+\pi^+\pi^-)$ from free protons in CH$_2$. The solid (dashed) histogram shows the spectrum for events which were selected (rejected) by the cut of $(prob_{\Sigma+}(\chi^2) > 0.1$ or $prob_{\Sigma-}(\chi^2) > 0.1)$. A peak corresponding to the neutron mass is clearly seen for events selected by the cut, while no peak structure is visible in the neutron mass region for the rejected events.
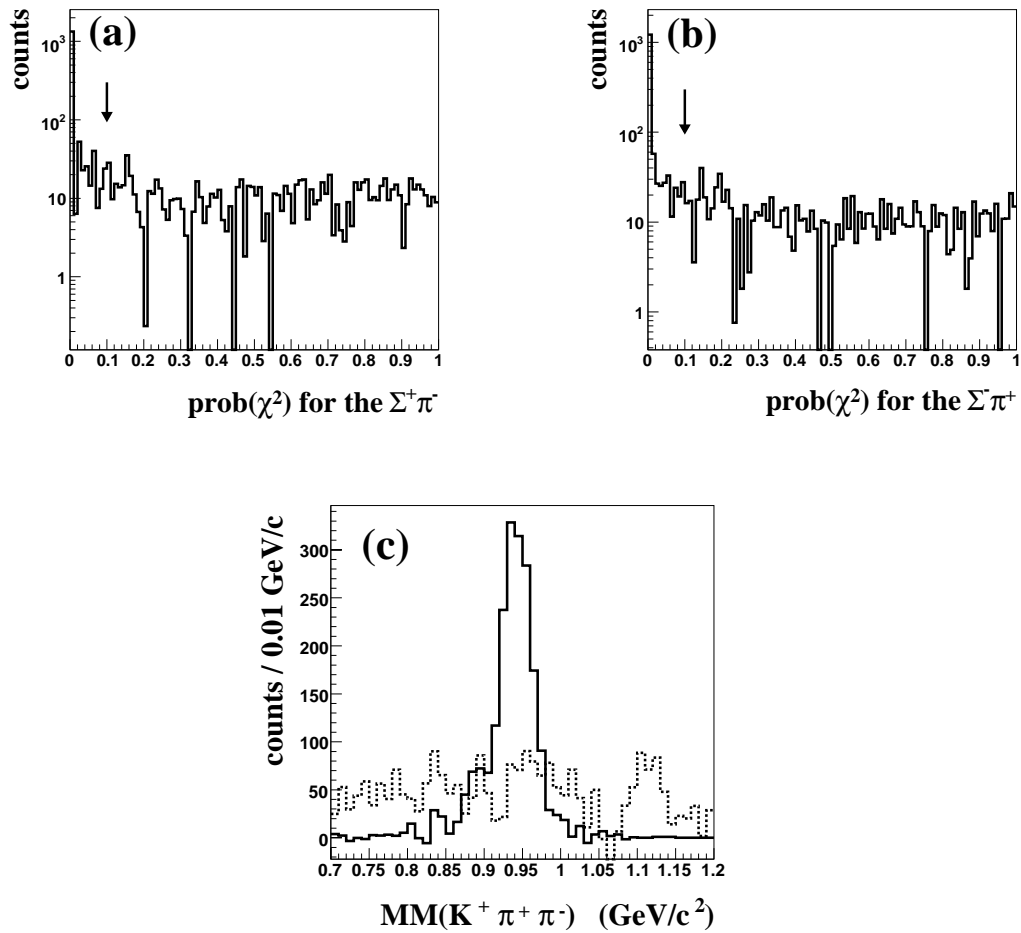


Figure 3.24: (a) and (b) show distributions of $\chi^2$ probability of the kinematic fit with $\Sigma^+\pi^-$ (a) and $\Sigma^-\pi^+$ (b) decay assumption for free protons in the CH$_2$ target. The arrows indicate the cut position. (c) shows $MM(K^+\pi^+\pi^-)$ distribution. The solid (dashed) histogram shows the spectrum for events selected (rejected) by $\chi^2$ probability cut of the kinematic fit.

### 3.4.3   Selection of $\Sigma^+$ or $\Sigma^-$

The decay mode of $\Lambda(1405)$ , $\Sigma^+\pi^-$ or $\Sigma^-\pi^+$, was identified from the $\chi^2$ probability of the kinematic fit. Figure 3.25 shows the correlation of the $\chi^2$ probability of the kinematic fit between the $\Sigma^-\pi^+$ assumption $(prob(\chi^2)_{\Sigma-})$ and $\Sigma^+\pi^-$ assumption $(prob(\chi^2)_{\Sigma+})$ for free protons in CH$_2$ for events which survived the neutron selection cut, the cut of $MM^2(K^+p\pi^-) < -0.05$ (GeV/c$^2$)$^2$ and $(prob_{\Sigma+}(\chi^2) > 0.1$ or $prob_{\Sigma-}(\chi^2) > 0.1$ ). Events with a $(\Sigma^+\pi^-)$ pair should have larger values for the $\chi^2$ probability with the $\Sigma^+\pi^-$ decay assumption than with the $\Sigma^-\pi^+$ decay assumption. As shown in Fig. 3.25, events with large $prob(\chi^2)_{\Sigma+}$ and $prob(\chi^2)_{\Sigma-}$ are mostly exclusive. In this way, we could distinguish the two decay modes using the $\chi^2$ probability of the kinematic fit. The $\Sigma^+\pi^-$ decay events were selected by requiring $prob(\chi^2)_{\Sigma+} > 0.1$ and $prob(\chi^2)_{\Sigma+} > prob(\chi^2)_{\Sigma-}$, whereas the $\Sigma^-\pi^+$ decay events were selected by requiring $prob(\chi^2)_{\Sigma-} > 0.1$ and $prob(\chi^2)_{\Sigma-} > prob(\chi^2)_{\Sigma+}$. The solid line in Fig. 3.25 shows the boundary of the $\Sigma^+/\Sigma^-$ selection cut. The misidentification rate of $\Sigma^+$ and $\Sigma^-$ using the above procedure was estimated to be 12% using the MC simulation.
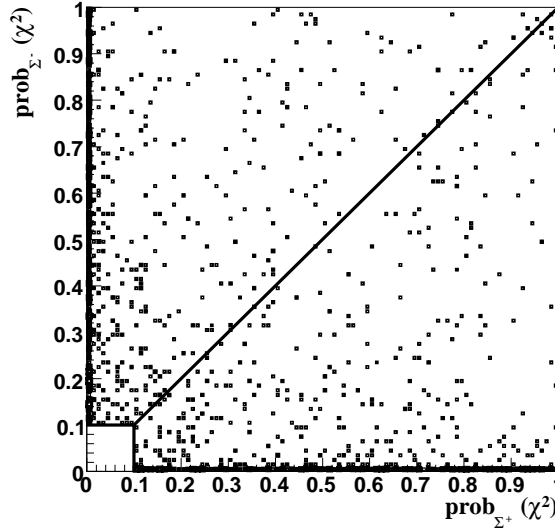


Figure 3.25: Correlation plot of the $\chi^2$ probability of the kinematic fit between the $\Sigma^-\pi^+$ assumption and $\Sigma^+\pi^-$ assumption for free protons in CH$_2$.

The distributions of $MM(K^+\pi^-)$ and $MM(K^+\pi^+)$ are shown in Fig. 3.26 left and right, respectively. The solid histogram in the left (right) plot shows the spectrum for events selected by $\Sigma^+\pi^-$ ($\Sigma^-\pi^+$) selection cut, and the dashed one shows the spectrum for events rejected by this cut. The masses of $\Sigma^+(1189)$ and $\Sigma^-(1197)$ were determined from a Gaussian fit to the data to be $1191\pm1$ MeV/c$^2$ and $1199\pm1$ MeV/c$^2$, respectively in agreement with the PDG values. The measured widths of $\Sigma^+(1189)$ and $\Sigma^-(1197)$ were $20\pm1$ MeV/c$^2$ and $16\pm1$ MeV/c$^2$, respectively, and they are consistent with the expected value of 17 MeV/c$^2$ as estimated by the MC simulation.
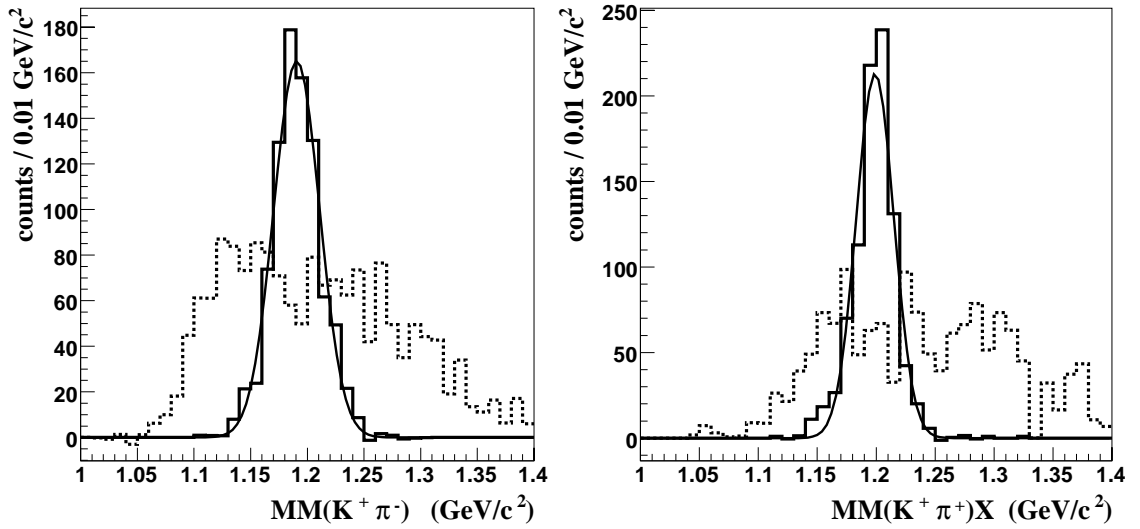
Figure 3.26: Distributions of $MM(K^+\pi^-)$ (left) and $MM(K^+\pi^+)$ (right). The solid histogram in the left (right) plot shows the spectrum for events selected by $\Sigma^+\pi^-$ ($\Sigma^-\pi^+$) selection cut, and the dashed one shows the spectrum for events rejected by the cut.

### 3.4.4   The lineshape of $\Lambda(1405)$

Figure 3.27 shows missing mass spectra for the $\gamma p \rightarrow K^+ X$ reaction for the $(K^+ \Sigma^+ \pi^-)$ final state (a) and $(K^+ \Sigma^- \pi^+)$ final state (b) for events selected by all the cuts described above. The solid histograms show the spectra for $CH_2$ and the dotted histograms show those for carbon. The spectrum for carbon was smoothed by smearing the photon energies with the experimental resolution in order to reduce the effect of statistical fluctuations. The smoothed spectra are shown as dashed histograms.
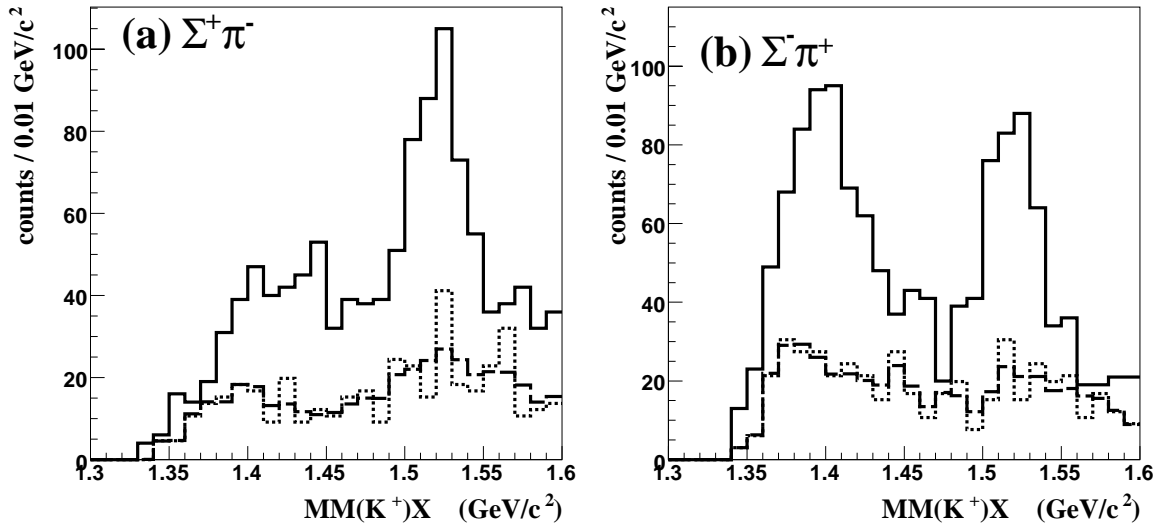


Figure 3.27: Distributions of $MM(K^+)$ for the $(K^+ \Sigma^+ \pi^-)$ final state (left) and for the $(K^+ \Sigma^- \pi^+)$ final state (right). The solid and dotted histograms show spectra for $CH_2$ and carbon, respectively. The dashed histograms show the spectra for carbon after smoothing.

Closed circles in Fig. 3.28 show spectra for free protons in $CH_2$. Open circles show spectra obtained by the previous measurement [14], where the heights of spectra are not normalized. The $\Lambda^*(1520)$ peak visible in these spectra was fitted using a Breit-Wigner function atop the phase space distribution of nonresonant $(K^+ \Sigma \pi)$ production. The solid lines show the fit results. The mass peak positions are $1520 \pm 2$ MeV/$c^2$ in the $\Sigma^+ \pi^-$ decay mode and $1517 \pm 2$ MeV/$c^2$ in the $\Sigma^- \pi^+$ decay mode. Thus, the mass of $\Lambda^*(1520)$ is consistent with the PDG value of 1519.5 MeV/$c^2$ in each decay mode. The peak position of the $\Lambda(1405)$ in $\Sigma^- \pi^+$ mode was consistent with the PDG value of 1406 MeV/$c^2$. However, the peak structure in the $\Sigma^+ \pi^-$ mode was not clear. The decay mode dependence of the lineshapes of $\Lambda(1405)$ is likely due to strong interference between isospin 0 and 1 amplitudes of the $\Sigma\pi$ interaction. The cross sections of the $\Sigma^+ \pi^-$ interaction ($\sigma_{\Sigma^+ \pi^-}$) and $\Sigma^- \pi^+$ interaction ($\sigma_{\Sigma^- \pi^+}$) can be written using the isospin 0 ($T^{(0)}$) and 1 ($T^{(1)}$) component of scattering matrices

as,

$$\sigma_{\Sigma^+\pi^-} = \frac{1}{2}|T^{(1)}|^2 + \frac{1}{3}|T^{(0)}|^2 + \frac{2}{\sqrt{6}}\text{Re}(T^{(0)}T^1)$$

$$\sigma_{\Sigma^-\pi^+} = \frac{1}{2}|T^{(1)}|^2 + \frac{1}{3}|T^{(0)}|^2 - \frac{2}{\sqrt{6}}\text{Re}(T^{(0)}T^1).$$

The coefficients are deduced from the Clebsch-Gordan coefficients. The third term, the interference term of isospin 0 and 1 amplitudes, has different sign in two decay modes, and thus, this term causes the change of the lineshape depending on the decay mode. The apparent difference for the lineshape of the $\Lambda(1405)$ in the $\Sigma^-\pi^+$ decay mode between the current work and the previous measurement will be discussed in Chapter 5.1.
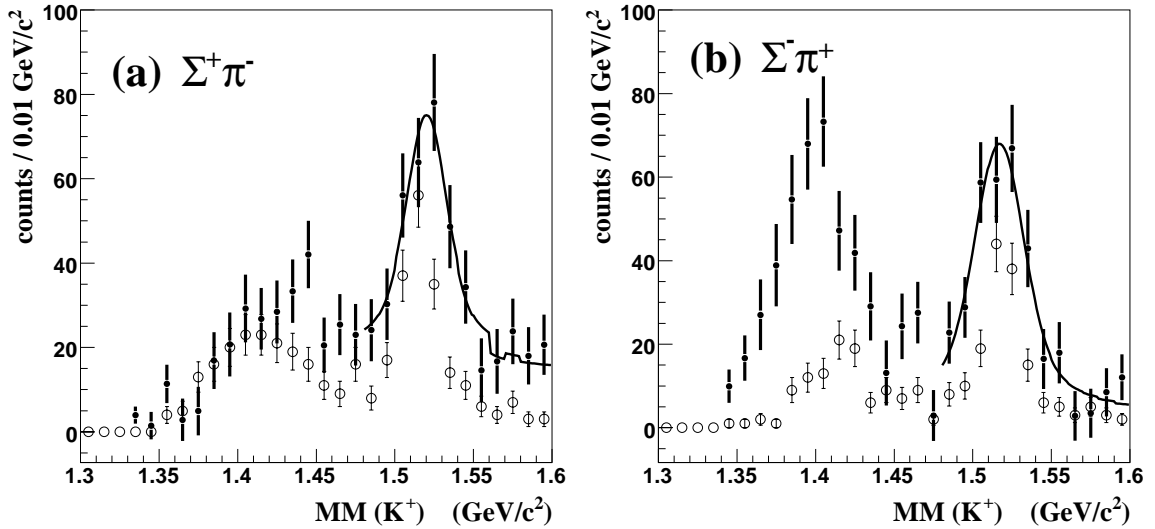


Figure 3.28: Distributions of $MM(K^+)$ for the $(K^+\Sigma^+\pi^-)$ final state (left) and for the $(K^+\Sigma^-\pi^+)$ final state (right). The closed circles show spectra for free protons in $CH_2$. The open circles show spectra obtained by the previous measurement [14].

The isospin interference term is canceled by summing the spectra of the $\Sigma^+\pi^-$ and $\Sigma^-\pi^+$ modes. The summed spectrum was obtained after correcting for the decay branch of $\Sigma^+ \to p\,\pi^0$ ($\sim 52\%$), and the result is shown in Fig. 3.29. Closed and open circles show the spectra measured by this work and by the previous one, respectively, where the normalization for the spectrum by the previous measurement was determined by fitting in the range of $1.34 < MM(K^+) < 1.47$ GeV/c$^2$. The $\chi^2$/ndf was 1.4 in the $\Lambda(1405)$ mass region. Thus, the lineshape of $\Lambda(1405)$ after the sum is consistent with the one from the previous measurement.
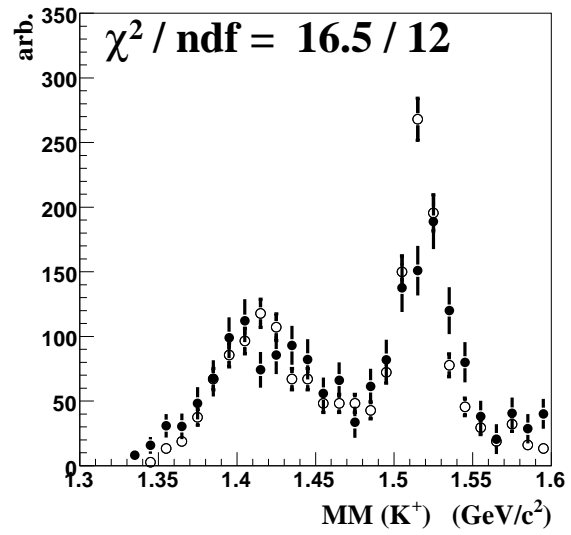
Figure 3.29: Distributions of $MM(K^+)$. The closed and open circles show spectra obtained by this work and by the previous measurement [14].

### 3.4.5 Yield of Λ(1405) production

The yield of Λ(1405) photoproduction was extracted from a peak in the combined spectrum of the $\Sigma^+\pi^-$ decay mode and $\Sigma^-\pi^+$ decay mode in which the isospin interference term is canceled. The yields were obtained in two photon energy regions: $1.5 < E_\gamma < 2.0$ GeV and $2.0 < E_\gamma < 2.4$ GeV. Figure 3.30 shows distributions of $MM(K^+)$ in two photon energy regions. The closed circles show experimental data for free protons in $CH_2$. The contribution from $\Sigma^0(1385)$ production estimated from $\Lambda\pi^0$ decay mode is shown as open circles. The background of $K^0(892)\Sigma^+$ production is measured from a invariant mass spectrum of $(K^+\pi^-)$ pairs, see Appendix E. The threshold of $K^0(892)\Sigma^+$ production is $E_\gamma = 1.9$ GeV, and therefore, the contribution is significant only in the high photon energy region. The estimated contribution is shown as the dot-dashed histogram. The spectra were fitted with the distribution for $K^+\Lambda^*(1405)$, $K^+\Lambda^*(1520)$ and nonresonant $(K^+\Sigma\pi)$ production as determined by the MC simulation, where the spectrum shape of Λ(1405) calculated by Nacher *et al.* was used. The strength of each reaction was obtained by the fitting, with the assumption that the ratio of the yields of nonresonant $(K^+\Sigma\pi)$ production in the two photon energy regions is proportional to the phase volume, as described below. The solid curves show the spectra of Λ(1405) calculated by Nacher *et al.*, and the dashed lines show the distribution for nonresonant $(K^+\Sigma\pi)$ production. The fit results are shown as the solid histograms.
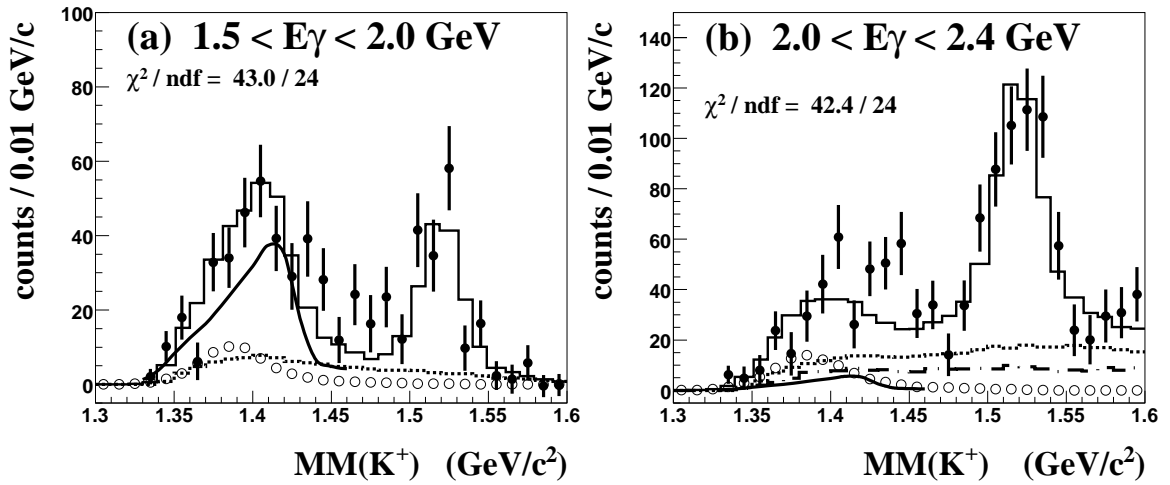


Figure 3.30: Distribution of $MM(K^+)$. The combined spectra of the $\Sigma^+\pi^-$ mode and $\Sigma^-\pi^+$ mode are shown in two photon energy ranges: $1.5 < E_\gamma < 2.0$ GeV (a) and $2.0 < E_\gamma < 2.4$ GeV (b).

The $\chi^2/ndf$ for the fits were 1.7 for both photon energy region. The theoretical spectrum of Nacher *et al.* is seen to be consistent with the experimental data in the

low photon energy region. A second fit was performed using a different theoretical spectrum due to Kaiser *et al.* [54] derived from an effective Lagrangian. The fit results did not change significantly, and this theoretical model is also seen to be consistent with the experimental data, see Appendix F.

Fig. 3.31 (a) shows the phase space distributions of $(K^+\Sigma\pi)$ production for the photon energy of 1.5 GeV (solid line) and 2.4 GeV (dashed line). Fig. 3.31 (b) shows the phase volume as a function of the photon energy. The ratio of the phase volumes for nonresonant $(K^+\Sigma\pi)$ production between the photon energy range of $1.5 < E_\gamma < 2.0$ GeV and $2.0 < E_\gamma < 2.4$ GeV was found to be 0.37, and this ratio was used for the fitting described above after taking into account of the detector acceptance. The yields of $\Lambda(1405)$ were found to be $182 \pm 26$ events and $42 \pm 32$ events for $1.5 < E_\gamma < 2.0$ GeV and $2.0 < E_\gamma < 2.4$ GeV, respectively.
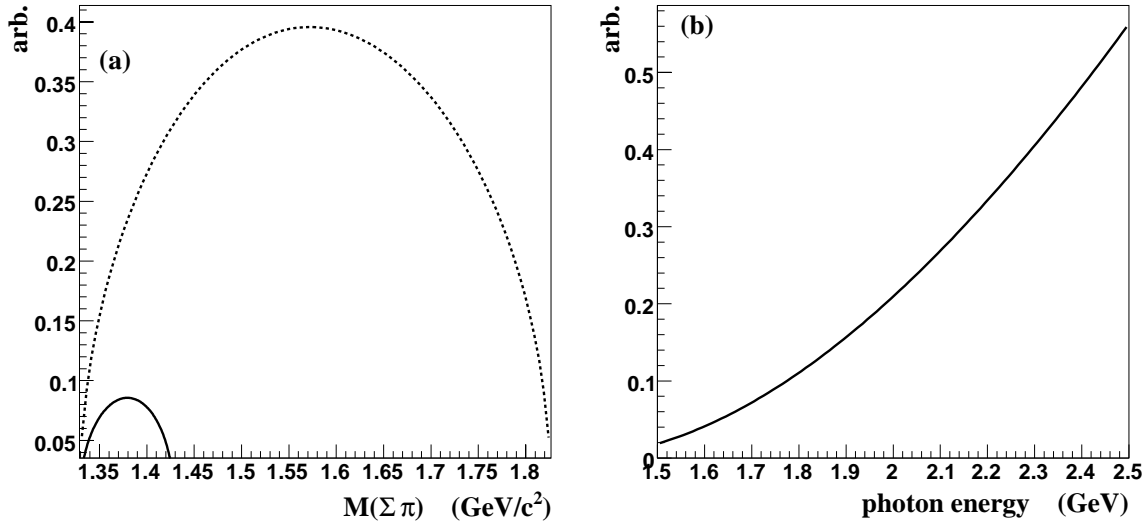


Figure 3.31: Left: Phase space distributions for $(K^+\Sigma\pi)$ production for the photon energies of 1.5 GeV (solid) and 2.4 GeV (dashed). Right: Phase volume as a function of photon energy.

## 3.4.6   Production ratio between $\Lambda(1405)$ and $\Sigma^0(1385)$

The production ratio between $\Sigma^0(1385)$ and $\Lambda(1405)$ was obtained from the yields measured in $\Lambda\pi^0$ mode and in $\Sigma^\pm\pi^\mp$ mode, respectively. The yield of $\Sigma^0(1385)$ was measured in $\Lambda\pi^0$ mode, and the contamination to $\Sigma^\pm\pi^\mp$ mode was estimated using the detector acceptance estimated by the MC simulation assuming flat decay angular distributions, as described in the previous section. The detector acceptances of $\Sigma^\pm\pi^\mp$ decay of $\Lambda(1405)$ were obtained by the MC simulation as 0.12 and 0.15 for $1.5 < E_\gamma < 2.0$ GeV and $2.0 < E_\gamma < 2.4$ GeV, respectively. The ratio of $\Lambda(1405)$

production to $\Sigma^0(1385)$ production was found to be $0.54 \pm 0.17$ and $0.074 \pm 0.076$ for $1.5 < E_\gamma < 2.0$ GeV and $2.0 < E_\gamma < 2.4$ GeV, respectively. The numbers used for the measurement of the production ratio are summarized in Table 3.6.

Table 3.6: Summary of the production ratio between $\Lambda(1405)$ and $\Sigma^0(1385)$ .

| | number of events in $1.5 < E_\gamma < 2.0$ GeV | number of events in $2.0 < E_\gamma < 2.4$ GeV |
|---|---|---|
| acceptance corrected yield of $\Sigma^*(1385)$ | $4.1 \pm 1.1 \times 10^3$ | $5.8 \pm 1.4 \times 10^3$ |
| yield of $\Lambda(1405)$ in $\Sigma^\pm \pi^\mp$ mode | $182 \pm 26$ | $42 \pm 32$ |
| acceptance of $\Lambda^*(1405) \to \Sigma^\pm \pi^\mp$ | $0.12$ | $0.15$ |
| acceptance corrected yield of $\Lambda^*(1405)$ | $2.2 \pm 0.33 \times 10^3$ | $0.43 \pm 0.33 \times 10^3$ |
| ratio of $\Lambda^*/\Sigma^*$ | $0.54 \pm 0.17$ | $0.074 \pm 0.076$ |

# Chapter 4

# Differential cross section

## 4.1 Measurement of the differential cross section using liquid hydrogen data

The absolute value of the differential cross section was extracted from the peak in the missing mass of the $\gamma p \rightarrow K^+ X$ reaction measured in data which were taken previously at SPring-8/LEPS using the liquid hydrogen target (data set (I)). In this data set, the only $K^+$'s from the $\gamma p \rightarrow K^+ X$ reaction were detected at the LEPS spectrometer. Because of the small mass difference between $\Sigma^0(1385)$ and $\Lambda(1405)$, these hyperon resonances cannot be separated in the $MM(K^+)$ distribution. In order to separate these two hyperons, the production ratio of $\Lambda(1405)$ to $\Sigma^0(1385)$ obtained from the data set (II) as described in the previous chapter was used in the common detector acceptance of these two data sets. The $K^+$ selection criteria for the measurement of the $\gamma p \rightarrow K^+ X$ reaction were same as those for the analysis of the measurement of the production ratio described in Chapter 3.1 except for the selection of reaction vertex at the target. The liquid hydrogen target was placed about 1 m downstream along the beam axis from the nuclear target used for the data set (II). Accordingly, the angular coverage of the LEPS spectrometer for the $K^+$'s produced from the liquid hydrogen target in the data set (I) is larger than that produced from the nuclear target in the data set (II). In order to match the acceptance between two data sets, the polar angle of a $K^+$ in the center-of-mass system, $\Theta_{K_{CM}}$, is required to be $\cos(\Theta_{K_{CM}}) > 0.8$.

Fig 4.1 (a) shows a distribution of the missing mass of the $\gamma p \to K^+ X$ reaction from the liquid hydrogen target. The peaks corresponding to hyperons, $\Lambda(1116)$, $\Sigma^0(1192)$, $\Lambda(1405)/\Sigma(1385)$ and $\Lambda(1520)$, are clearly seen.
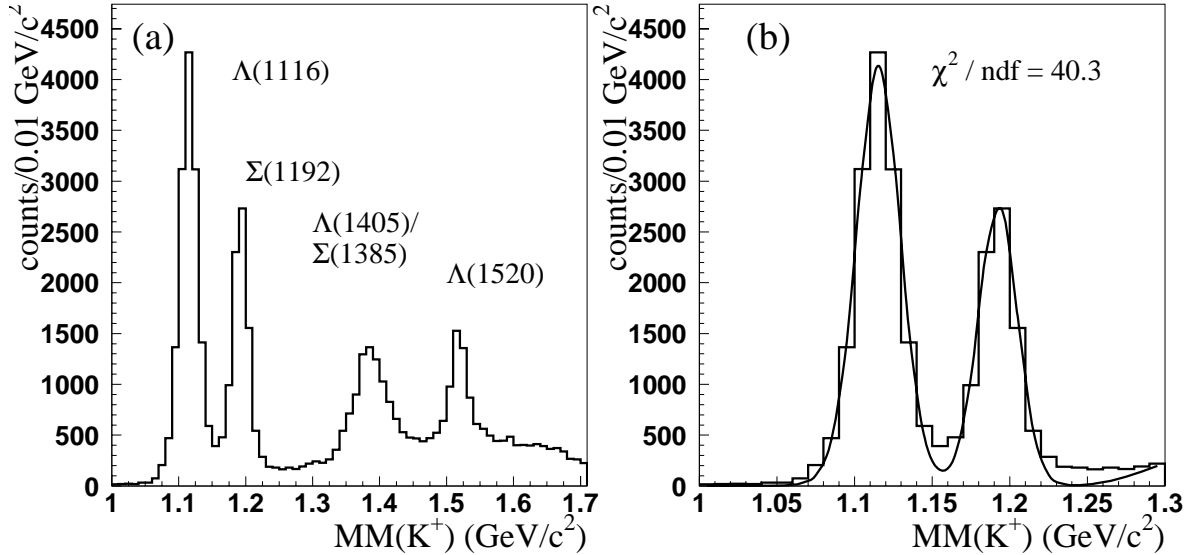


Figure 4.1: Distribution of $MM(K^+)$ for the liquid hydrogen target. Peaks corresponding to hyperons can be seen in (a). Plot (b) shows spectra around the $\Lambda(1116)$ and $\Sigma(1192)$ mass region.

Fig 4.1 (b) shows a missing mass spectrum around the $\Lambda(1116)$ and $\Sigma(1192)$ mass region. The spectrum was fitted with the expected spectra of $\Lambda(1116)$, $\Sigma(1192)$ and $(K^+\Lambda(1116)\pi^0)$ production generated by the MC simulation. The fit result is shown as the solid line. The MC simulation could not reproduce the experimental spectrum around 1.15 GeV/c$^2$ and 1.24 GeV/c$^2$. The inconsistency around 1.24 GeV/c$^2$ region affects on the estimation of the strength of $(K^+\Lambda\pi^0)$ production and the extraction of the yield of $\Sigma^0(1385)$ and $\Lambda(1405)$ production. The contribution of $\Sigma(1192)$ production is small enough at 1.24 GeV/c$^2$ and no other hyperon production reaction is possible bellow the $(K^+\Lambda\pi^0)$ production threshold, 1.25 GeV/c$^2$, thus, this background must be due to events in which the photon energy or the momentum of a $K^+$ were not obtained correctly, or near threshold enhancement of $(K^+\Lambda\pi^0)$ production. The solid and dashed histograms in Fig. 4.2 show the distributions of photon energies for events in the background region, $1.22 < MM(K^+) < 1.27$ GeV/c$^2$, and in the $\Sigma^0(1192)$ mass region, $1.17 < MM(K^+) < 1.22$ GeV/c$^2$, respectively. The height of the distribution in the $\Sigma^0(1192)$ mass region was normalized to that in the background region around 2.0 GeV. The distribution in the background region shows the enhancement in the low photon energy region, $1.5 < E_\gamma < 1.7$ GeV. These

events were produced by the recoiled electrons which hit the wall of the chamber of the tagging counter. The recoiled electron which corresponds to the $\sim 1.3$ GeV photon hit the chamber of the tagging counter and produces an electromagnetic shower in the thick material of the chamber wall. The $e^+e^-$ pairs hit the scintillating fibers of the tagging counter around $1.5 < E_\gamma < 1.7$ GeV region. Thus, the photon energy is misidentified to be higher than true value, and the $MM(K^+)$ distributes in higher mass side of the true mass.
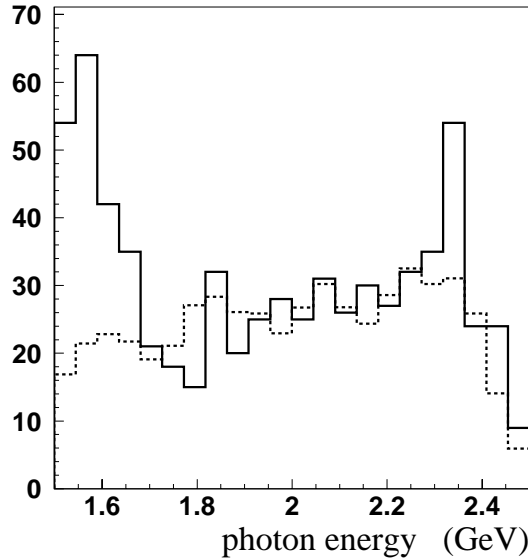


Figure 4.2: Photon energy distribution for events in the $\Sigma^0(1192)$ mass region (dashed histogram) and the background region (solid histogram). The height of the distribution in the $\Sigma^0(1192)$ mass region was normalized to that of the background region around $E_\gamma \sim 2.0$ GeV.

Some of background events in $1.22 < MM(K^+) < 1.27$ GeV/c$^2$ region were caused by this electromagnetic shower in the tagging counter. However, all of events cannot be explained by this shower event since there are events which show the spectrum of the Compton scattering. Since these background events could not be reproduced by the known physics processes, a linear function was employed to estimate the effect to the measurement of the cross section.

Figure 4.3 shows the distribution of $MM(K^+)$ around $\Sigma^0(1385)$ and $\Lambda(1405)$ mass region for the liquid hydrogen target in two photon energy bins: $1.5 < E_\gamma < 2.0$ GeV (a) and $2.0 < E_\gamma < 2.4$ GeV (b).
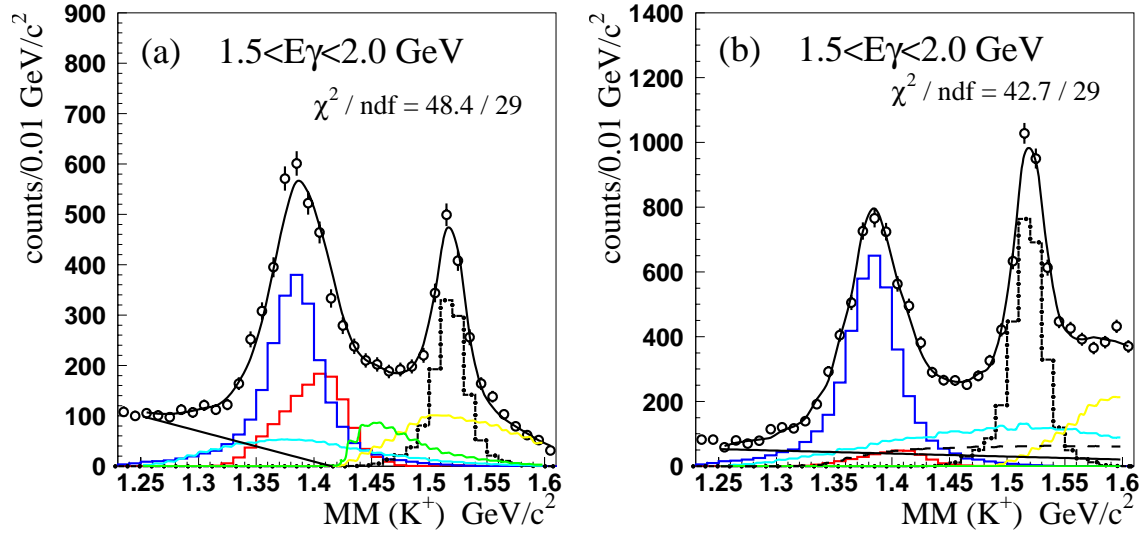
Figure 4.3: Distribution of $MM(K^+)$ around $\Sigma^0(1385)$ and $\Lambda(1405)$ mass region for the liquid hydrogen target for the photon energy range of $1.5 < E_\gamma < 2.0$ GeV (a) and $2.0 < E_\gamma < 2.4$ GeV (b). The solid curves show the fit result using the MC spectra of $\Sigma^0(1385)$ (blue), $\Lambda(1405)$ (red), $\Lambda(1520)$ (dot-dashed), $\phi$-meson (yellow), $(K^+K^-p)$ (green) and the sum of the phase space distribution of $(K^+\Lambda\pi^0)$ and $(K^+\Sigma\pi)$ production (light blue). The additional background contributions which could not be reproduced by the sum of the known physics processes are fitted with a linear function and indicated by the straight lines.

The production ratio of $\Lambda(1405)$ to $\Sigma^0(1385)$ used for fitting was 0.54 and 0.08 for $1.5 < E_\gamma < 2.0$ GeV and $2.0 < E_\gamma < 2.4$ GeV, respectively, as obtained in the previous chapter. Open circles show experimental data. The solid curve shows fit result. The blue, red and dot-dashed histograms show spectra of hyperon resonances, $\Sigma^0(1385)$, $\Lambda(1405)$ and $\Lambda^*(1520)$, respectively. The spectra of background reactions of $K^*(892)\Sigma^+$ and $\phi$-meson production are shown as the dashed and yellow histograms, respectively. The phase space distribution of nonresonant $(K^+\Lambda\pi^0)$ and $(K^+\Sigma\pi)$ production is similar to each other, and thus, the combined spectrum of these two reactions is shown by the light blue line. The phase space distributions of nonresonant $(K^+K^-p)$ production are shown as the green histogram. The background contributions which could not be reproduced by the sum of the known physics processes are fitted with a linear function and indicated by the straight lines. The main systematic uncertainties for the yield of the $\Sigma^0(1385)$ and $\Lambda(1405)$ due to this background were estimated to be $^{+1.0}_{-27}\%$ and $^{+8.1}_{-0.94}\%$ for $1.5 < E_\gamma < 2.0$ GeV and $2.0 < E_\gamma < 2.4$ GeV, respectively, by fitting with various slope parameters of the linear background and without the linear background. The other sources of systematic uncertainties are summarized in Table 4.1.

The differential cross sections of $\Sigma^0(1385)$ production were found to be $d\sigma/d(\cos\theta) = 0.80\pm0.092(stat.)^{+0.062}_{-0.27}(syst.)$ $\mu$b for $1.5 < E_\gamma < 2.0$ GeV and $0.87\pm0.064(stat.)^{+0.13}_{-0.067}(syst.)$ $\mu$b for $2.0 < E_\gamma < 2.4$ GeV. That of $\Lambda(1405)$ production was obtained as $d\sigma/d(\cos\theta) = 0.43 \pm 0.088(stat.)^{+0.034}_{-0.14}(syst.)$ for $1.5 < E_\gamma < 2.0$ GeV. The production cross section in higher photon energy region could not be measured accurately, but an upper limit of 95% confidence level was extracted as $d\sigma/d(\cos\theta) < 0.094 + 1.64 \times \sqrt{0.054^2 + 0.025^2} = 0.19$ $\mu$b.

Table 4.1: Systematic uncertainties for the measurement of differential cross sections.

| The sources of uncertainties | $1.5 < E_\gamma < 2.0$ GeV | $2.0 < E_\gamma < 2.4$ GeV |
|---|---|---|
| Background around $(K^+\Lambda\pi)$ threshold | $^{+1.0}_{-27}$ % | $^{+8.1}_{-0.94}$ % |
| | $1.5 < E_\gamma < 2.4$ GeV | |
| Thickness of the liquid hydrogen target | | 1.0 % |
| Number of photons | | 1.2 % |
| Photon transmission efficiency | | 3.0 % |
| Accidental veto by | | |
| the aerogel Čerenkov counter | | 1.6 % |

## 4.2  Normalization of the invariant mass spectrum of $\Lambda(1405)$

In order to compare the strength of the $\Lambda(1405)$ in two photon energy bins, the mass spectrum obtained in Section 3.4.5 was normalized using the $K^+\Lambda(1116)$ production measured in the data set (I) and (II). The integrated luminosity is defined as the product of the number of target protons, $N_T$, and the total number of photons at the target, $N_{eff\gamma}$. The integrated luminosity for the data set (II) was obtained using the differential cross section of $\Lambda(1116)$ production measured from the data set (I) and the yield of $\Lambda(1116)$ measured from the data set (II). The differential cross section of $\Lambda(1116)$ can be written in terms of the yield, the acceptance, $A_{\Lambda(1116)}$, and the integrated luminosity as follows,

$$\frac{d\sigma}{d(\cos\theta)}\left[\Lambda(1116)\right] \;=\; Y_{\Lambda(1116)}/(A_{\Lambda(1116)} \cdot N_T \cdot N_{eff\gamma}).$$

The differential cross sections of $\Lambda(1116)$ production in the angular range of kaon of $\cos(\Theta_{K_{CM}}) > 0.8$ measured from the data set (I) were $2.0\pm0.04$ $\mu$b and $1.7\pm0.03$ $\mu$b in $1.5 < E_\gamma < 2.0$ GeV and $2.0 < E_\gamma < 2.4$ GeV, respectively. The yields of $\Lambda(1116)$ in the data set (II) were extracted from peaks in the missing mass of the $\gamma p \rightarrow K^+ X$ reaction for events with a $\Lambda$ detected in the TPC. Fig. 4.4 shows distributions of $MM(K^+)$ for events which survived the $\Lambda$ selection cut for free protons in $CH_2$.
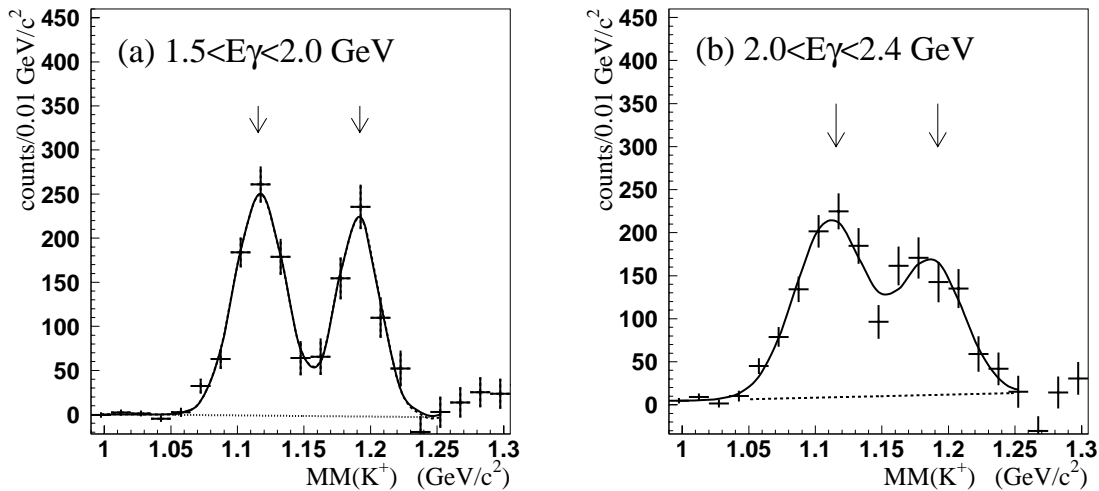


Figure 4.4: Distributions of $MM(K^+)$ for events with a $\Lambda$ detected in the TPC for free protons in $CH_2$ measured from the data set (II).

The yields of $\Lambda(1116)$ were obtained by fitting a Gaussian to the data with a linear background and found to be $799 \pm 76$ events and $911 \pm 98$ events for $1.5 < E_\gamma < 2.0$ GeV and $2.0 < E_\gamma < 2.4$ GeV, respectively. The acceptance for the detection of $K^+\Lambda(1116)$ production events in the range of $0.8 < \cos(\Theta_{K_{CM}}) < 1.0$ was obtained from the MC simulation to be 0.067 for $1.5 < E_\gamma < 2.0$ GeV and 0.075 for $2.0 < E_\gamma < 2.4$ GeV. The integrated luminosity was obtained as $6.0 \times 10^3$ $\mu$b$^{-1}$ for $1.5 < E_\gamma < 2.0$ GeV and $7.1 \times 10^3$ $\mu$b$^{-1}$ for $2.0 < E_\gamma < 2.4$ GeV.

The detector acceptance of $(K^+\Sigma^\pm\pi^\mp)$ production as a function of the invariant mass of $(\Sigma\pi)$ pairs was obtained from the MC simulation. The combined spectra of the $\Sigma^+\pi^-$ and $\Sigma^-\pi^+$ mode in Fig. 3.30 were corrected using the detector acceptance and divided by the integrated luminosity described above. Closed circles in Fig. 4.5 show the corrected spectra of $MM(K^+)$ for $0.8 < \cos(\Theta_{K_{CM}}) < 1.0$ and in two photon energy ranges: $1.5 < E_\gamma < 2.0$ GeV (a) and $2.0 < E_\gamma < 2.4$ GeV (b).
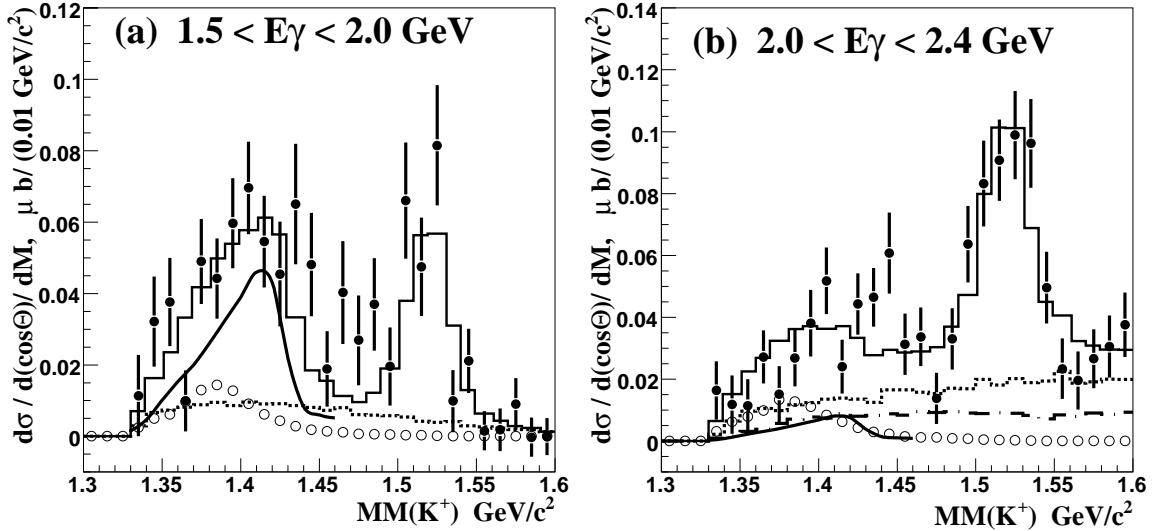


Figure 4.5: Closed circles show combined spectra of $MM(K^+)$ of $\Sigma^+\pi^-$ mode and $\Sigma^-\pi^+$ mode, after correcting for the detector acceptance and the integrated luminosity in two photon energy ranges: $1.5 < E_\gamma < 2.0$ GeV (a) and $2.0 < E_\gamma < 2.4$ GeV (b).

Open circles show the contamination of the $\Sigma^0(1385)$ estimated from the $\Lambda\pi^0$ decay mode. The background of $K^0(892)\Sigma^+$ is shown as the dot-dashed histogram in Fig. 4.5 (b). The solid curves show the spectra of $\Lambda(1405)$ calculated by Nacher *et al.*, and the dashed lines show the phase space distribution for nonresonant $(K^+\Sigma\pi)$ production. The solid histograms show the sum of all contributions including $\Lambda(1405)$, $\Sigma^0(1385)$, nonresonant $(K^+\Sigma\pi)$, $K^0(892)\Sigma^+$ and $\Lambda(1520)$ production.

In order to confirm the validity of the normalization, the production cross sec-

tion of $\Lambda(1520)$ is compared between two data sets. The cross sections of $\Lambda(1520)$ production in the charged $\Sigma\pi$ mode were obtained by fitting the MC spectra to the data as shown as solid histograms in Fig. 4.5, and were found to be $0.21 \pm 0.03$ $\mu$b and $0.31 \pm 0.04$ $\mu$b for $1.5 < E_\gamma < 2.0$ GeV and $2.0 < E_\gamma < 2.4$ GeV, respectively. After taking into account of the decay branch of $\Lambda(1520)$ into $\Sigma\pi$ mode, 0.42, and the ratio of the charged $\Sigma\pi$ mode to all $\Sigma\pi$ mode, 2/3, the production cross sections were found to be $0.75 \pm 0.11$ $\mu$b and $1.1 \pm 0.14$ $\mu$b for $1.5 < E_\gamma < 2.0$ GeV and $2.0 < E_\gamma < 2.4$ GeV, respectively. On the other hand, the cross sections measured from the data set (I) were $0.81 \pm 0.05$ $\mu$b and $0.74 \pm 0.02$ $\mu$b for $1.5 < E_\gamma < 2.0$ GeV and $2.0 < E_\gamma < 2.4$ GeV, respectively. These are consistent within the statistical errors, and thus, the normalization factor is found reliable.

In the high photon energy region, the lineshape of $\Lambda(1405)$ is unclear, and the yield of $\Lambda(1405)$ extracted by fitting depends on the estimation of the background reaction. To obtain a more conservative estimate, the integral of the invariant mass distribution was considered. First, the strength in the range of $1.33 < MM(K^+) < 1.44$ GeV/c$^2$, including $\Lambda(1405)$, $\Sigma^0(1385)$ and all background reactions, was compared in two photon energy bins. The ratios of this combined strength to $\Sigma^0(1385)$ production were $0.80 \pm 0.23$ and $0.50 \pm 0.14$ for $1.5 < E_\gamma < 2.0$ GeV and $2.0 < E_\gamma < 2.4$ GeV, respectively. The production cross section for $\Sigma^0(1385)$ slightly increases in the higher photon energy region, and the contributions of the $(K^+\Sigma\pi)$ and $(K^{*0}\Sigma^+)$ production also increase for higher photon energy as the phase volume increases. Therefore, even in the conservative estimation, the cross section of $\Lambda(1405)$ production should decrease remarkably. Next, in order to estimate the cross section of $\Lambda(1405)$ production, we subtracted the contamination of $\Sigma^0(1385)$ and $K^{*0}$ production. Although the amplitude of $\Lambda(1405)$ production can interfere with these background amplitudes, we subtracted the square of $\Sigma^0(1385)$ and $K^*$ production amplitudes because a theoretical model calculation of such an interference term is not available. However, we note that the contribution of $\Sigma^0(1385)$ is not negligible even in the lower photon energy region, and a theoretical study of the interference with the p-wave amplitude is necessary. The ratios of the sum of $\Lambda(1405)$ and non-resonant $(K^+\Sigma\pi)$ production to $\Sigma^0(1385)$ production were $0.65 \pm 0.19$ and $0.35 \pm 0.12$ for $1.5 < E_\gamma < 2.0$ GeV and $2.0 < E_\gamma < 2.4$ GeV, respectively. Thus, the production of $\Lambda(1405)$ relative to $\Sigma^0(1385)$ is seen to decrease in the higher photon energy region even without any specific knowledge of the nonresonant $(K^+\Sigma\pi)$ contribution.

# Chapter 5

# Discussion

## 5.1  Lineshape of $\Lambda(1405)$

In this section, the lineshapes of $\Lambda(1405)$ measured by this work and by the previous measurement [14] are discussed. In Fig. 5.1, the distributions of $MM(K^+)$ for the $(K^+\Sigma^+\pi^-)$ final state (left) and the $(K^+\Sigma^-\pi^+)$ final state (right) in $1.5 < E_\gamma < 2.4$ GeV are shown again.
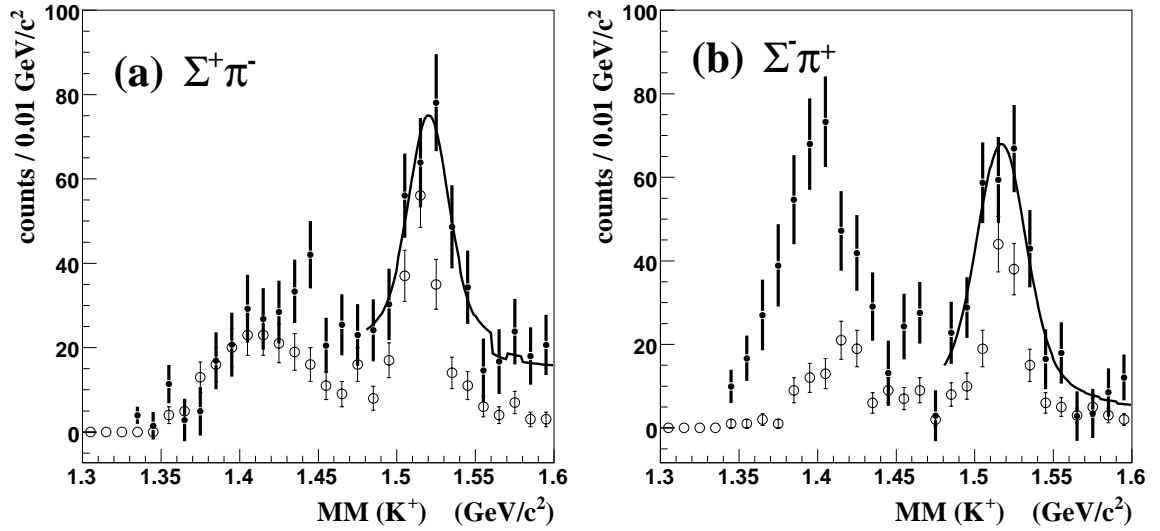


Figure 5.1: Distribution of $MM(K^+)$ for the $(K^+\Sigma^+\pi^-)$ final state (left) and for $(K^+\Sigma^-\pi^+)$ final state (right). The closed circles show spectra for free protons in $CH_2$. The open circles show spectra obtained by the previous measurement [14].

The observed mass spectra of $\Lambda(1405)$ in $\Sigma^+\pi^-$ mode and in $\Sigma^-\pi^+$ mode shown in Fig. 5.1 are quite different, which is understood to be due to the interference

between the isospin 0 and 1 amplitudes, as discussed in Chapter 3.4.4. In addition, the lineshapes of $\Lambda(1405)$ in the $\Sigma^-\pi^+$ decay mode measured by this work and by the previous work are different with each other as shown by the closed and open circles in Fig. 5.1 (b). The photon energy and the scattering angle of the $K^+$ were the same in these two measurements. However, the range of polar angles for the pion with respect to the momentum vector of the $\Lambda(1405)$ was quite different. Fig. 5.2 shows a schematic view of the direction of the $K^+$ and the pion from the decay of $\Lambda(1405)$ in the previous measurement (a) and in this work (b).
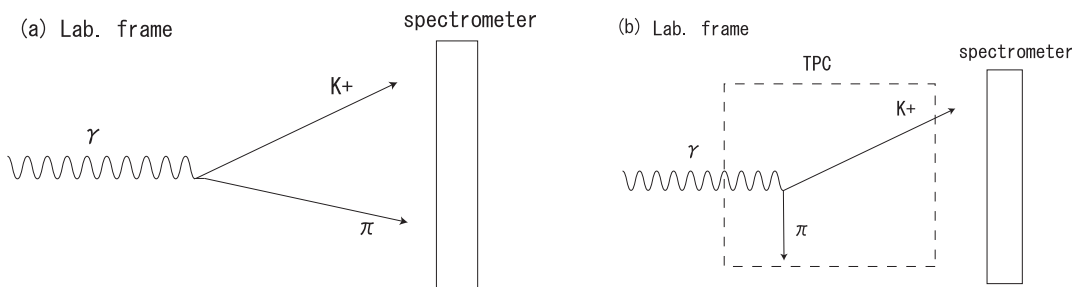


Figure 5.2: Schematic view of the direction of a $K^+$ and a pion from the decay of the $\Lambda(1405)$ in the previous measurement (a) and in this work (b).

In the previous measurement, both a $K^+$ and a charged pion were detected in the LEPS spectrometer. The direction of the $\Lambda(1405)$ is opposite to that of the $K^+$ in the center-of-mass frame, and thus, the direction of the pion relative to the $\Lambda(1405)$, $\Theta_{\pi\Lambda^*}$, is near 180 degrees. Fig. 5.3 (left) shows a distribution of the angle of a pion with respect to the $\Lambda(1405)$ momentum direction generated by the MC simulation.
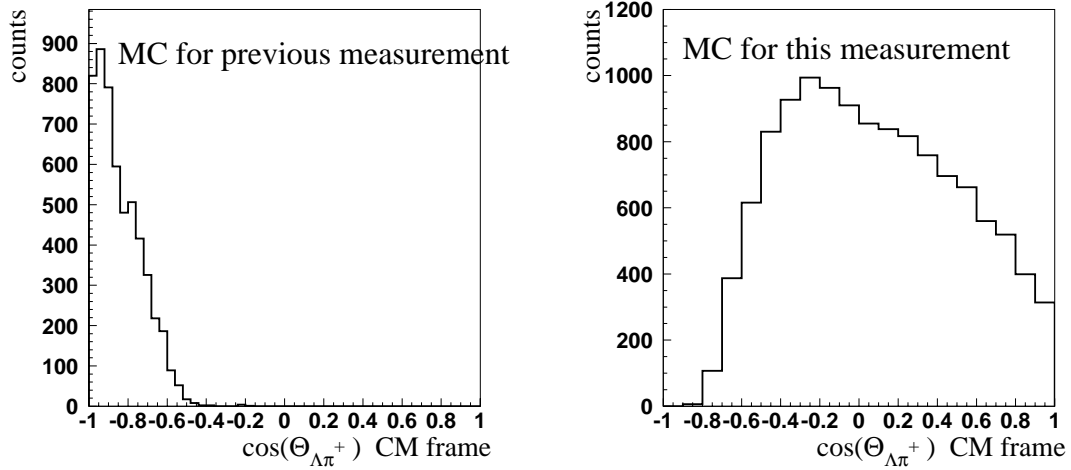
Figure 5.3: Distributions of the angle of a pion with respect to the $\Lambda(1405)$ momentum direction from the MC simulation for the previous measurement (left) and for this work (right).

According to the MC simulation, 99% of events fall in the range of $\cos(\Theta_{\pi\Lambda^*}) < -0.5$ for the previous measurement. In this work, a $K^+$ was detected in the LEPS spectrometer and charged pions were measured in the TPC, which covers the side of the target and can access the entire range of $\Theta_{\pi\Lambda^*}$. Thus, $\Theta_{\pi\Lambda^*}$ distributed over a much wider range than in the previous measurement. Therefore, the difference of the lineshapes between the two measurements might be explained by the angular dependence of the interference term of the $\Sigma\pi$ scattering amplitudes. Because the spin parity of the $\Lambda(1405)$ is $\frac{1}{2}^-$, $(\Sigma\pi)$ pairs are produced in s-wave, and therefore, such an angular dependence does not appear only from the decay of $\Lambda(1405)$. However, the contribution from $\Sigma^0(1385)$, which has the spin parity of $\frac{3}{2}^+$, is not negligible even in the photon energy of just above the production threshold. Thus, this angular dependence is likely due to the interference with the $\Sigma^0(1385)$ production amplitude and the nonresonant $(K^+\Sigma\pi)$ amplitude.

## 5.2 Production ratio of $\Lambda(1405)$ to $\Sigma^0(1385)$

The production ratios of $\Lambda(1405)$ to $\Sigma^0(1385)$ and the differential cross sections for the photoproduction of these hyperon resonances were obtained in two photon energy regions, $1.5 < E_\gamma < 2.0$ GeV and $2.0 < E_\gamma < 2.4$ GeV and in the range of the $K^+$ polar angles of $0.8 < \cos\Theta_{K_{CM}} < 1.0$. The production ratios of $\Lambda(1405)$ to $\Sigma^0(1385)$ were obtained as $\Lambda^*/\Sigma^* = 0.54 \pm 0.17$ and $0.074 \pm 0.076$ for $1.5 < E_\gamma < 2.0$ GeV and $2.0 < E_\gamma < 2.4$ GeV, respectively. The production of $\Lambda(1405)$ decreases in the higher photon energy region with respect to that of $\Sigma^0(1385)$. Because $K^+$'s were detected at the forward angles, the $t$-channel $K^-$ or $K^{*-}$ meson exchange process

was expected to contribute to the production of the $\Sigma^0(1385)$ and $\Lambda(1405)$. In the $t$-channel process, the form factor of the hyperon resonances is an important parameter to describe the production cross section. In general, the production cross section for a particle with a large form factor shows a steep momentum transfer ($t$) dependence. In order to gauge the effect of the form factor of $\Lambda(1405)$, the momentum transfer was calculated in each photon energy region. The four momentum transfer, $t$, was in the range of $-0.45 < t < -0.12$ (GeV)$^2$ for photon energy of $1.5 < E_\gamma < 2.0$ GeV and $-0.37 < t < -0.08$ (GeV)$^2$ for $2.0 < E_\gamma < 2.4$ GeV. The momentum transfer in the two photon energy bins is similar, so our measurement is not sensitive to the $t$ dependence of the $\Lambda(1405)$ cross section. Thus, the reduction of $\Lambda(1405)$ production is not simply related to the $t$-dependence of the production cross section and the form factor. Recently, Nam $et$ $al.$ calculated the cross section of the $\Lambda(1405)$ photoproduction using the effective Lagrangian [55]. They obtained the total cross section of $0.1 \sim 0.2$ $\mu$b near the threshold. In their calculation the cross section starts to decrease beyond $E_\gamma \sim 1.6$ GeV, and they suggested that the production mechanism of the $\Lambda(1405)$ is dominated by the $s$-channel contribution. The measured differential cross section by this experiment was $\sim 0.4$ $\mu$b in $1.5 < E_\gamma < 2.0$ GeV and $0.8 < \cos\Theta_{K_{CM}} < 1.0$. The calculated production cross section by Nam $et$ $al.$ is smaller than the experimental data. However, the tendency of the photon energy dependence is similar to the experimental data. Jido and En'yo proposed a $K\bar{K}N$ molecule which is strongly coupled with the $K\Lambda(1405)$, $a_0(980)N$ and $f_0(980)N$ states [56]. The mass of this molecular state was predicted to be $20 \sim 40$ MeV/c$^2$ below the $K\bar{K}N$ threshold, 1930 MeV/c$^2$, and the predicted width was $90 \sim 100$ MeV/c$^2$. If we assume that this molecular state is produced by the $\gamma p$ reaction, the corresponding photon energy is $1.43 \sim 1.48$ GeV. By taking into account of the width of $90 \sim 100$ MeV/c$^2$, this molecular state can contribute to the threshold enhancement of the $\Lambda(1405)$ photoproduction. However, the statistics of the experimental data are not sufficient to determine the photon energy dependence of the production cross section precisely, and we need more experimental data to investigate the existence of this molecular state.

The observed differential cross sections of $\Sigma^0(1385)$ photoproduction of $d\sigma/d(\cos(\Theta)) \sim 0.8$ $\mu$b in the two photon energy bins are consistent with the effective Lagrangian calculation of Oh $et$ $al.$ [47] (0.6-1.1 $\mu$b).

# Chapter 6

# Conclusion

A hyperon photoproduction experiment was carried out to measure the lineshape of $\Lambda(1405)$ and the differential cross sections of $\Lambda(1405)$ and $\Sigma^0(1385)$ photoproduction. The experiment was performed at the backward Compton $\gamma$-ray beamline in the SPring-8 facility (SPring-8/LEPS). The data were collected using two different experimental setups. The first data set was collected with a liquid hydrogen target and the LEPS spectrometer. A combined spectrum of $\Sigma^0(1385)$ and $\Lambda(1405)$ was observed in the missing mass of the $\gamma p \rightarrow K^+ X$ reaction, $MM(K^+)$, from this data set. In order to distinguish these two hyperons, a time projection chamber (TPC) was constructed for the second data set together with the LEPS spectrometer to facilitate the detection of the decay products of these hyperon resonances. Using this data set, the production ratio between $\Sigma^0(1385)$ and $\Lambda(1405)$ was obtained from the yields of $\Sigma^0(1385)$ and $\Lambda(1405)$ measured from their $\Lambda \pi^0$ and $\Sigma^\pm \pi^\mp$ decay modes, respectively. The absolute values of the differential cross sections were then obtained from the $MM(K^+)$ distribution measured in the first data set.

The peak of $\Sigma^0(1385)$ was clearly observed in the missing mass of the $\gamma p \rightarrow K^+ X$ reaction for events in which a $\Lambda$ hyperon was detected by the TPC. On the other hand, the lineshape of the $\Lambda(1405)$ was obtained by identifying the $\Sigma^+$ and $\Sigma^-$ in the missing mass of the $\gamma p \rightarrow K^+ \pi^- X$ reaction and $\gamma p \rightarrow K^+ \pi^+ X$ reaction, respectively. The lineshapes of the $\Lambda(1405)$ in $\Sigma^+ \pi^-$ and $\Sigma^- \pi^+$ mode were distinct, which indicates strong interference between isospin 0 and 1 amplitudes. The shape of the summed spectrum of the $\Sigma^+ \pi^-$ and $\Sigma^- \pi^+$ modes, in which the interference term was canceled, was consistent with the theoretical calculation by Nacher $et\ al.$ [10] and Kaiser $et\ al.$ [54]. The lineshapes of the $\Lambda(1405)$ in $\Sigma^- \pi^+$ mode obtained by the previous measurement [14] and by this measurement were quite different. The photon energy and the scattering angles of $K^+$'s are consistent between these two measurements, and the difference is only in the angle between $K^+$ and pion from the decay of $\Lambda(1405)$. Thus the difference of the lineshape is likely due to the angular dependence of the isospin interference term.

The production ratios of $\Lambda(1405)$ to $\Sigma^0(1385)$ were determined to be $0.54 \pm 0.17$ and $0.074 \pm 0.076$ for $1.5 < E_\gamma < 2.0$ GeV and $2.0 < E_\gamma < 2.4$ GeV, respectively.

The ratio decreases in the higher photon energy region, which suggests that the production mechanisms and/or form factors of the $\Lambda(1405)$ photoproduction are largely different from those of the $\Sigma^0(1385)$. The differential cross sections of the $\Sigma^0(1385)$ and $\Lambda(1405)$ photoproduction were obtained in the range of $K^+$ polar angle of $0.8 < \cos\Theta_{K_{CM}} < 1.0$. The differential cross sections of $\Sigma^0(1385)$ production were obtained as $0.80 \pm 0.092(stat.)^{+0.062}_{-0.27}(syst.)$ $\mu$b for $1.5 < E_\gamma < 2.0$ GeV and $0.87 \pm 0.064(stat.)^{+0.13}_{-0.067}(syst.)$ $\mu$b for $2.0 < E_\gamma < 2.4$ GeV. Those of $\Lambda(1405)$ production were found to be $0.43 \pm 0.088(stat.)^{+0.034}_{-0.14}(syst.)$ for $1.5 < E_\gamma < 2.0$ GeV. The production cross section in higher photon energy region could not be measured accurately, but an upper limit of 95% confidence level was extracted as $0.19$ $\mu$b.

For the study on the production mechanisms and the form factor of the $\Sigma^0(1385)$ and $\Lambda(1405)$ , more data with high statistics is necessary. The TPC used in this work was designed for the study of the lineshape of the $\Lambda(1405)$ in the nuclear medium, and thus, the TPC was used with a nuclear target. In this work, the production ratios of the $\Lambda(1405)$ to $\Sigma^0(1385)$ were obtained for free protons in $CH_2$ by subtracting the spectra of carbon from those of $CH_2$. However, a liquid hydrogen target has advantage for the study of the production of hyperon resonances on the proton. A TPC which can be operated with a liquid hydrogen target has been newly constructed at SPring-8/LEPS for the study of the pentaquark state, $\Theta^+$, via the $\gamma p \to K^0(892)\Theta^+$ reaction. The data taking using this TPC with the liquid hydrogen target is underway. The photoproduction of the $\Sigma^0(1385)$ and $\Lambda(1405)$ can be studied using this new data, and clean data of the differential cross sections of the $\Sigma^0(1385)$ and $\Lambda(1405)$ production will be available in near future.

In this work, the differential cross sections of the $\Sigma^0(1385)$ and $\Lambda(1405)$ have been measured in the range of $K^+$ polar angle of $0.8 < \cos\Theta_{K_{CM}} < 1.0$ by detecting $K^+$'s scattered to forward region. However, for the study of the production mechanisms and the form factor of hyperon resonances, the angular dependence of the production cross section is also important. The CLAS experiment at TJNAF and a new high intensity $\gamma$-ray beam line which is planned at SPring-8 (LEPS2) can measure the production cross section of hyperon resonances in large angular coverage. The CLAS group took data of the production of hyperon resonances on proton, and they reported the cross section of $\Sigma^0(1385)$ photoproduction in Ref. [46]. The detector system of the CLAS experiment covers the backward region in which particles have large scattering angles. The detector system of the LEPS2 experiment is designed to cover from forward to backward region. The experimental data of the production cross sections of the $\Lambda(1405)$ from these two facilities will be important for the further study on the production mechanisms and the internal structure of the $\Sigma^0(1385)$ and $\Lambda(1405)$.

# Chapter 7

# Acknowledgement

# Appendix A

# Drift of electron in the magnetic field

The electron cluster ionized by a charged particle travels in the active volume of the TPC up to 770 mm. For the reconstruction of the trajectory of the particle, it is necessary to obtain the coordinates where the argon atom was ionized to the electron ion pair. The coordinate in the drift direction was obtained from the drift time of the electron cluster by solving the equation of motion of the electron in the gas in the electric and magnetic field. The drift velocity of the electron in the electric and magnetic field is described by the Langevin equation as [1],

$$\boldsymbol{u} = \frac{\mu|\boldsymbol{E}|}{1+\omega^2\tau^2}\left(\hat{\boldsymbol{E}} + \omega\tau(\hat{\boldsymbol{E}}\times\hat{\boldsymbol{B}}) + \omega^2\tau^2(\hat{\boldsymbol{E}}\cdot\hat{\boldsymbol{B}})\hat{\boldsymbol{B}}\right) \tag{A.1}$$

where $\hat{\boldsymbol{E}}$ and $\hat{\boldsymbol{B}}$ are unit vectors in the directions of the electric and magnetic fields respectively, $\mu$ is the electron mobility in the gas, $\omega$ is the cyclotron frequency $eB/mc$, and $\tau = \mu m/e$ is the mean time between collisions of the drifting electron. The magnetic field was obtained from the calculation using finite-element method, and the magnitude at the center of the solenoid magnet was 2 T. The magnitude of the electric field was set to be 18 V/mm, and the typical drift velocity was 50 mm/$\mu$sec. The first term indicate the drift velocity of electrons without the magnetic field. The second term represent the $E \times B$ effect which bends the electrons in the direction perpendicular to the electric and magnetic field. The solenoid magnet makes the cylindrically symmetric magnetic field which bends in radial direction. In this case, the $E \times B$ term bend the electrons in azimuthal direction. The third term is most important for our measurement. Under the strong magnetic field, the electrons rotate along the magnetic field and drift along the magnetic field. In this measurement, the magnetic field of 2 T is sufficiently strong and the third term is dominated.

The mobility of the electron in the active volume of the TPC has changed up to 14% while the data taking, depending on the pressure of the p10 gas. The

mobility was monitored using the events created at the carbon plate embedded on the shield wire and the kapton membrane embedded on the inner end of the target holder. Fig. A.1 shows a distribution of z-coordinate of two-track vertexes (vtz) in the target region (top) and the shield wire region (bottom), where the mobility was assumed as the typical value of $50/18 = 2.78$ mm$^2$/(V·$\mu$s).
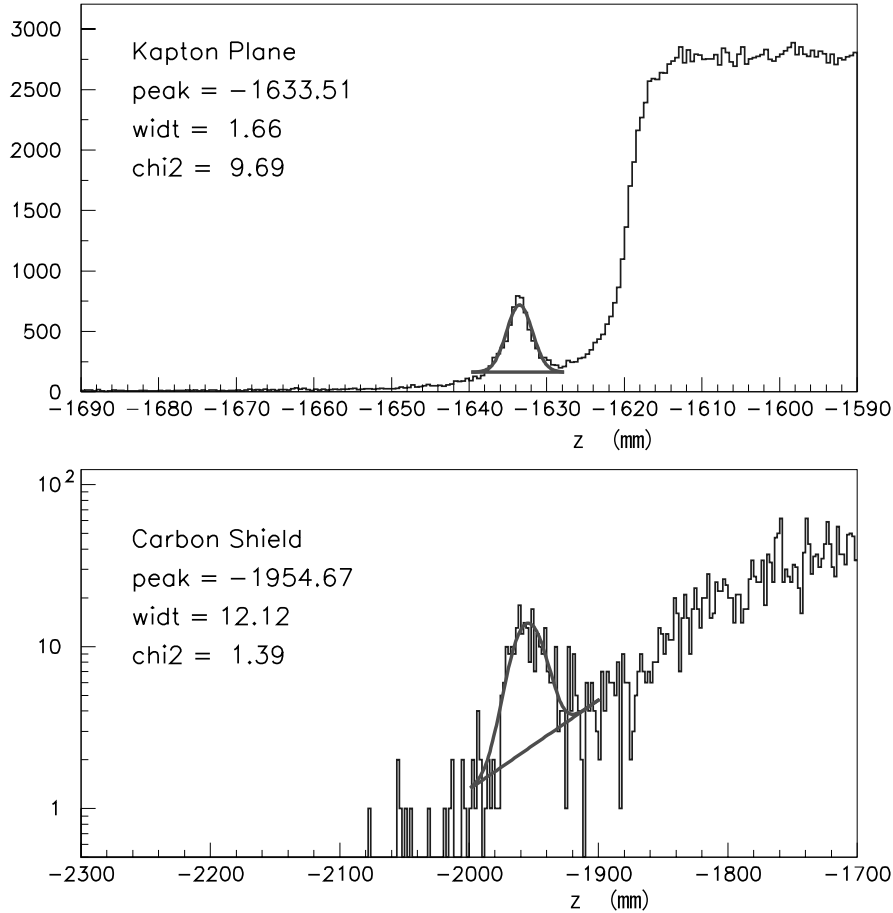


Figure A.1: Distribution of z-coordinate of two-track vertexes in the target region (top) and the shield wire region (bottom).

The events in $-1640 < z < -1630$ mm and $z > -1620$ mm in Fig. A.1 (top) were produced from the kapton membrane and the CH$_2$ target, respectively. The events in the peak shown in the Fig. A.1 (bottom) were produced from the carbon plate on the shield wire. The background events under the peak were due to the shower events produced at the downstream of the upstream-veto counter. The mobility of the electron was obtained using the ratio of the observed distance between the

carbon plate and the kapton membrane ($L$) to the real distance, 315 mm, as $\mu = 2.78 \cdot L/315$ mm$^2$/(V·$\mu$s), where the magnetic field was assume as parallel to the electric field.

Then, the hit coordinate in the drift direction was obtained by solving the equation A.1 using the drift time, the mobility obtained above and the position of the avalanche in the pad plane determined from the center-of-gravity of the pads as the initial position. The mean of the tracking residuals obtained in each layer was slightly shifted from zero, depending on the signal hight and the scattering angle of the track. These shifts were corrected empirically.

# Appendix B

# Spatial resolution and detection efficiency of the TPC

## B.1  Spatial resolution in the azimuthal direction

The hit coordinates in the azimuthal direction ($\phi$) were obtained using the center-of-gravity of the induced charges on pads. The position measurement error for MIPs in the azimuthal direction can be described in terms of the drift diffusion of electrons, the track wire crossing angle ($\alpha$) and the track pad crossing angle ($\beta$). Fig. B.1 shows a schematic view of the geometry of the pads and wires. The spatial resolution in the azimuthal direction can be written as

$$\sigma_\phi = \sigma_0^2 + \sigma_D^2(1 + \tan^2\alpha)L/L_{\max} + \sigma_\alpha^2(\tan\alpha - \tan\psi)^2 + \sigma_\beta^2\tan^2\beta, \quad \text{(B.1)}$$

where $L$ is the drift distance and $\psi$ is the Lorentz angle.
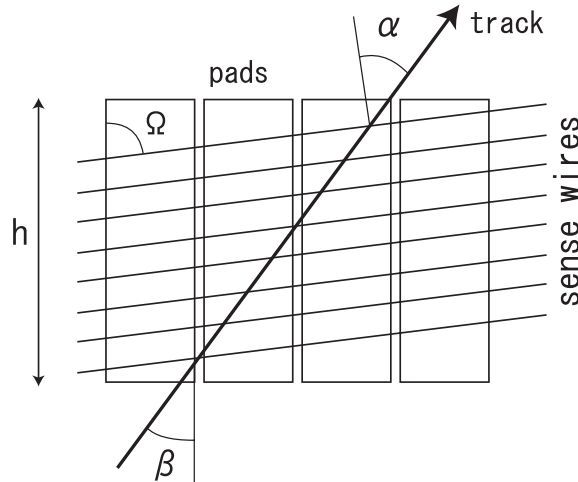


Figure B.1: Schematic view of the geometry of the pads and wires.

The first, second, third and fourth terms represent the contributions of the intrinsic resolution, the drift diffusion effect, the track-wire angular effect and the track-pad angular effect, respectively. In addition to these terms, the spatial resolution depends on the angle between the pad and wires ($\Omega$).

## B.1.1 The effect of the pad-wire angle

In this TPC, the angle between a pad and wires ($\Omega$ in Fig. B.1) varies from 0 to 180 degrees, see Fig. 2.20. Fig. B.2 shows a schematic drawing of the pads in the second inner layer. The straight lines are the sense wires. There are 32 pads in the second layer and these pads are labeled clockwise. For pads 5, 6, 7, 21, 22 and 23, the angles ($\Omega$) are close to 0 or 180 degrees, and the avalanche position along the pad raw ($\phi$) are fixed at the position of the sense wire. Fig. B.3 shows distributions of the center-of-gravity of the induced charges on pads in the second inner layer. The horizontal axes correspond to the position of the center-of-gravity measured from the pad center where 0 corresponds to the center of the each pad. The pad numbers correspond to those in Fig. B.2. Clear peaks corresponding to the wire position are seen for pad with $\Omega \sim 0$ or 180 degrees. For these pads, the position measurement errors were set to be $4/\sqrt{12}$ mm, where 4 mm is the wire pitch.
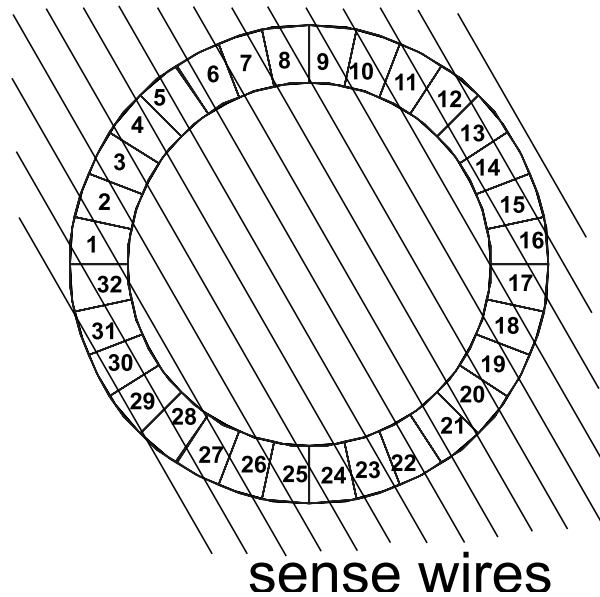


Figure B.2: Schematic view of the geometry of the pads and wires for the second inner layer.

# Layer2
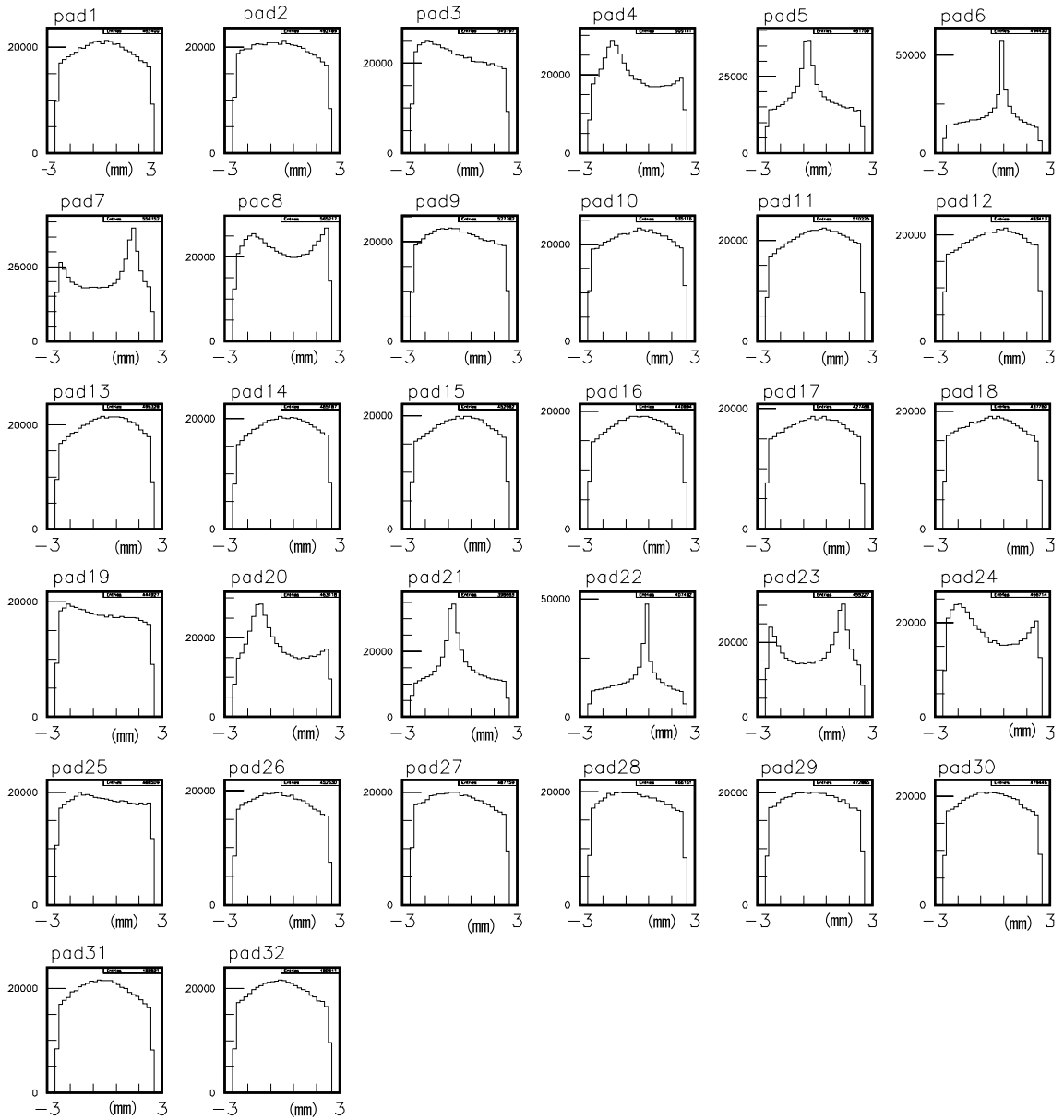


Figure B.3: Distributions of the center of gravity of the induced charges measured from the center of the pad.

## B.1.2 The effect of the transverse diffusion

The second term in the equation B.1 represents the effect of the transverse diffusion. The strong magnetic field parallel to the drift direction suppresses transverse diffusion by a factor $D(B)/D(0) = 1/(1+\omega^2\tau^2)$, where $D$ is the diffusion coefficient, $\omega = eB/mc$ is the cyclotron frequency, and $\tau$ is the mean time between collisions. In this experiment, the magnitude of the magnetic field in the active volume was 1.5-2 Tesla, and the $\omega\tau$ was 7-8. Fig. B.4 shows a correlation plot between the widths (RMS) of the tracking residuals in the azimuthal direction ($\phi$) and the drift distance for cosmic ray tracks. The tracks in short drift distance region were not measured. The width was almost constant with respect to the drift distance because the transverse diffusion is suppressed by the magnetic field.
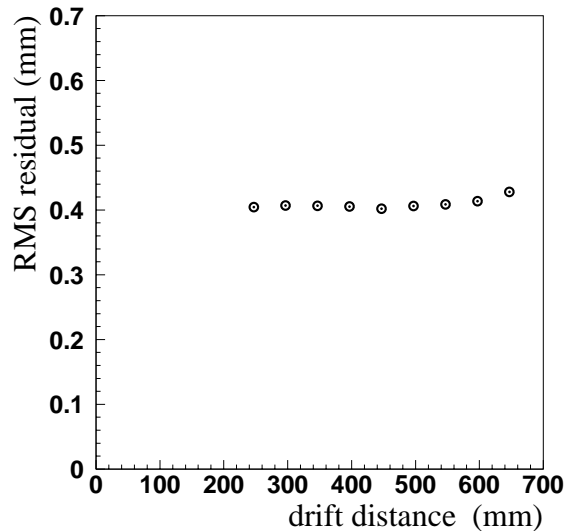


Figure B.4: Correlation between the widths (RMS) of the tracking residuals in the azimuthal direction and the drift distance.

## B.1.3 The effect of the track-wire angle

The third term in the equation B.1, $\sigma_\alpha^2(\tan\alpha - \tan\psi)^2$, represents the effect of the track-wire angle. Fig. B.5 shows a schematic view of the track-wire angle ($\alpha$) without (a) and with (b) the magnetic field. The thick lines indicate the avalanche region on the sense wires. The avalanche region is spread along the wire if $\alpha$ is not zero. When the magnetic field is on, the electrons drift towards the wire with the Lorentz angle $\psi$ due to the $E \times B$ effect near the sense wire. The $E \times B$ effect broadens the spread along the wire if $\alpha$ and $\psi$ have opposite signs. On the other hand, if $\alpha = \psi$,

the angular spread is compensated by the $E \times B$ effect. Fig. B.6 shows a correlation plot between the widths (RMS) of the tracking residuals in the azimuthal direction ($\phi$) and the track-wire angle ($\alpha$) for protons produced from the $CH_2$ target. The width of the residuals becomes wider if the track-wire angle is close to $\pm 90$ degrees. The minimum point of the width slightly shifted from 0 degree due to the $E \times B$ effect.
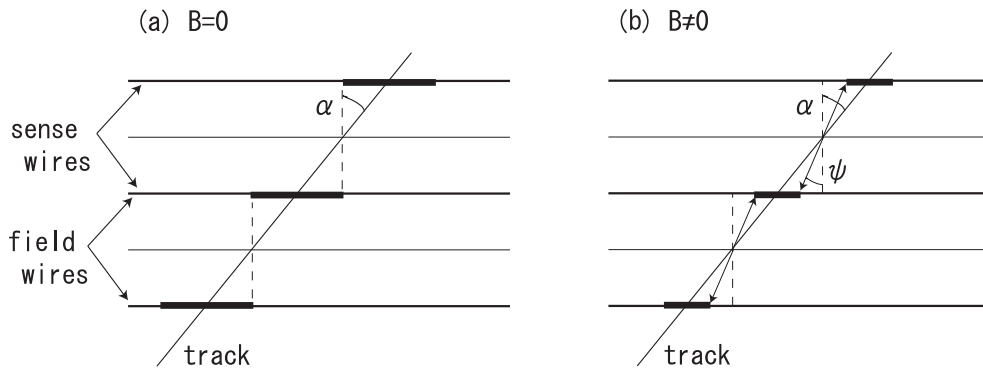


Figure B.5: Schematic view of the track-wire angle.
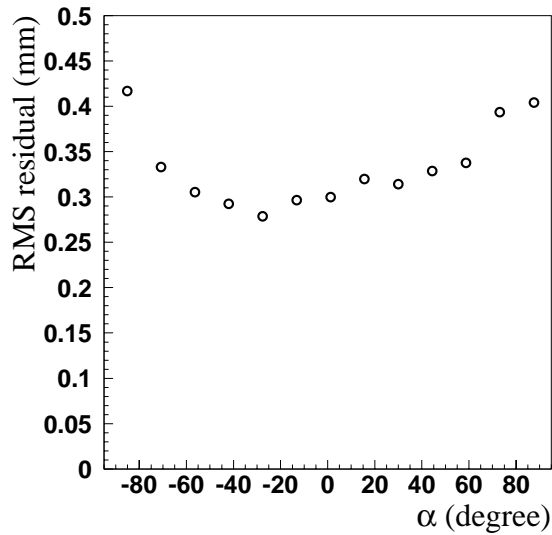


Figure B.6: Correlation between the widths (RMS) of the tracking residuals in the azimuthal direction and the track-wire angle ($\alpha$).

## B.1.4    The effect of the track-pad angle

The last term in the equation B.1, $\sigma_\beta^2 \tan^2 \beta$, represents the effect of the track-pad angle ($\beta$). In order to investigate the track-pad angular effect, $\pi^+/\pi^-$ tracks were used instead of proton tracks because the track-pad angle depends on the charge and momentum of the particle, and low momentum protons are concentrated in the negative $\beta$ region. Fig. B.7 shows a correlation plot between the widths (RMS) of the tracking residuals in the azimuthal direction ($\phi$) and the track-pad angle ($\beta$) for charged pions produced from the $CH_2$ target. The minimum of the width is around 0 degrees, but it is slightly shifted from 0 due to contamination of protons.
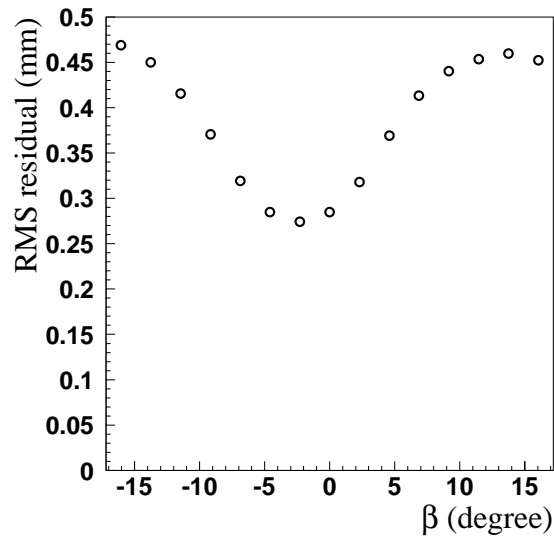


Figure B.7: Correlation between the widths (RMS) of the tracking residuals in the azimuthal direction and the track-pad angle ($\beta$).

## B.1.5    Pulse height dependence

Fig. B.8 shows a correlation plot between the widths (RMS) of the tracking residuals in the azimuthal direction and the signal height for proton (left) and pion (right) tracks. The tracks which satisfy the conditions of $|\alpha| < 40$ were selected. The spatial resolution becomes worse for small pulse height signals produced by pion tracks because the signal to noise ratio becomes worse. The position measurement errors were obtained from the mean of the widths for pions and protons and used for the track fitting.
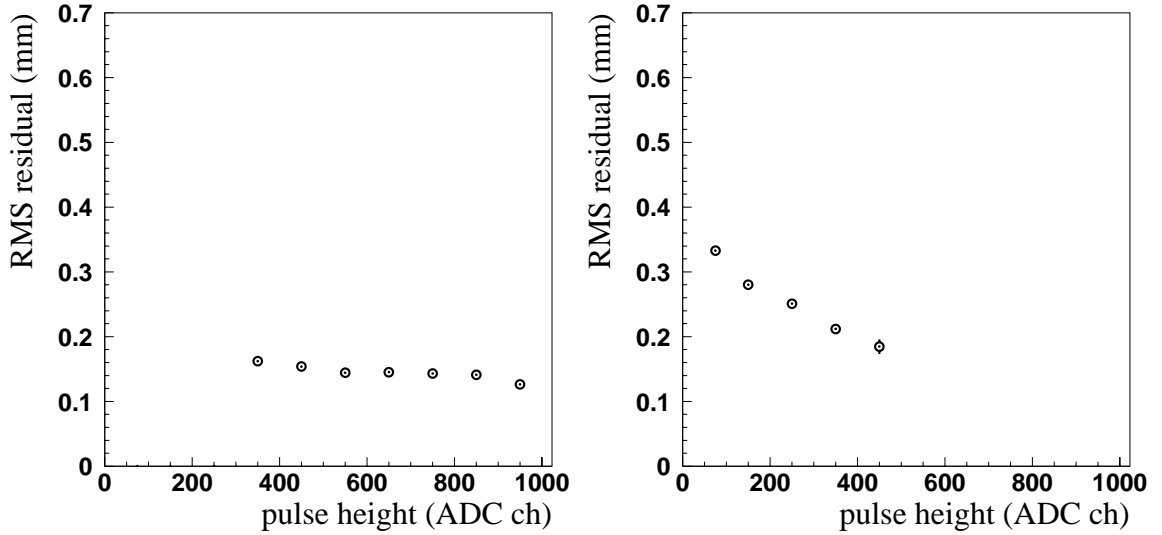
Figure B.8: Correlation between the widths (RMS) of the tracking residuals in the azimuthal direction and the signal height for proton tracks (left) and pion tracks (right).

## B.2   Spatial resolution in the drift direction

The position measurement error in the drift direction can be described as

$$\sigma_z^2 \;=\; \sigma_0^2 + \sigma_D^2 \cdot L/L_{\mathrm{max}} + (h \cdot \tan \lambda)^2, \tag{B.2}$$

where $L$ is the drift distance, $h$ is the length of the pad and $\lambda$ is the angle between a track and the pad plane (dip angle). The first term represents the intrinsic resolution, and the second and third terms represent the effect of the drift diffusion and dip angle, respectively. Fig. B.9 shows a correlation plot between the widths (RMS) of the tracking residuals in the drift direction and the drift distance for cosmic ray tracks with the dip angle of $|\lambda| < 5.6$ degrees. The tracks in the short drift distance region were not measured. The widths of the tracking residuals become larger as the drift distance due to the longitudinal diffusion.
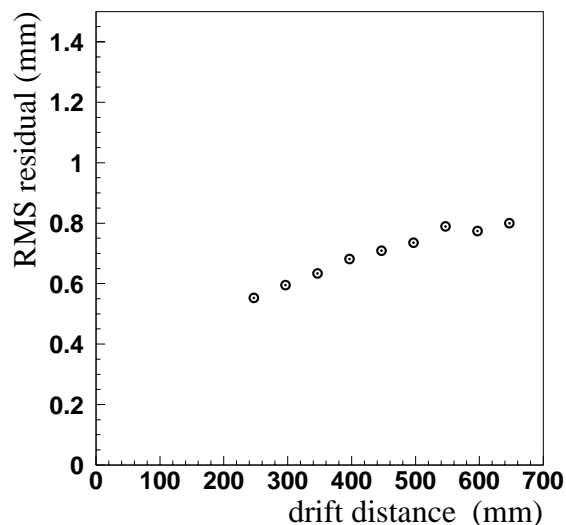
Figure B.9: Correlation between the widths (RMS) of the tracking residuals in the drift direction and the drift distance.

The last term of equation B.2 represents the effect of the dip angle. The effect of the dip angle is correlated with the drift diffusion effect because the particles were generated from the target which was located in the middle of the drift area and the electrons generated by the track with a negative dip angle drift short distance until the sense wire region. Fig. B.10 shows a correlation plot between the widths (RMS) of the tracking residuals in the drift direction and the dip angle ($\lambda$) for particles generated from the $CH_2$ target. The correlations in the 9th layer were plotted in 10 pulse hight bins. The forward (backward) going particles have positive (negative) dip angles, and $\lambda \sim 0$ corresponds to the track which is parallel to the pad plane. The correlations are asymmetric because the tracks in the negative dip angle region have small widths due to short drift distance from the track to the sense wires. The spatial resolutions as a function of the dip angle were fitted with 3rd polynomial functions in each pulse height bins to obtain the position measurement errors used for the track fitting.
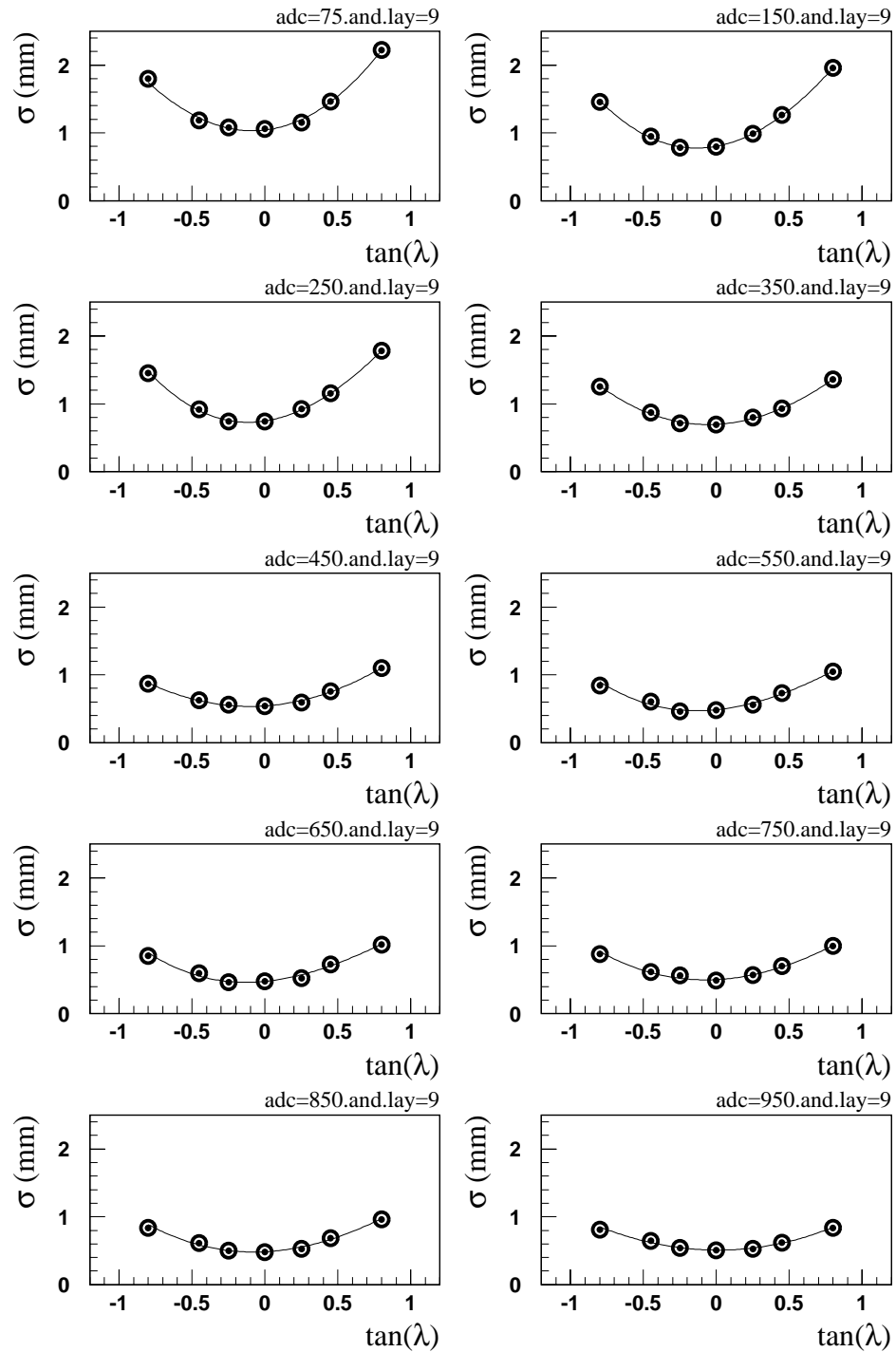
Figure B.10: Correlation between the widths (RMS) of the tracking residuals in the drift direction and the dip angle ($\lambda$).

## B.3    Spatial resolution of the most inner layer

The electric field near the target holder is not uniform, and the drift path of electrons on the most inner pad layer is distorted due to the target holder. Fig. B.11 shows distributions of tracking residuals for the most inner pads in the azimuthal direction (left) and drift direction (right). The spatial resolution in the azimuthal direction was obtained from a Gaussian fit to be 0.73 mm. The distribution of the tracking residuals in the drift direction is shifted to the positive side because the electric field near the target holder is distorted and the drift path could not be obtained correctly.
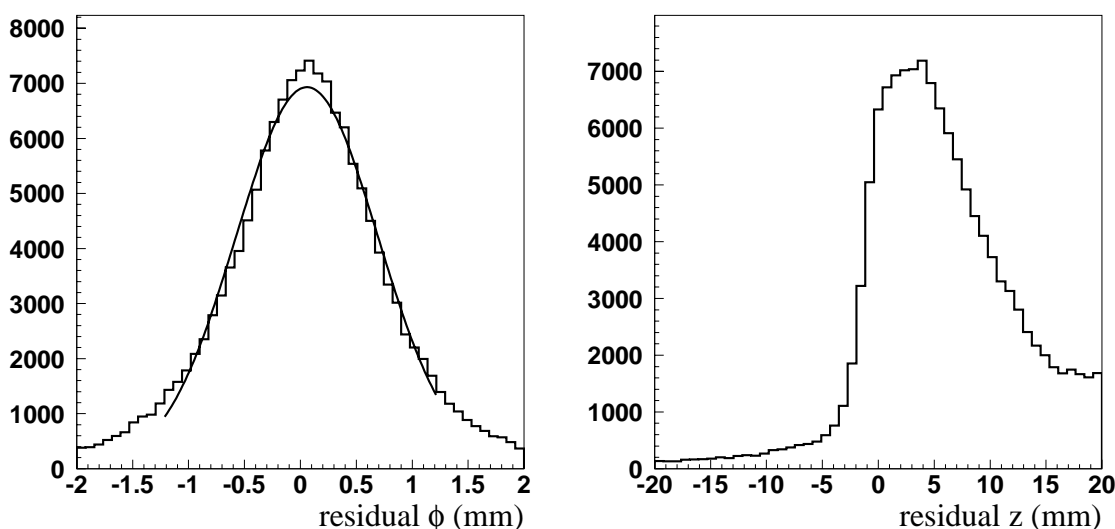


Figure B.11: Distributions of the tracking residuals in the azimuthal direction (left) and drift direction (right) for the most inner pads.

## B.4    Detection efficiency

Fig. B.12 shows the detection efficiency as a function of the pad number from layer 1 to 13. The lines indicate 98% efficiency. The detection efficiency in each layer was higher than 98% except for the pads in the most inner layer.
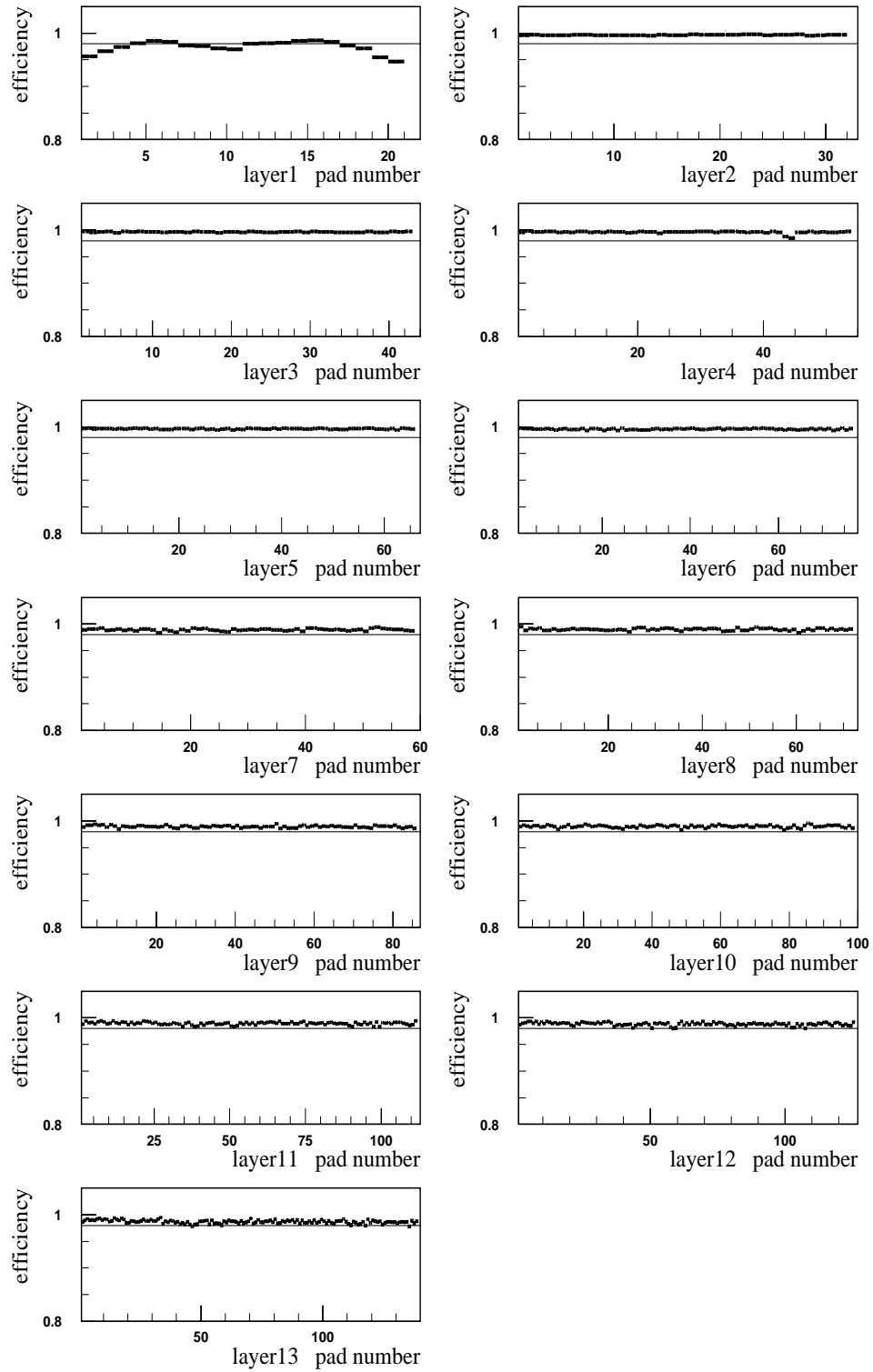
Figure B.12: Detection efficiency as a function of the pad number.

# Appendix C

# Particle identification by the TPC

The energy deposition ($dE/dx$) of the charged particle in the TPC was calculated using the truncated mean of the induced charge on the pads, where the threshold of the truncation was set as 60% of the largest signal. Fig. C.1 shows a correlation between the $dE/dx$ and momentum of particles measured by the TPC for events a $\pi^+$ was detected in the LEPS spectrometer. Fig. C.1 left and right show distributions for positively and negatively charged particles, respectively. The band in Fig. C.1 (right) with larger $dE/dx$ than $\pi^-$ band corresponds to protons which were produced at the yoke of the solenoidal magnet and passed through the active volume of the TPC. The charge of these protons were misidentified as negative if they travels towards the target. The distributions of protons and $\pi^-$'s were fitted with the Bethe-Bloch function, where the scale and offset were determined from the fitting. The solid lines show the fit result.
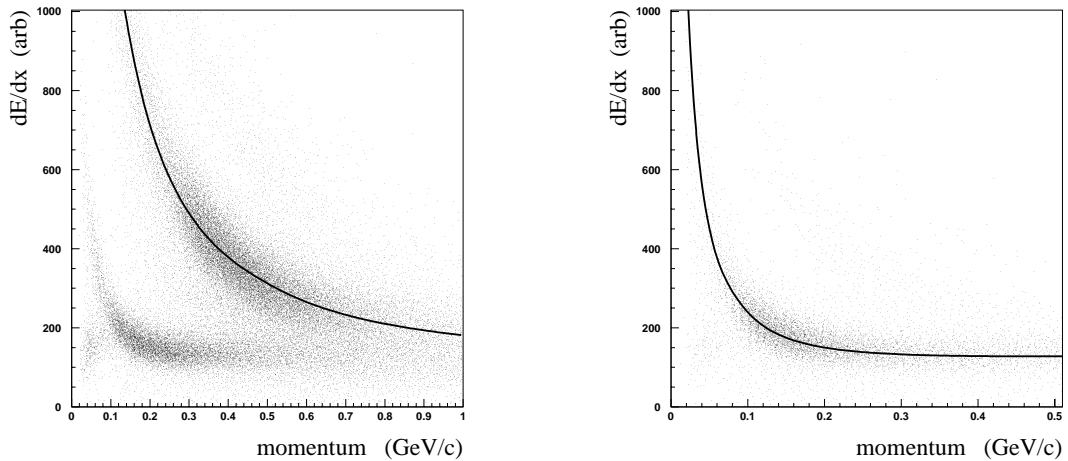


Figure C.1: Correlation between the $dE/dx$ and momentum of a positively charged particle (left) and negatively charged particles (right) measured by the TPC.

Then, the distributions of the difference between the measured $dE/dx$ and the Bethe-Bloch function was obtained in each momentum region, and fitted by Gaussians, Fig. C.2 shows the distributions of the difference between the measured $dE/dx$ and the Bethe-Bloch function for positively charged particles (left) and negatively charged particles (right). The solid lines show the fit results. The higher peak in Fig. C.2 left corresponds to protons, and the peak in Fig. C.2 right corresponds to $\pi^-$'s. The lower peak in the left plot corresponds to $\pi^+$'s. The RMS widths were used to determine the boundaries of the particle identification. The solid and dot-dashed lines in Fig. C.3 show the $3\sigma$ boundaries for the protons. The dashed and dot-dot-dashed lines show the boundaries of the pion selection. The $3\sigma$ boundaries of $dE/dx$ for protons and pions overlaps at the momentum of 0.35 GeV/c. A positive particle with larger $dE/dx$ than the pion selection boundary or with higher momentum than 0.35 GeV/c was identified as a proton.
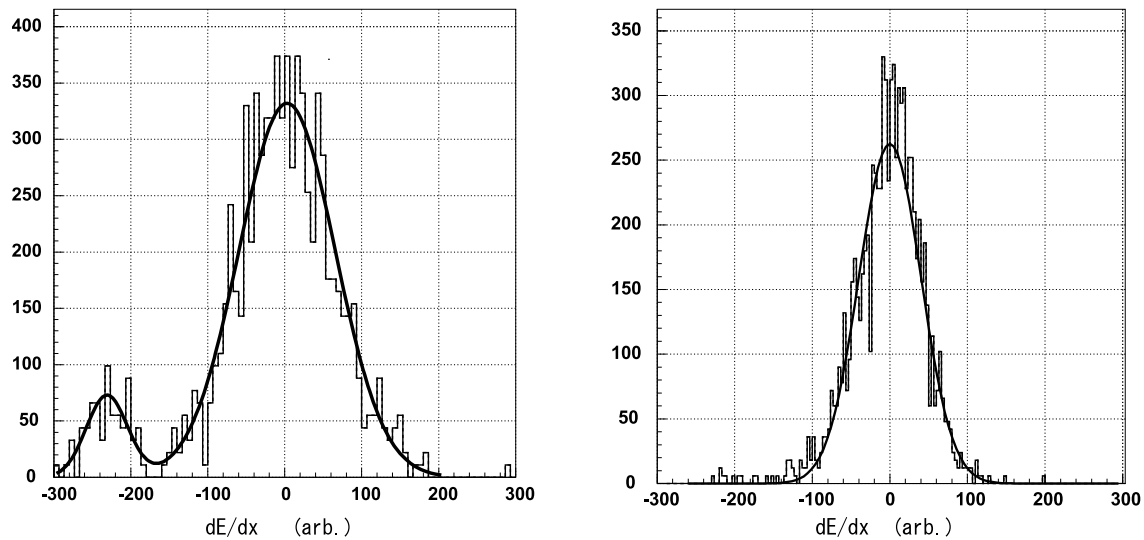


Figure C.2: Distribution of the difference between measured $dE/dx$ and the Bethe-Bloch function.
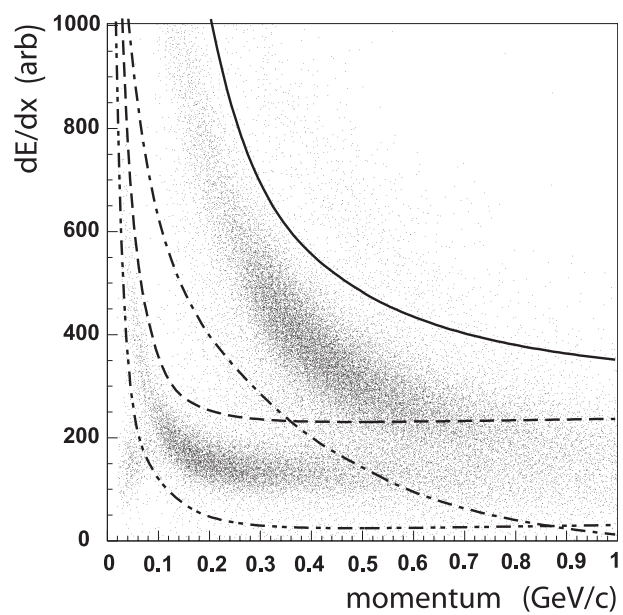
Figure C.3: Correlation between the $dE/dx$ and momentum of particles measured by the TPC. The solid and dot-dashed lines show the $3\sigma$ boundaries for the $dE/dx$ of protons, and the dashed and dot-dot-dashed lines show those of the pions.

# Appendix D

# Particle misidentification by the LEPS spectrometer

In this chapter, the background due to particle misidentification by the LEPS spectrometer is described. The $K^+$'s produced by the $\gamma p \to K^+ X$ reaction were identified from the mass reconstructed using the momentum and velocity measured by the LEPS spectrometer. The velocity was measured using the path length of the trajectory and the time-of-flight from the target to the TOF counter. The start of the time-of-flight measurement was determined using the RF signal of the electron storage ring of SPring-8. The start counter was used as a reference counter to select the RF signal corresponding to the Compton scattered photon. Sometimes, however, the selection of the electron bunch was not correct due to the time resolution of the start counter. In such events, the time-of-flight was not obtained correctly, and a proton or a $\pi^+$ was misidentified as a $K^+$. These events cause the background for the identification of the particles by the missing mass technique.

In the section 3.4.1, neutrons produced from the $\gamma p \to K^+ \pi^+ \pi^-$ reaction were identified through the missing mass technique, and the background events below the neutron mass were observed. Figure D.1 (left) shows a distribution of $MM(K^+\pi^+\pi^-)$. The background events are seen around $0.7 \sim 0.9\,\mathrm{GeV/c^2}$, below the peak of neutron mass.
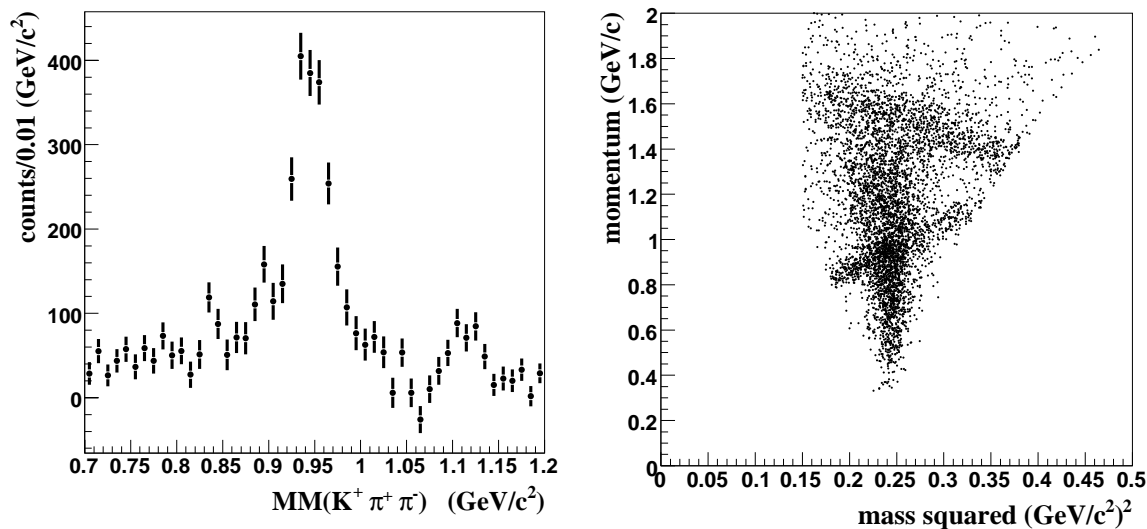
Figure D.1: The left plot shows a distribution of $MM(K^+\pi^+\pi^-)$. The right plot shows a correlation plot between the momentum and mass of $K^+$ candidates measured by the LEPS spectrometer for events in the region of $0.7 < MM(K^+\pi^+\pi^-) < 0.9$ GeV/c$^2$.

The right plot of Figure D.1 shows a correlation plot between the momentum and mass of $K^+$ candidates measured by the LEPS spectrometer for events in the region of $0.7 < MM(K^+\pi^+\pi^-) < 0.9$ GeV/c$^2$. The contamination from $\pi^+$'s and protons is seen as a band in the momentum region of $0.8 \sim 1.1$ GeV/c, and $1.4 \sim 1.8$ GeV/c, respectively. Thus, the contamination rate depends on the momentum range. In order to estimate the contamination due to particle misidentification, $\pi^+$'s and protons were selected by the LEPS spectrometer and assigned the mass of the kaon, and then, the $MM(K^+\pi^+\pi^-)$ was calculated with the "fake" mass in five momentum regions. The obtained "fake" distribution of the $MM(K^+\pi^+\pi^-)$ was then fitted to the distribution of the $MM(K^+\pi^+\pi^-)$ in the region of $0.7 < MM(K^+\pi^+\pi^-) < 0.9$ GeV/c$^2$ to estimate the contamination rate. The distributions of $MM(K^+\pi^+\pi^-)$ are shown in five momentum ranges in Fig. D.2, (a) $p_{K^+} < 0.8$ GeV/c, (b) $0.8 < p_{K^+} < 1.1$ GeV/c, (c) $1.1 < p_{K^+} < 1.3$ GeV/c, (d) $1.3 < p_{K^+} < 1.7$ GeV/c, (e) $1.7 < p_{K^+}$ GeV/c. The open and closed circles show the contamination of protons and $\pi^+$'s, respectively. The normalizations of each contribution are determined by fitting.
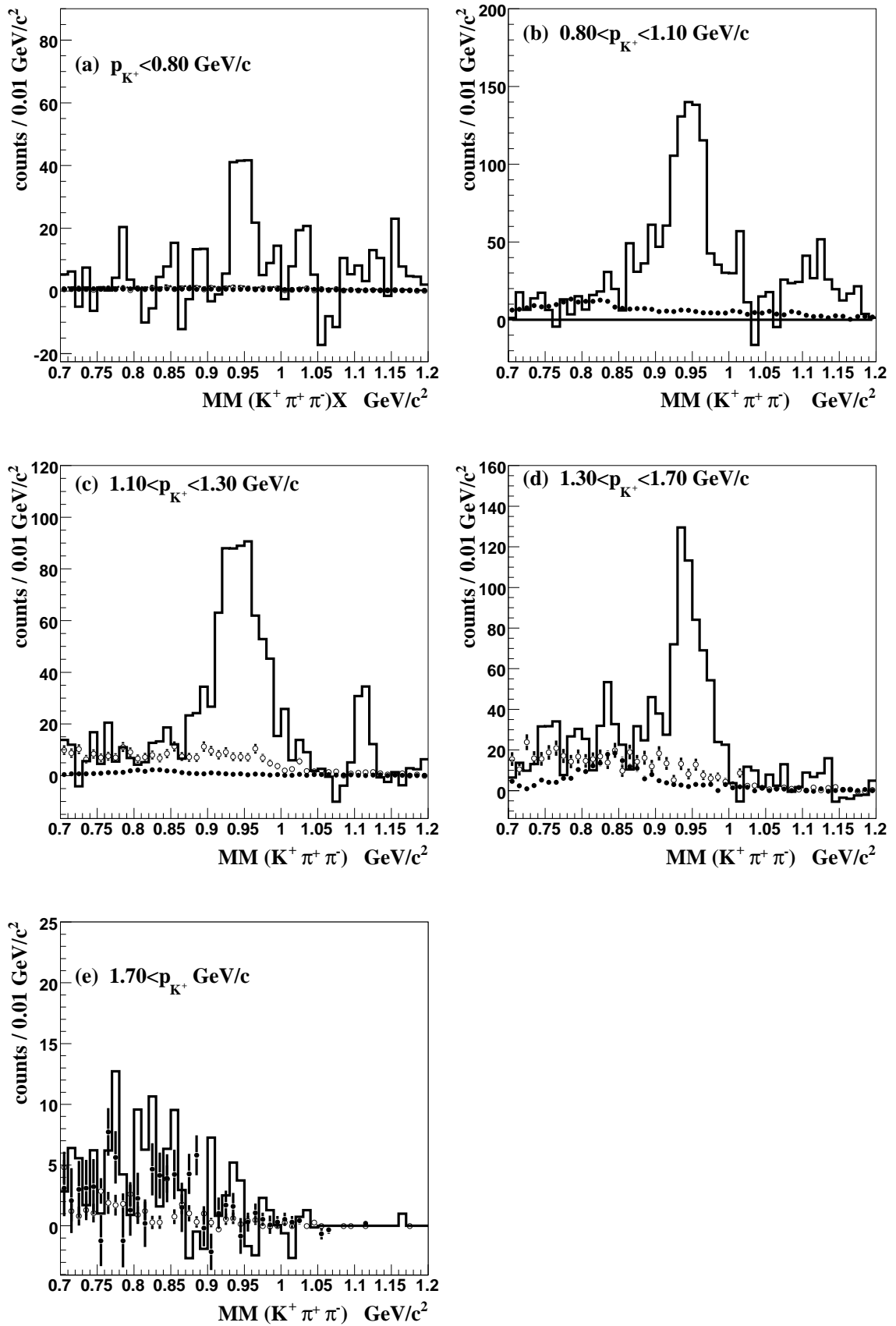
Figure D.2: Distributions of $MM(K^+\pi^+\pi^-)$ in five momentum ranges.

Open circles in Fig. D.3 show a distribution of $MM(K^+\pi^+\pi^-)$. The solid and dashed lines show the fit result and the contamination from the particle misidentification estimated above, respectively. The contamination of this background into the neutron mass region was estimated to be 8%.
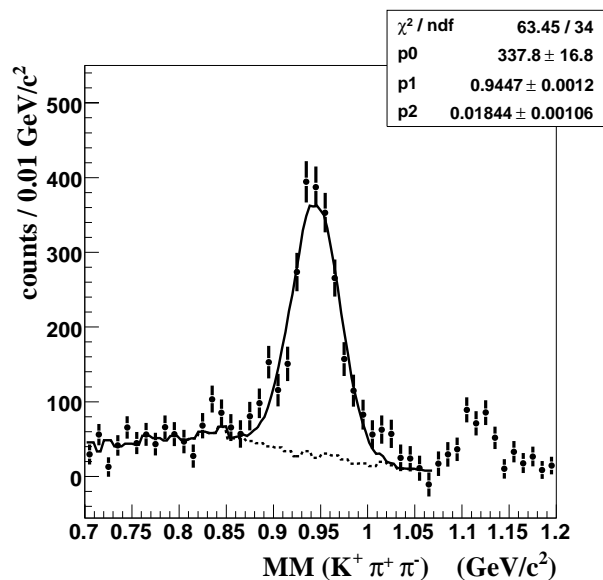


Figure D.3: Distributions of $MM(K^+\pi^+\pi^-)$. Solid and dashed lines show the fit result and the background due to particle misidentification by the LEPS spectrometer, respectively.

# Appendix E

# Contamination from $K^0(892)$ production

In this section, the contamination from the $\gamma\,p \rightarrow K^0(892)\Sigma^+ \rightarrow K^+\pi^-\Sigma^+$ reaction is discussed. This reaction has same particles in the final state as $\gamma\,p \rightarrow K^+\Lambda(1405) \rightarrow K^+\pi^-\Sigma^+$ reaction. Fig. E.1 shows spectra for the events generated by a MC simulation of $K^0(892)\Sigma^+$ production. Fig. E.1 (a) shows an invariant mass spectrum of $(K^+\pi^-)$ pairs. A peak corresponding to $K^0(892)$ is seen, and the width (FWHM) was obtained as 55 MeV/c$^2$. Fig. E.1 (b) shows a distribution of $MM(K^+)$. The spectrum is broadly distributed peaking at 1.5 GeV/c$^2$.
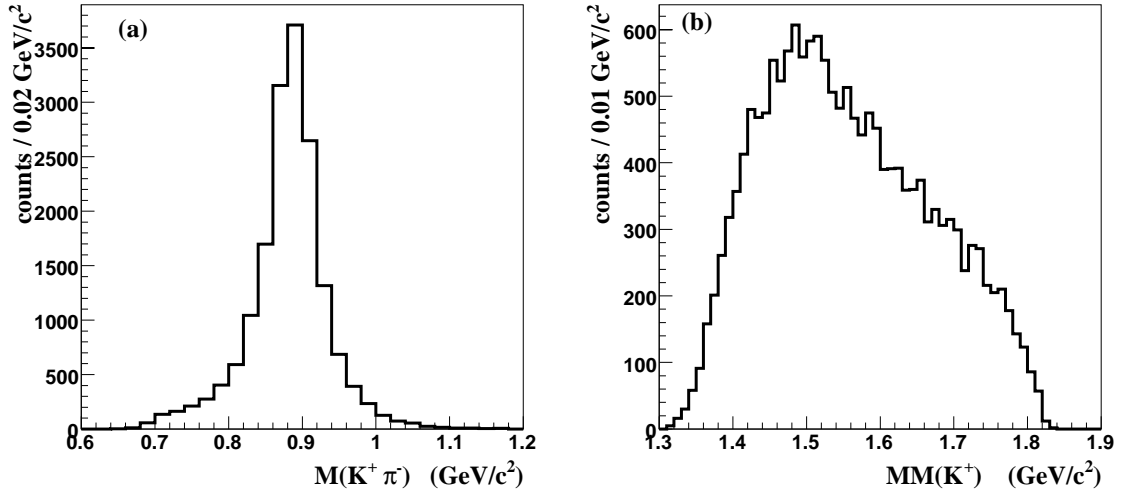
Figure E.1: Monte Carlo simulation for $K^{*0}(892)$ photoproduction. (a) shows an invariant spectrum of $(K^+\pi^-)$ pairs. (b) shows a distribution of $MM(K^+)$.

131

Fig. E.2 (a) and (b) show invariant mass of $(K^+\pi^-)$ pairs in the energy range of $1.5 < E_\gamma < 2.0$ GeV and of $2.0 < E_\gamma < 2.4$ GeV, respectively. Solid and dashed histograms show spectra for $CH_2$ and carbon, respectively. The threshold photon energy for $K^0(890)\Sigma^+$ production is 1.9 GeV. Thus, $K^0(890)\Sigma^+$ production is seen only in higher photon energy region. Fig. E.3 shows an invariant mass spectrum in the energy range of $2.0 < E_\gamma < 2.4$ GeV for free protons. The background events were from $\Lambda(1405)$ and $\Lambda(1520)$ photoproduction and non resonant $K^+\Sigma^+\pi^-$ production. The spectrum for free protons was fitted by Monte Carlo spectra of $K^*(892)$, $\Lambda(1405)$, $\Lambda(1520)$ and nonresonant $K^+\Sigma^+\pi^-$ photoproduction. The contribution of $\Lambda(1520)$ production is dominated in this photon energy region, and is shown as the dashed histogram. The yield of $K^0(890)\Sigma^+$ production was obtained as $147 \pm 48$ events.
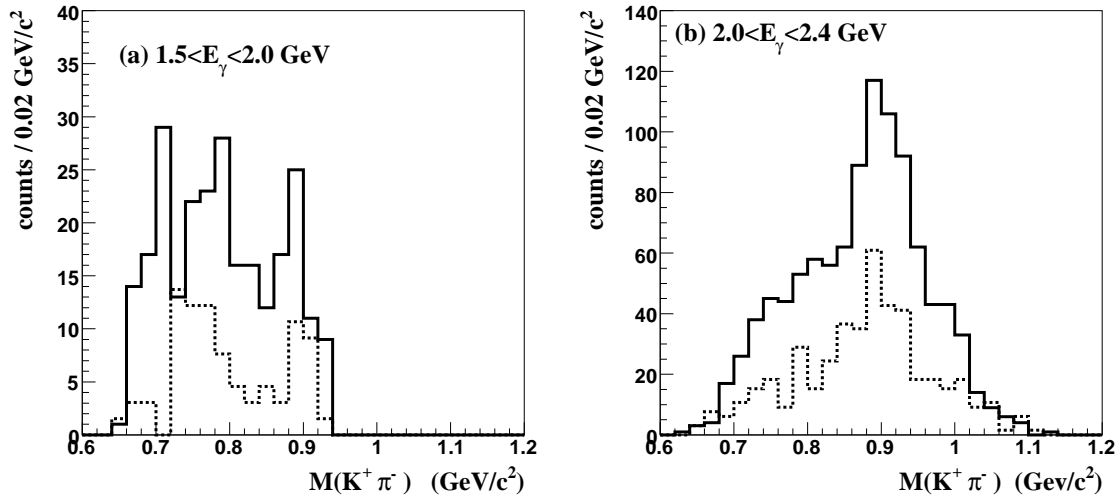


Figure E.2: Invariant mass spectra of $(K^+\pi^-)$ pairs. (a) Spectrum for $CH_2$ (solid) and for carbon (dashed) for photon energy range of $1.5 < E_\gamma < 2.0$ GeV. (b) Spectrum for $CH_2$ (solid) and for carbon (dashed) for photon energy range of $2.0 < E_\gamma < 2.4$ GeV.

133
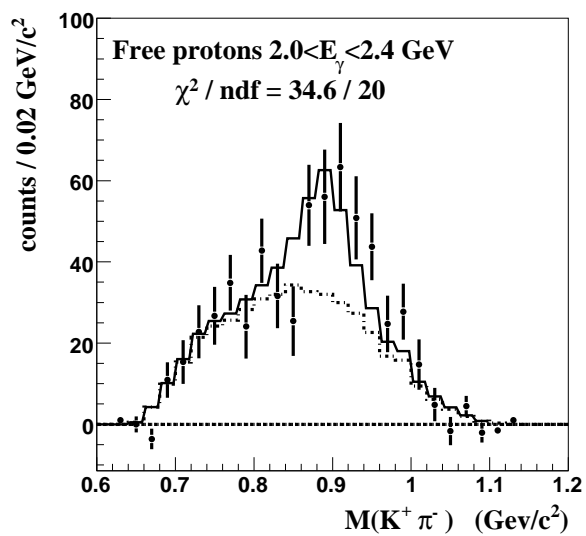
Figure E.3: Invariant mass spectrum of $(K^+\pi^-)$ pairs for free protons in $CH_2$ for $2.0 < E_\gamma < 2.4$ GeV.

# Appendix F

# Comparison with theoretical spectrum by Kaiser *et al.*

In this chapter, a theoretical calculation of the $\Lambda(1405)$ by Kaiser *et al.* [54] using the effective Lagrangian is compared with the experimental data. Fig. F.1 shows the missing mass of the $\gamma p \rightarrow K^+ X$ reaction for events with $(K^+\Sigma^+\pi^-)$ and $(K^+\Sigma^-\pi^+)$ final states. The combined spectra of $\Sigma^+\pi^-$ and $\Sigma^-\pi^+$ mode were used to cancel the effect of the isospin interference term as described in section 3.4.4.
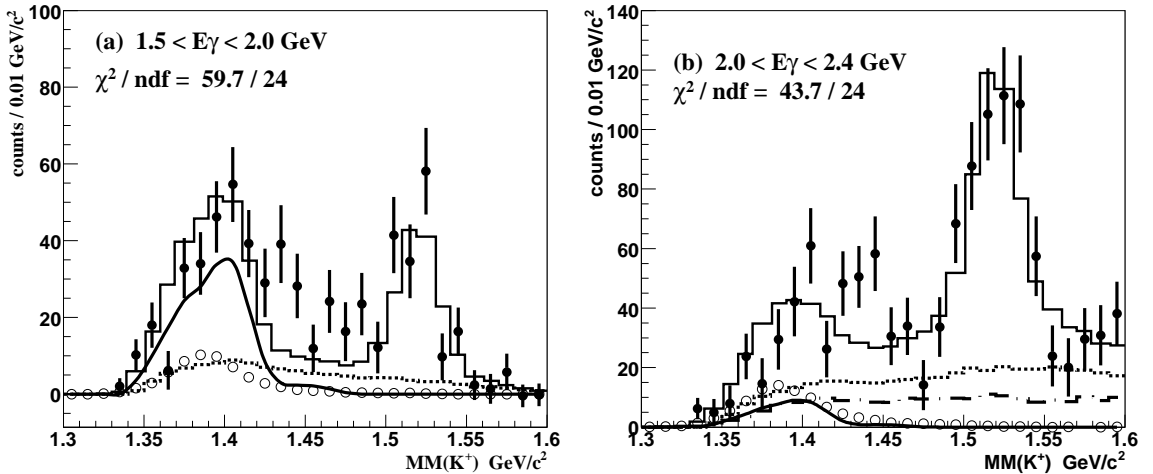


Figure F.1: Distributions of $MM(K^+)$. The combined spectra of the $\Sigma^+\pi^-$ and $\Sigma^-\pi^+$ mode are shown in the photon energy range of $1.5 < E_\gamma < 2.0$ GeV (a) and $2.0 < E_\gamma < 2.4$ GeV (b).

The closed circles show experimental data for free protons in $CH_2$. The spectrum was fitted using the theoretical spectrum by Kaiser *et al.* instead of the one by Nacher *et al.* The solid curves show the spectra of $\Lambda(1405)$ calculated by Kaiser *et*

135

*al.*, and the fit results are shown as the solid histograms. The $\chi^2/ndf$ were 2.5 and 1.8 for $1.5 < E_\gamma < 2.0$ GeV and $2.0 < E_\gamma < 2.4$ GeV, respectively. The $\chi^2$ was slightly worse than that by Nacher *et al.* but it seems consistent with the experimental data. The contributions from $\Sigma^0(1385)$ production estimated from $\Lambda\pi^0$ decay mode are shown as open circles. The estimated contribution of $K^0(892)\Sigma^+$ production is shown by the dot-dashed histogram. The dashed lines show the distribution for nonresonant $(K^+\Sigma\pi)$ production. The normalization factors of each contribution are determined by fitting.

# Appendix G

# Read out electronics for the TPC

In this chapter, the details on the read out electronics for the TPC is described. The read out electronics for the TPC consists of preamplifiers, shaping amplifiers and flash ADC (FADC) modules.

The preamplifier consists of integrating amplifiers and buffer amplifiers. Fig. G.1 shows a circuit diagram of a channel of the preamplifier. Low noise amplifier chips, LMH6655 of National Semiconductor co., were used for the integrating and buffer amplifier. The feedback capacitance of 4 pF was used for the integrating amplifier, and the integration time was 132 nsec. The buffer amplifier was used to set the output impedance to be 50 Ω. The gain of the preamplifier card was 2.5 V/pC in total. The channel by channel fluctuation of the gain was less than 1 %. In order to read signals from anode wires and cathode pads and to match the polarity of the output signal, the polarity of the buffer amplifier can be changed by soldering jumper pins.
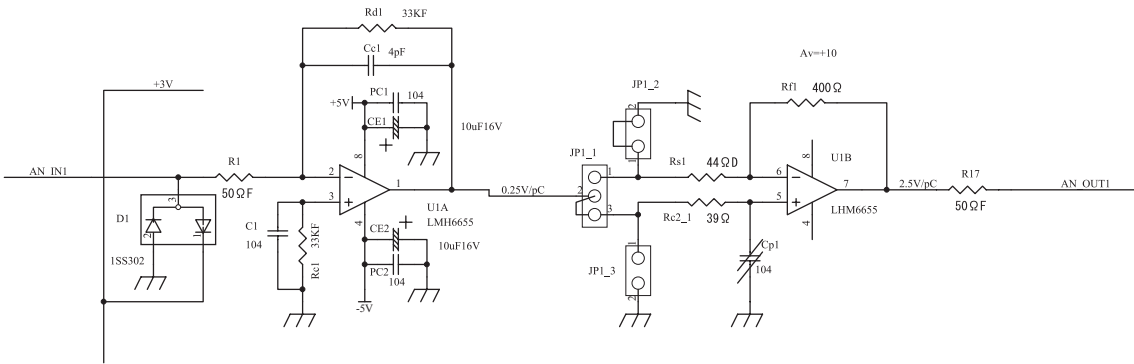


Figure G.1: Circuit diagram of the preamplifier used for the TPC.

The shaping amplifier was used as a band-pass filter, which rejects noise and changes the signal shape to be suitable for digitization by the FADC. The shaping amplifier consists of differentiating amplifiers with the pole-zero cancel, integrating amplifiers and differential drivers. Fig. G.2 shows a circuit diagram of a channel of the shaping amplifier. The shaping time was determined as 20 nsec to match the diffusion spreading of an electron cluster drifting in the active volume of the TPC [57–60]. The typical width (FWHM) of the output signal is 200 nsec. Low noise amplifiers of LMH6655 were used to amplify a signal in the band-pass filter. Signals which passed the band-pass filter were sent to FADC modules through twisted pair cables by differential drivers (MAX4147).
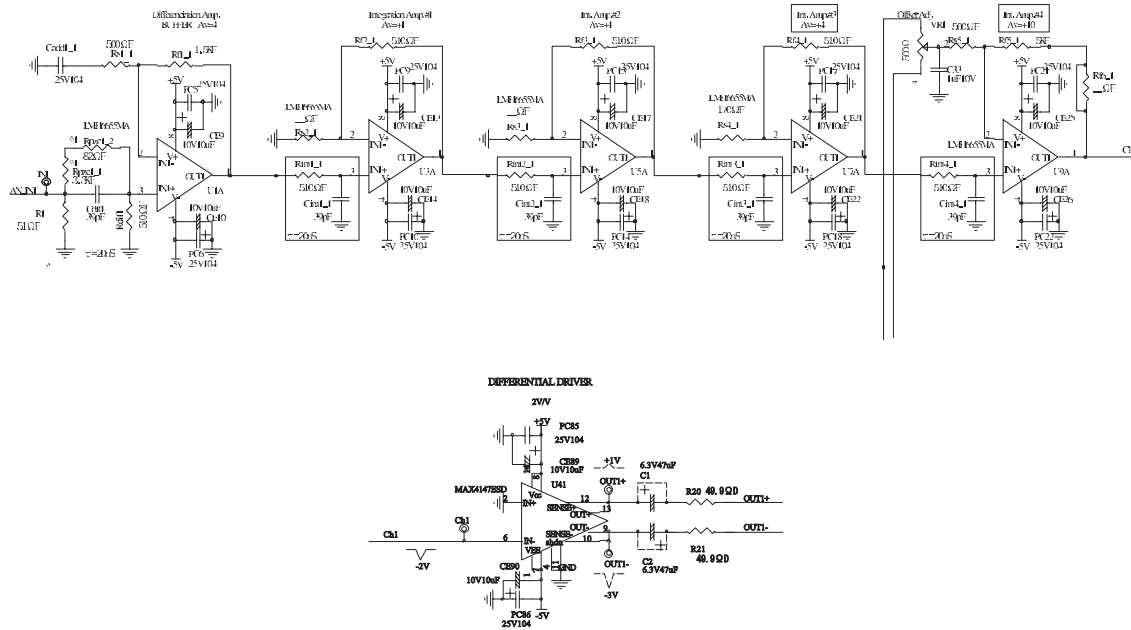


Figure G.2: Circuit diagram of the shaping amplifier used for the TPC.

Fig. G.3 shows a circuit diagram of the input part of the FADC module used for the TPC. The input part of the FADC consists of differential receivers (MAX4145), driver amplifiers for FADC (AD8138) and FADC chips (AD9203). The FADC chip has the resolution of 10 bit with 40 MHz sampling, an the maximum input voltage is 2 V.
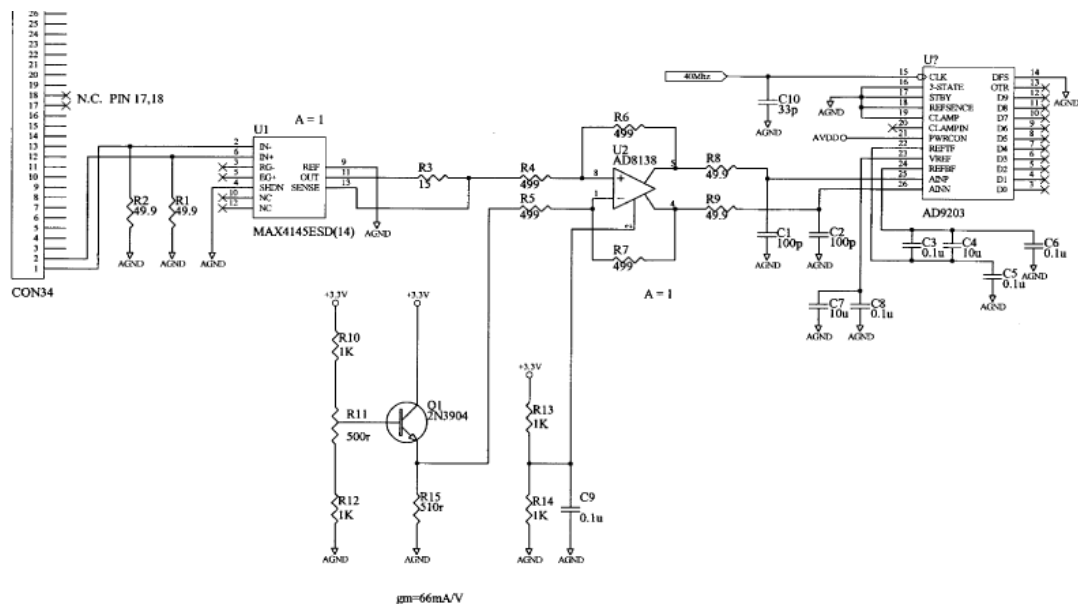


Figure G.3: Circuit diagram of the input part of the FADC module used for the TPC.

# Bibliography

[1] W.-M. Yao et al., J. Phys. G 33, 1 (2006) (PDG).

[2] N. Isgur and G. Karl, Phys. Rev. D18, 4187 (1978).

[3] T.A. DeGrand, Ann. Phys. N.Y. 101 ,496 (1976).

[4] R.H. Dalitz, Rev. Mod. Phys. 33, 471 (1961).

[5] R.H. Dalitz, T.C. Wong and G. Rajasekaran, Phys. Rev. 153, 1617 (1967).

[6] R.H. Dalitz, Euro. Phys. J C15, 748 (2000) (PDG).

[7] W. Melnitchouk et al., Phys. Rev. D67, 114506 (2003).

[8] Y. Nemoto, N.Nakajima, H. Matsufuru and H. Suganuma, Phys. Rev. D68, 094505 (2003).

[9] N. Ishii, T. Doi, M. Oka and H. Suganuma, Prog. Theor. Phys. Suppl. 168, 598 (2007).

[10] J.C. Nacher, E. Oset, H. Toki and A. Ramos, Phys. Lett. B455, 55 (1999).

[11] D. Jido, J.A. Oller, E. Oset, A. Ramos and U.-G, Meissner, Nuc. Phys. A755, 669 (2005).

[12] D.W. Thomas, A. Engler, H.E. Fisk and R.W. Kraemer Nucl. Phys. B56, 15 (1973).

[13] R.J. Hemingway, Nucl. Phys. B253, 742 (1985).

[14] J.K. Ahn et al., Nucl. Phys. A721, 715c (2003).

[15] S. Prakhov et al., Phys. Rev. C70, 034605 (2004).

[16] V.K. Magas, E. Oset and A. Ramos, Phys. Rev. Lett. 95, 052301 (2005).

[17] I. Zychor et al., Phys. Lett. B 660, 167 (2008).

[18] J.D. Davies et al., Phys. Lett. B 83, 55 (1979).

[19] M. Izycki *et al.*, Z. Phys. A 297, 11 (1980).

[20] P.M. Bird *et al.*, Nucl. Phys. A 404, 482 (1983).

[21] P.B. Siegel and B. Saghai, Phys. Rev. C 52, 392 (1995).

[22] Y.-A. Chao, R.W. Kraemer, D.W.Thomas and B.R. Martin, Nucl. Phys. B 56, 46 (1973).

[23] A.D. Martin, Nucl. Phys. B 179, 1 (1981).

[24] M. Iwasaki *et al.*, Phys. Rev. Lett. 78, 3067 (1997).

[25] Y. Akaishi and T. Yamazaki, Phys. Rev. C 65, 044005 (2002).

[26] T. Yamazaki and Y. Akaishi, Phys. Lett. B 535, 70 (2002).

[27] A. Dote, H. Horiuchi, Y. Akaishi and T. Yamazaki, Phys. Lett. B 590, 51 (2004).

[28] T. Suzuki *et al.*, Phys. Lett. B 597, 263 (2004).

[29] T. Suzuki *et al.*, Nucl. Phys. A 754, 375c (2005).

[30] M. Sato *et al.*, Phys. Lett. B 659, 107 (2008).

[31] T. Suzuki *et al.*, Phys. Rev. C 76, 068202 (2007).

[32] T. Kishimoto *et al.*, Nucl. Phys. A 754, 383c (2005).

[33] M. Agnello *et al.*, Phys. Rev. Lett. 94, 212303 (2005).

[34] M. Agnello *et al.*, Phys. Lett. B 654, 80 (2007).

[35] G. Bendiscioli *et al.*, Nucl. Phys. A 789, 222 (2007).

[36] `http://j-parc.jp/NuclPart/Proposal_e.html`.

[37] `http://www.oeaw.ac.at/smi/research/research_detail_amadeus.htm`; AMADEUS LOI, `http://www.lnf.infn.it/`.

[38] `http://www.oeaw.ac.at/smi/research/research_detail_fopi.htm`.

[39] M.Q. Tran *et al.*, Phys. Lett. B445, 20 (1998).

[40] J.W.C. McNabb *et al.*, Phys. Rev. C69, 042201 (2004).

[41] K.-H. Glander *et al.*, Eur. Phys. J. A19, 251 (2004).

[42] M. Sumihama *et al.*, Phys. Rev. C73, 035214 (2006).

[43] S. Capstick and W.Roberts, Phys. Rev. D58, 074011 (1998).

[44] Cambridge bubble chamber group, Phys. Rev. 156, 1426 (1967).

[45] R. Erbe *et al.*, Phys. Rev. 188, 2060 (1969).

[46] L. Guo and D.P. Weygand, hep-ex/0601010, in NSTAR05 Proceedings.

[47] Y. Oh, C.M. Ko and K. Nakayama, Phys. Rev. C 77, 045204 (2008).

[48] M.F.M. Lutz and M. Soyeur, Nucl. Phys. A748, 499 (2005).

[49] T. Nakano *et al.*, Nucl. Phys. A684, 71c (2001).

[50] SPring-8 annual report (1998) 132

[51] `http://www.esrf.eu/Accelerators/Groups/InsertionDevices/Software/Radia`
P. Elleaume, O. Chubar, J. Chavanne, "Computing 3D Magnetic Field from Insertion Devices", proc. of the PAC97 Conference May 1997, p.3509-3511.

[52] `http://garfield.web.cern.ch/garfield/`

[53] T. Mibe, Master thesis of Osaka university (in Japanese) (2000)

[54] N. Kaiser, P.B. Siegel and W. Weise, Nucl. Phys. A594, 325 (1995).

[55] S.I. Nam, J.H. Park, A. Hosaka, H.C. Kim, hep-ph/arXiv:0806.4029 .

[56] D. Jido, Y. Kanada, nucl-th/arXiv:0806.3601 .

[57] R.C. Jared, D.A. Landis, F.S. Goulding, IEEE Trans. Nucl. Sci. 29, 57, (1982).

[58] D.A. Landis *et al.*, IEEE Trans. Nucl. Sci. 29, 573, (1982).

[59] S.R. Klein *et al.*, IEEE Trans. Nucl. Sci. 43, 1768, (1996).

[60] F. Bieser *et al.*, Nucl. Inst. Meth. A385, 535, (1997).